

**STRUCTURAL EVOLUTION OF WEAKLY
DEFORMED NUCLEI IN MASS \sim 140 REGION
WITH INCREASING ANGULAR MOMENTUM**

By
SAJAD ALI
PHYS05201504010

Saha Institute of Nuclear Physics, Kolkata

A thesis submitted to the
Board of Studies in Physical Sciences
In partial fulfillment of requirements
for the Degree of
DOCTOR OF PHILOSOPHY
of
HOMI BHABHA NATIONAL INSTITUTE



June, 2020

Homi Bhabha National Institute

Recommendations of the Viva Voce Committee

As members of the Viva Voce Board, we certify that we have read the dissertation prepared by **Sajad Ali** entitled “**Structural evolution of weakly deformed nuclei in mass A ~ 140 region**” and recommend that it maybe accepted as fulfilling the dissertation requirement for the Degree of Doctor of Philosophy.

.....Date:

Chairman - Prof. Subinit Roy



.....Date: 21/08/2020

Guide - Prof. Sukalyan Chattopadhyay

.....Date:

Member 1 - Prof. Anjali Mukherjee

.....Date:

Member 2 - Prof. Maitreyee Saha Sarkar

.....Date:

Member 3 - Dr. Gopal Mukherjee

Final approval and acceptance of this dissertation is contingent upon the candidate's submission of the final copies of the dissertation to HBNI.

I hereby certify that I have read this dissertation prepared under my direction and recommend that it may be accepted as fulfilling the dissertation requirement.

Date: 21/08/2020

Place: KOLKATA



Guide: Prof. Sukalyan Chattopadhyay

STATEMENT BY AUTHOR

This dissertation has been submitted in partial fulfillment of requirements for an advanced degree at Homi Bhabha National Institute (HBNI) and is deposited in the Library to be made available to borrowers under rules of the HBNI.

Brief quotations from this dissertation are allowable without special permission, provided that accurate acknowledgement of source is made. Requests for permission for extended quotation from or reproduction of this manuscript in whole or in part may be granted by the Competent Authority of HBNI when in his or her judgement the proposed use of the material is in the interests of scholarship. In all other instances, however, permission must be obtained from the author.

A handwritten signature in black ink that reads "Sajad Ali". The signature is written in a cursive style with a horizontal dotted line underneath it.

Sajad Ali

DECLARATION

I, hereby declare that the investigation presented in the thesis has been carried out by me. The work is original and has not been submitted earlier as a whole or in part for a degree / diploma at this or any other Institution / University.

Sajad Ali
.....
Sajad Ali

List of Publications arising from the thesis

Journal

1. “Shears mechanism and development of collectivity in ^{141}Sm ”, S. Rajbanshi, **Sajad Ali**, Abhijit Bisoi, Somnath Nag, S. Saha, J. Sethi, T. Bhattacharjee, S. Bhattacharyya, S. Chattopadhyay, G. Gangopadhyay, G. Mukherjee, R. Palit, R. Raut, M. Saha Sarkar, A. K. Singh, T. Trivedi and A. Goswami, *Phys. Rev. C* **2016**, *94*, 044318.
2. “Evidence of antimagnetic rotation in an odd-odd nucleus: The case of ^{142}Eu ”, **Sajad Ali**, S. Rajbanshi, B. Das, S. Chattopadhyay, M. Saha Sarkar, A. Goswami, R. Raut, Abhijit Bisoi, Somnath Nag, S. Saha, J. Sethi, R. Palit, G. Gangopadhyay, T. Bhattacharjee, S. Bhattacharyya, G. Mukherjee, A. K. Singh and T. Trivedi, *Phys. Rev. C* **2017**, *96*, 021304(R).
3. “Evidence of the octupole correlation between shears bands in ^{142}Eu ”, **Sajad Ali**, S. Rajbanshi, R. Raut, H. Pai, Y. Y. Wang, G. Gangopadhyay, J. Meng, R. Palit, Somnath Nag, Abhijit Bisoi, S. Saha, J. Sethi, S. Bhattacharyya, S. Chattopadhyay, G. Mukherjee, A. K. Singh, T. Trivedi and A. Goswami, *Physics Letters B* **2019**, *798*, 134960.
4. “ ^{112}Sn target: Fabrication, characterization and application”, H. Pai, **Sajad Ali**, S. Rajbanshi, Prithwijita Ray, Subinit Roy, A. Goswami, *Vacuum* **2019**, *167*, 393-396.

Conferences

1. “Assignment of multipolarity for $\Delta I = 0$ γ transitions from Polarization measurements”, **Sajad Ali**, S. Rajbanshi, Abhijit Bisoi, Somnath Nag, S. Saha, J. Sethi, T. Trivedi, T. Bhattacharjee, S. Bhattacharyya, S. Chattopadhyay, G. Gangopadhyay, G. Mukherjee, R. Palit, R. Raut, M. Saha Sarkar, A. K. Singh and A. Goswami, *Proceedings of the DAE Symp. on Nucl. Phys.* **2017**, *62*, 196-197.
2. “Fabrication of ^{112}Sn target on ^{208}Pb -backing”, **Sajad Ali**, H. Pai, S. Rajbanshi, P. Ray, S. Roy, and A. Goswami, *Proceedings of the DAE Symp. on Nucl. Phys.* **2017**, *62*, 1132-1133.
3. “Coupling between two extreme excitation mode in weakly deformed ^{142}Eu ”, **Sajad Ali**, S. Rajbanshi, A. Goswami, Prithwijita Ray, H. Pai, R. Raut, Abhijit Bisoi, S. Chattopadhyay, Somnath Nag, R. Palit, S. Saha, J. Sethi, G. Gangopadhyay, S. Bhattacharyya, G. Mukherjee, A. K. Singh, T. Trivedi and M. Saha Sarkar, *Frontiers in Gamma Ray Spectroscopy 2018 (FIG18)*, TIFR, Mumbai.

Awarded best prize in the poster presentation

4. “ Multipolarity assignment of $\Delta I = 0$ γ transitions”, underline **Sajad Ali**, S. Rajbanshi, P. Ray, Abhijit Bisoi, Somnath Nag, S. Saha, J. Sethi, T. Trivedi, T. Bhattacharjee, S. Bhattacharyya, S. Chattopadhyay, G. Gangopadhyay, G. Mukherjee, R. Palit, R. Raut, M. Saha Sarkar, A. K. Singh and A. Goswami,
Zakopane Conference on Nuclear Physics Extremes of the Nuclear Landscape, 2018, Zakopane, Poland.

Others

1. “Abrupt phase change of the core rotation in the ^{143}Sm nucleus”, S. Rajbanshi, R. Raut, H. Pai, **Sajad Ali**, A. Goswami, G. Gangopadhyay, S. Bhattacharyya, G. Mukherjee, S. Muralithar, R. P. Singh, M. Kumar Raju, P. Singh and R. K. Bhowmik, *Phys. Lett. B* **2018**, 782, 143-148.
2. “Extremely asymmetric shears band in ^{143}Sm ”, S. Rajbanshi, R. Raut, H. Pai, **Sajad Ali**, A. Goswami, S. Bhattacharyya, G. Mukherjee, R. K. Bhowmik, S. Muralithar, R. P. Singh, G. Gangopadhyay, M. Kumar Raju, and P. Singh, *Phys. Rev. C* **2018**, 98, 061304(R).
3. “Search for unobserved transitions in ^{142}Eu ”, **Sajad Ali**, S. Rajbanshi, Abhijit Bisoi, Somnath Nag, S. Saha, J. Sethi, T. Trivedi, T. Bhattacharjee, S. Bhattacharyya, S. Chattopadhyay, G. Gangopadhyay, G. Mukherjee, R. Palit, R. Raut, M. Saha Sarkar, A. K. Singh and A. Goswami, *Proceedings of the DAE Symp. on Nucl. Phys.* **2016**, 61, 216-217.
4. “Deexcitation of three particle - three hole structure in ^{142}Eu ”, **Sajad Ali**, S. Rajbanshi, Prithwijita Ray, Abhijit Bisoi, Somnath Nag, S. Saha, J. Sethi, T. Trivedi, T. Bhattacharjee, S. Bhattacharyya, S. Chattopadhyay, G. Gangopadhyay, G. Mukherjee, R. Palit, R. Raut, M. Saha Sarkar, A. K. Singh and A. Goswami *Proceedings of the DAE Symp. on Nucl. Phys.* **2018**, 63, 210-211.

Sajad Ali

To my mentor

'Prof. Asimananda Goswami'

ACKNOWLEDGEMENTS

First and foremost, I would like to convey my profound gratitude to my mentor Prof. Asimananda Goswami for inspiring me to pursue research on experimental physics. Asimananda sir is one of the best teacher and human being I have ever met. Sir not just guided me in my PhD work and related research, but, his immense knowledge and the conversations with him will always motivate me in the process of thinking. I can say sir taught me the way of life. His guidance helped me in all the time of research and writing of this thesis. I could not have imagined having a better supervisor and mentor for my PhD work.

I would also like to express my sincere gratitude to Prof. Sukalyan Chattopadhyay for taking responsibility to guide me for the rest of my PhD period very after the passing away of my mentor Prof. Asimananda Goswami. It was my great pleasure for having in-depth discussion with Sukalyan sir who has immense of knowledge on the subject of nuclear physics.

Words can hardly express my deepest acknowledgment to my senior Subhendu da (Dr. Subhendu Rajbanshi) for the immense of help throughout my PhD period. He has taught me all the data analysis procedure of my PhD work along with many delicious recipe. I would also like to convey my honor to Prof. Subimal Sen, Prof. Chinamy Basu and Prof. Subinit Roy whose teaching in my MSc days have motivated me to pursue nuclear physics. I am thankful to my super senior Rajarshi da (Dr. Rajarshi Raut) of UGC-DAE-CSR for the immense of help during my PhD. I am also grateful to Hari da (Dr. Haridas Pai, SINP), Gopal sir (Dr. Gopal Mukherjee, VECC), Sarmistha mam (Dr. Sarmistha Bhattacharyya, VECC), Anajli mam (Prof. Anjali Mukherjee, SINP), Palit sir (Prof. Rudrajyoti Palit, TIFR), Prof. A. K. Singh (IIT Kharagpur), Prof. G. Gangopadhyay (CU), Pradipta da (Mr. Pradipta Kr. Das, SINP) and Sujib da (Mr. Sujib Chatterjee, SINP), Sutanu (GGDU), Saikat da (BHU), Sazedur (TIFR), Biswarup

da (Dr. Biswarup Das), Pradip da (Dr. Pradip Datta), Arindam Da (HENPP), Balaram Da (Dr. Balaram Dey) for the fruitful discussions and help. I am thankful to head of the nuclear physics division, Prof. Maitreyee Saha Sarkar. The accelerator and INGA facility at VECC, IUAC and TIFR are the places where I have got the real flavor of experimental nuclear physics, without the support at these places it would not be possible to conduct this research.

I thank my fellow flatmates cum besties Wadut, Snehal and Shuvankar, with them the five year journey is really awesome. I am very much grateful to my friends and colleagues Mantu, Sampad da, Anisur da, Santos da and many other at SINP. The very friendly atmosphere of SINP has not just taught me about my subject but also about life. I would also like to acknowledge the staffs of the SINP and VECC canteens.

Lastly, but certainly not the least, I could not have this far without the support of my Abba and Maa and my school days teachers, specially Fula kaka, Salam sir, Rashid sir, Santosh sir, Santanu sir, Tapas sir and Palash da.

I sincerely apologies to those I missed out in this list but whose help have privileged me.

Contents

List of Publications	vii
Summary	xix
List of Figures	xxiii
List of Tables	xxvii
1 Introduction	1
2 Nuclear Shape and Structure	7
2.1 Shell Closure Nuclei	8
2.2 Mid-Shell Nuclei: Nilsson Model	10
2.3 Nuclear Rotation	14
2.3.1 Principal axis rotation: The Cranking Model	16
2.3.1.1 Magnetic Dipole Transition Strengths: Dönau Model	21
2.3.1.2 Comparison of the Theoretical Calculation with Experimental Results	22

2.4	Exotic Modes of Excitation	25
2.4.1	Magnetic rotation	25
2.4.1.1	Shears Mechanism	27
2.4.1.2	Shears Mechanism with Principal Axis Cranking Model	29
2.4.2	Antimagnetic Rotation	32
2.4.2.1	Semi-classical particles-plus-rotor model	34
2.4.3	Chiral Symmetry Breaking	35
2.4.4	Octupole Deformation and Correlations	36
2.5	Summary	38
3	Experimental Techniques and Data Analysis	41
3.1	Fusion Evaporation Reaction	41
3.2	Decay of Residual Nuclei	43
3.3	Interaction of γ -Rays with Matter	43
3.3.1	Photoelectric Interaction	43
3.3.2	Compton Scattering	44
3.3.3	Pair Productions	45
3.4	Detection of γ -rays: Clover Detector	46
3.4.1	The Indian National Gamma Array	47
3.5	Data Analysis Techniques	49
3.5.1	Energy Calibration and Gain matching	49

3.5.2	Efficiency Calibration and Add-back factor	51
3.5.3	Coincidence Measurements and Analysis	53
3.5.4	Angular Distributions Measurements	54
3.5.4.1	Mixing Ratio Calculation	55
3.5.5	DCO Analysis	57
3.5.5.1	Width of the Substate Population (σ/j)	58
3.5.6	ADO Analysis	58
3.5.7	Linear Polarization Measurements	59
3.5.8	Level Lifetime Measurements	61
4	Structural Evolution in ^{141}Sm	65
4.1	Introduction	65
4.2	Experimental Details and Data Analysis	66
4.3	Experimental Result	66
4.4	Discussion	75
4.5	Summary	84
5	Structural Evolution in ^{142}Eu	85
5.1	Introduction	85
5.2	Experimental Results	87
5.2.1	Quadrupole structure QB I	88
5.2.2	Dipole structures DB I and DB II	91

5.2.3	Lineshape Analysis	96
5.3	Discussions	100
5.3.1	Evidence of AMR band in ^{142}Eu	101
5.3.2	Octupole correlation between two shears bands in ^{142}Eu	104
5.3.2.1	TAC-CDFT calculations	107
5.3.2.2	Dönau Model Calculations	107
5.3.2.3	SPAC Model Calculation	109
5.3.2.4	Octupole Correlation between DB I and DB II	111
5.4	Summary	113
6	Structural Evolution in ^{140}Eu	115
6.1	Introduction	115
6.2	Survey of the existing work in ^{140}Eu	116
6.3	Experimental Planning	116
6.3.1	Choice of Target-Projectile Combination: PACE4 Calculation	117
6.3.2	Fabrication of ^{112}Cd and ^{112}Sn Target	118
6.3.2.1	Vacuum Sealing of the Target Material	119
6.3.2.2	Preparation of ^{112}Cd and ^{112}Sn Ingot	120
6.3.2.3	Rolling of the ^{112}Sn and ^{112}Cd Ingot	123
6.4	Experimental Details	124
6.5	Data Analysis Techniques	125

6.6	Experimental Results	127
6.6.1	Width of the Substate Population	127
6.6.2	Construction of the Level Scheme	128
6.6.3	Level Lifetime Measurements	133
6.6.4	Discussion	137
6.6.5	Summary	138
7	Future Outlook	139
	Bibliography	141

List of Figures

1.1	Variation of $B(M1)$ values with spin in the Pb isotopes	4
2.1	Illustration of the single particle states arises from the shell model	9
2.2	Representation of spherical, prolate and oblate shape of nuclei in 2-d . . .	11
2.3	The different type of shapes of the nucleus at different β and γ values. . .	12
2.4	Strong and weak coupling of the single particle with the deformed core . .	15
2.5	Representation of the laboratory and body-fixed coordinate	17
2.6	The effect of the deformed core rotation on $g_{9/2}$ orbital	19
2.7	The quasi-particle coupling scheme in the geometrical Dönau model	21
2.8	Angular momentum vector coupling in the shears mechanism.	27
2.9	The normal initial alignment in the framework of shears mechanism	30
2.10	Angular momentum coupling scheme in the antimagnetic rotation	33
3.1	Illustration of the heavy-ion induced fusion-evaporation reaction	42
3.2	Interaction of γ -rays with matter	44
3.3	Graphical representation of the cross-section of γ interactions	45

3.4	The geometry of the clover detector	46
3.5	A photograph of the INGA detector setup at IUAC, New Delhi	48
3.6	Spectra of clover detector for before and after the gain matching	51
3.7	Efficiency of the clover detector in the INGA array at TIFR	52
3.8	The variation of add-back factor with γ -ray energy	53
3.9	Partial levelscheme for coincidence relation	54
3.10	Schematic arrangements of the conventional Compton polarimeter	60
3.11	Doppler broadened lineshape spectra for different detector angle	63
4.1	The double and triple coincidence spectra for γ -rays in ^{141}Sm	67
4.2	The partial proposed levelscheme of ^{141}Sm	68
4.3	R_{DCO} vs. σ/j and δ , angular distribution of 132.6 keV and a_2/a_4 vs δ plots	69
4.4	The summed gated spectra for the newly found γ 's in ^{141}Sm	70
4.5	The observed lineshape spectra for the transitions in ^{141}Sm	74
4.6	TRS contour plot for the configurations of DB I and DB II in ^{141}Sm	77
4.7	Comparison of the SPAC calculations with the experimental results	78
4.8	Variation of excitation energies with spin for the dipole bands in ^{141}Sm	79
4.9	Aligned angular momentum, quasiparticle routhians, energy staggering and moment of inertia plots for the dipole bands in ^{141}Sm	81
4.10	The comparison of the angular momentum of Sm, Eu, Gd nuclei with ω	83
5.1	Partial proposed levelscheme of ^{142}Eu	86
5.2	Coincidence spectra shows the transitions of the excited states in ^{142}Eu	88

5.3	Angular distribution, χ^2 and R_{DCO} vs PDCO plot for 602 and 1021 keV	89
5.4	Coincidence spectra for the newly observed transitions of DB I in ^{142}Eu	91
5.5	Coincidence spectra for the newly found transitions of DB II in ^{142}Eu	92
5.6	Spectra for the connecting transitions between DB I and DB II	93
5.7	The experimental lineshape fitted spectra for γ 's of QB I in ^{142}Eu	97
5.8	The experimental lineshape fitted spectra for γ 's of DB I in ^{142}Eu	99
5.9	The experimental lineshape fitted spectra for γ 's of DB II in ^{142}Eu	100
5.10	Experimental $B(E2)$ vs. I and I vs. ω with SPRM model calculation	102
5.11	Alignment plot for the quadupole band QB I in ^{142}Eu	103
5.12	Angular momenta calculated by TAC-CDFT for the DB I and II in ^{142}Eu	107
5.13	The plot of experimental $B(M1)$ with Dönau calculation for the DB I and DB II	108
5.14	Plot for measured $B(M1)$, $B(E2)$ and ω with SPAC calculation	109
5.15	The experimental $B(M1)$ and $B(E2)$ with SPAC calculations for DB II	110
5.16	δE , $\omega^-(I)/\omega^+(I)$ for opposite parity bands in Eu, Th and other isotopes	111
5.17	The $B(E1)/B(E2)$ and the dipole moment against I for different nuclei	111
5.18	The potential energy surface of ^{142}Eu calculated by the MDC-CDFT	113
6.1	PACE4 calculation for the reactions $^{32}\text{S} + ^{112}\text{Cd}$ and $^{32}\text{S} + ^{112}\text{Sn}$	117
6.2	The Pi chart for the isotopic abundance of Tin and Cadmium	119
6.3	A photograph of vacuum tube sealing setup at SINP	120
6.4	The different states for foil preparation of the ^{112}Cd isotope	121

6.5	The different states for foil preparation of the ^{112}Sn isotope	122
6.6	Image of rolling machine at Saha Institute of Nuclear Physics	124
6.7	Image of the Pb backed ^{112}Cd target after the experiment at IUAC	125
6.8	Geometrical asymmetry correction factor $a(E_\gamma)$ for a clover detector	126
6.9	The m-state population (σ/j) calculation from the R_{DCO}	127
6.10	The partial level scheme of ^{140}Eu from the present analysis	134
6.11	Gated spectra of 537.4 and 484.3 keV in ^{140}Eu	135
6.12	Gated spectra of 646.9 and 406.3 keV in ^{140}Eu	136
6.13	The experimental line shapes fitted spectra of transitions in ^{140}Eu	138

List of Tables

3.1	Measured calibration coefficients of the clover detector	50
4.1	Table of E_γ , I_γ , R_{DCO} , R_θ , Polarization and δ in ^{141}Sm	71
4.2	Measured level lifetimes and corresponding $B(M1)$ values in ^{141}Sm	76
5.1	E_γ , I_γ , R_{DCO} , $R(\theta)$ and PDCO for the transitions in ^{142}Eu	94
5.2	The $B(E2)$, $J^{(2)}$ and $J^{(2)}/B(E2)$ values for the QB I in ^{142}Eu	101
5.3	Measured τ , $B(M1)$ and $B(E2)$ values for DB I	105
5.4	Measured τ , $B(M1)$, $B(E1)$, $B(E2)$, Q_0 and D_0 values for DB II	106
5.5	Parameters used in the Dönaue model calculation of $B(M1)$ values	108
5.6	The $B(E1)$ rates, $B(E1)/B(E2)$ ratio and dipole moments of the DB II	113
6.1	Experimental parameters for the reactions $^{32}\text{S} + ^{112}\text{Cd}$ and $^{32}\text{S} + ^{112}\text{Sn}$	118
6.2	E_γ , I_γ , R_{DCO} , $R(\theta)$ and PDCO (Δ) for the γ 's in ^{140}Eu	129
6.3	Table of $B(M1)$ and $B(E2)$ from the measured level lifetime in ^{140}Eu	137

Summary

The main objective of the present thesis work is to investigate the various mechanisms of the generation of angular momentum, which result in the evolution of nuclear structure in the weakly deformed nuclei of mass $A \sim 140$ region. In this thesis work, the high-spin level structure of ^{141}Sm ($Z = 62$, $N = 79$), ^{142}Eu ($Z = 63$, $N = 79$) and ^{140}Eu ($Z = 63$, $N = 77$) have been experimentally investigated using the gamma-ray spectroscopic technique.

The availability of particles and holes in the high- j $h_{11/2}$ orbital in mass ~ 140 region leads to the different exotic excitation mechanisms through the coupling of the quasi-particle and the collective angular momenta. The quasi-particle angular momenta contribute coherently to generate the high angular momentum states in magnetic (MR) and anti-magnetic rotational bands (AMR) [1–3]. On the other hand, the opposite shape driving effects of the proton particles and the neutron holes in the $h_{11/2}$ orbital may lead to a triaxially deformed nuclei [4]. It may also be possible to observe transitions from magnetic (planar tilt) to Chiral doublet band (aplanar tilt) with increase of excitation energy. In addition, the occupancy of the $d_{5/2}$ and the $h_{11/2}$ orbitals by the protons may lead to the observation of octupole correlation in this mass region [5].

The high spin states of the ^{141}Sm were populated by the reaction $^{116}\text{Cd}(^{31}\text{P}, p5n)$ with $E_{\text{Lab}} = 148$ MeV, at Pelletron LINAC facility TIFR. The deexciting γ 's were detected using an array of clover detectors, named Indian National gamma Array (INGA). This study has established three dipole sequence (DB I, DB II and DB III), where the observed

magnetic dipole transition rates ($B(M1)$) have been found to decrease with increasing spin. The Shears Mechanism with Principal Axis (SPAC) calculations [6–8] could reproduce the falling trend of the $B(M1)$ values using the $\pi h_{11/2}^2 \otimes \nu h_{11/2}^{-1}$ configuration for DB I. The SPAC model calculations have also been performed for the dipole band DB II using the configuration $\pi h_{11/2}^2 \otimes \nu h_{11/2}^{-3}$. These calculations reproduced the falling trend of the $B(M1)$ values. The routhian plot showed a rapid increase in ω with angular momentum which has been also observed in ^{139}Sm [9]. This has been interpreted as the onset of collectivity along the MR band. The partner bands II and III show excellent similarities in the measured quasiparticle alignment, the quasiparticle routhians, the energy staggering and the kinetic moment of inertia. The existence of the degenerate $\Delta I = 1$ doublet bands II and III suggest that the ^{141}Sm can have triaxial deformed nuclear shape at the higher spins. Thus, it may be concluded that a smooth transition of the nuclear shape, from planar (MR) to aplanar (chiral) may exist in ^{141}Sm .

In the same reaction the excited states of the ^{142}Eu nucleus were also populated. A quadrupole band (QB I) and two opposite parity dipole bands (DB I and DB II) were observed. The $B(E2)$ values of the QB I showed a monotonically decreasing nature with increasing spin. The observed behavior could be well reproduced in the framework of Shears Mechanism with Principal axis Rotation Model (SPRM) calculations [7] with the proposed configuration $\pi g_{7/2}^{-1} \nu h_{11/2}^{-3} \otimes \pi h_{11/2}^2$. This leads to the novel observation of an AMR band in an odd - odd nuclei.

The positive parity dipole sequence DB I showed the characteristic staggering in the $\Delta I = 1$ transition energies which is a fingerprint of the Principal Axis Rotation (PAR) [3, 10], whereas, the negative parity dipole sequence (DB II) exhibit the conventional characteristics of a magnetic rotational band [11]. The theoretical calculation based on Tilted Axis Cranking - with Co-variant Density Functional Theory (TAC-CDFT) [12–17] indicates $\pi h_{11/2}^1 (g_{7/2}/d_{5/2})^{-2} \otimes \nu h_{11/2}^{-1}$ and $\pi h_{11/2}^2 (g_{7/2}/d_{5/2})^{-1} \otimes \nu h_{11/2}^{-1}$ configurations for DB I and DB II, respectively.

The corresponding reduced transition probabilities $B(M1)$, $B(E1)$ and $B(E2)$ values for the bands DB I and DB II were estimated from the measured level lifetimes. The $B(M1)$ and $B(E2)$ values for both the bands showed a falling trend. The SPAC model calculations indicated that the DB II originate due to the shears mechanism while the DB I is generated due to the interplay of the shears mechanism and collective rotation. The band DB II was found to decay to DB I by enhanced $E1$ transitions ($B(E1) \sim 10^{-4}$). Such large electric dipole transition strengths are the finger prints of the octupole correlation which is supported by the Multi-Dimensional Co-variant Density Functional Theory (MDC-CDFT) calculation [18–20]. This is the first experimental evidence of octupole correlation between two shears bands.

To study the possible chiral symmetry breaking as proposed earlier [21] and to test the border of the island of chirality ($N = 77$) [22, 23] an experiment was proposed to study the ^{140}Eu ($N = 77$) nucleus. The ^{140}Eu can be populated by two possible way using ^{32}S beam on ^{112}Cd and ^{112}Sn at $E_{Lab} = 145$ MeV and 155 MeV, respectively. For this purpose two metallic foils of ^{112}Cd and ^{112}Sn are prepared from powder like materials. During the time of experiment, the maximum beam energy available was 145 MeV. Thus the reaction using the ^{112}Cd target was chosen.

The level scheme ^{140}Eu has been extended substantially in the present measurement. In the earlier measurement [21], a cascade of $M1$ transitions has been reported, which was not connected with the main part of the level scheme. In the present analysis, five new transitions have been identified via which this cascade decays to the main part of the level scheme. The DCO ratio, ADO ratio and PDCO measurements have been used to assign the spin-parity to the excited levels. From the present data, ten quadrupole bands and two dipole bands have been established but no signature of the chiral doublet band could be observed.

This thesis is organized in seven chapters. The first chapter gives a short introduction to the physics scope of the thesis. The different nuclear structure models relevant to

this thesis work have been described in the second chapter. The different spectroscopic techniques used have been described in chapter three. The investigation of the high spin behaviors of ^{141}Sm , ^{142}Eu and ^{140}Eu have been presented in chapters four, five and six, respectively. The chapter seven contains a short write up on the future outlook.

Summary

The main objective of the present thesis work is to investigate the various mechanisms of the generation of angular momentum, which result in the evolution of nuclear structure in the weakly deformed nuclei of mass $A \sim 140$ region. In this thesis work, the high-spin level structure of ^{141}Sm ($Z = 62$, $N = 79$), ^{142}Eu ($Z = 63$, $N = 79$) and ^{140}Eu ($Z = 63$, $N = 77$) have been experimentally investigated using the gamma-ray spectroscopic technique.

The availability of particles and holes in the high- j $h_{11/2}$ orbital in mass ~ 140 region leads to the different exotic excitation mechanisms through the coupling of the quasi-particle and the collective angular momenta. The quasi-particle angular momenta contribute coherently to generate the high angular momentum states in magnetic (MR) and anti-magnetic rotational bands (AMR) [1–3]. On the other hand, the opposite shape driving effects of the proton particles and the neutron holes in the $h_{11/2}$ orbital may lead to a triaxially deformed nuclei [4]. It may also be possible to observe transitions from magnetic (planar tilt) to Chiral doublet band (aplanar tilt) with increase of excitation energy. In addition, the occupancy of the $d_{5/2}$ and the $h_{11/2}$ orbitals by the protons may lead to the observation of octupole correlation in this mass region [5].

The high spin states of the ^{141}Sm were populated by the reaction $^{116}\text{Cd}(^{31}\text{P}, p5n)$ with $E_{\text{Lab}} = 148$ MeV, at Pelletron LINAC facility TIFR. The deexciting γ 's were detected using an array of clover detectors, named Indian National gamma Array (INGA). This study has established three dipole sequence (DB I, DB II and DB III), where the observed

magnetic dipole transition rates ($B(M1)$) have been found to decrease with increasing spin. The Shears Mechanism with Principal Axis (SPAC) calculations [6–8] could reproduce the falling trend of the $B(M1)$ values using the $\pi h_{11/2}^2 \otimes \nu h_{11/2}^{-1}$ configuration for DB I. The SPAC model calculations have also been performed for the dipole band DB II using the configuration $\pi h_{11/2}^2 \otimes \nu h_{11/2}^{-3}$. These calculations reproduced the falling trend of the $B(M1)$ values. The routhian plot showed a rapid increase in ω with angular momentum which has been also observed in ^{139}Sm [9]. This has been interpreted as the onset of collectivity along the MR band. The partner bands II and III show excellent similarities in the measured quasiparticle alignment, the quasiparticle routhians, the energy staggering and the kinetic moment of inertia. The existence of the degenerate $\Delta I = 1$ doublet bands II and III suggest that the ^{141}Sm can have triaxial deformed nuclear shape at the higher spins. Thus, it may be concluded that a smooth transition of the nuclear shape, from planar (MR) to aplanar (chiral) may exist in ^{141}Sm .

In the same reaction the excited states of the ^{142}Eu nucleus were also populated. A quadrupole band (QB I) and two opposite parity dipole bands (DB I and DB II) were observed. The $B(E2)$ values of the QB I showed a monotonically decreasing nature with increasing spin. The observed behavior could be well reproduced in the framework of Shears Mechanism with Principal axis Rotation Model (SPRM) calculations [7] with the proposed configuration $\pi g_{7/2}^{-1} \nu h_{11/2}^{-3} \otimes \pi h_{11/2}^2$. This leads to the novel observation of an AMR band in an odd - odd nuclei.

The positive parity dipole sequence DB I showed the characteristic staggering in the $\Delta I = 1$ transition energies which is a fingerprint of the Principal Axis Rotation (PAR) [3, 10], whereas, the negative parity dipole sequence (DB II) exhibit the conventional characteristics of a magnetic rotational band [11]. The theoretical calculation based on Tilted Axis Cranking - with Co-variant Density Functional Theory (TAC-CDFT) [12–17] indicates $\pi h_{11/2}^1 (g_{7/2}/d_{5/2})^{-2} \otimes \nu h_{11/2}^{-1}$ and $\pi h_{11/2}^2 (g_{7/2}/d_{5/2})^{-1} \otimes \nu h_{11/2}^{-1}$ configurations for DB I and DB II, respectively.

The corresponding reduced transition probabilities $B(M1)$, $B(E1)$ and $B(E2)$ values for the bands DB I and DB II were estimated from the measured level lifetimes. The $B(M1)$ and $B(E2)$ values for both the bands showed a falling trend. The SPAC model calculations indicated that the DB II originate due to the shears mechanism while the DB I is generated due to the interplay of the shears mechanism and collective rotation. The band DB II was found to decay to DB I by enhanced $E1$ transitions ($B(E1) \sim 10^{-4}$). Such large electric dipole transition strengths are the finger prints of the octupole correlation which is supported by the Multi-Dimensional Co-variant Density Functional Theory (MDC-CDFT) calculation [18–20]. This is the first experimental evidence of octupole correlation between two shears bands.

To study the possible chiral symmetry breaking as proposed earlier [21] and to test the border of the island of chirality ($N = 77$) [22, 23] an experiment was proposed to study the ^{140}Eu ($N = 77$) nucleus. The ^{140}Eu can be populated by two possible way using ^{32}S beam on ^{112}Cd and ^{112}Sn at $E_{Lab} = 145$ MeV and 155 MeV, respectively. For this purpose two metallic foils of ^{112}Cd and ^{112}Sn are prepared from powder like materials. During the time of experiment, the maximum beam energy available was 145 MeV. Thus the reaction using the ^{112}Cd target was chosen.

The level scheme ^{140}Eu has been extended substantially in the present measurement. In the earlier measurement [21], a cascade of $M1$ transitions has been reported, which was not connected with the main part of the level scheme. In the present analysis, five new transitions have been identified via which this cascade decays to the main part of the level scheme. The DCO ratio, ADO ratio and PDCO measurements have been used to assign the spin-parity to the excited levels. From the present data, ten quadrupole bands and two dipole bands have been established but no signature of the chiral doublet band could be observed.

This thesis is organized in seven chapters. The first chapter gives a short introduction to the physics scope of the thesis. The different nuclear structure models relevant to

this thesis work have been described in the second chapter. The different spectroscopic techniques used have been described in chapter three. The investigation of the high spin behaviors of ^{141}Sm , ^{142}Eu and ^{140}Eu have been presented in chapters four, five and six, respectively. The chapter seven contains a short write up on the future outlook.

CHAPTER 1

Introduction

The atomic nucleus is a complex many body finite quantal system. The understanding of the various properties of the nucleus through the nucleon-nucleon interaction is the main motivation of the nuclear physics studies. The advent of present day accelerators and detection techniques enable us to make in-depth study of the nucleon-nucleon interaction through the investigation of the nuclear reaction mechanisms across the energy scale and the nuclear structure at high angular momenta but low excitation energies. The generation of high angular momentum states in the atomic nuclei has become a topic of special interest in nuclear-structure studies.

The radiative transitions between the excited non-degenerate energy states of a quantal system explicitly reveal the existence of a perturbative interaction and the multipole character of this potential plays a crucial role in exhibiting a diverse modes of excitation [24]. In the atomic nucleus, the multipole character of the perturbative Hamiltonian has direct correspondence to the symmetry-breaking phenomena [3]. The breaking of the symmetry in mass, charge and current distributions leads to the observation of the different types of exotic excitation mechanisms in the excited level structures of the atomic nuclei. These modes of excitations depend on the occupancy of the nuclear orbitals near the Fermi surface by valence particles, which in turn, leads to various nuclear shapes.

The shape of the closed shell nuclei is spherical and thus, no axis of reference exists by which the change in orientation can be identified. Therefore, rotation cannot be observed for spherical nuclei. If the shape deviates from spherical symmetry, the rotational bands connected by strong $E2$ transitions, are observed as the manifestation of nuclear rotation.

In the spherical nuclei, the higher angular momentum states are generated via the coupling of the angular momentum of individual nucleons and/or the holes created as a result of the excitation of nucleons to the higher lying orbitals (commonly known as single particle excitations). Such type of excitations result in a randomly spaced level structure for these nuclei.

For the mid-shell nuclei with a large number of nucleons outside the closed core the nuclear-shape evolves into the axially deformed shape. The quadrupole term of the perturbative interaction potential is responsible for the deformed shape which breaks the rotational symmetry of the nuclear mass (charge) distribution. Such symmetry-breaking leads to the observation of the band structures connected by intraband $E2$ transitions with large $B(E2)$ strengths. The angular momentum in such systems is predominantly generated through collective rotation around a principal axis and termed as Principal Axis Rotation (PAR) [3, 10]. This mode of excitation has been successfully described in the framework of cranking shell model (CSM) calculations [25]. In this case, the signature (quantum number associated with π -rotational symmetry) is a good quantum number which leads to characteristic staggering in the $\Delta I = 1$ transition energies and in the magnetic dipole transition rates ($B(M1)$). The electric quadrupole transition rates remain nearly constant.

On the other hand, for weakly deformed nuclear systems which do not have any preferred axis of rotation, i. e., the total angular momentum does not coincide with any of the principal axis (tilted axis rotation TAR) [11]. In this case (around a non-principal axis), the signature is no longer a good quantum number [10, 11] and the phenomenon manifests itself in sequences of $M1$ transitions (as known as magnetic rotation) with

increasing gamma-ray transition energies and decreasing $B(M1)$ and $B(E2)$ values along with the band. Such band structures have been observed for a large number of weakly deformed nuclei across different mass regions and their characteristics have been well explained in the light of the Tilted Axis Cranking (TAC) calculations [2, 9, 26–33].

In a moderately deformed nucleus, however, a high spin band may originate due to an interplay of PAR and TAR. Such a band may simultaneously exhibit the staggering in the $\Delta I = 1$ transition energies and a decrease in the $B(M1)$ rates [34, 35]. This is plausible since the $M1$ energy staggering originates due to the influence of the rotationally aligned nucleons while the falling trend of the $B(M1)$ rate is governed by the deformation aligned nucleons.

Most of the deformed nuclei can be adequately described as an axial- and reflection-symmetric spheroidal shape, by which the experimentally observed properties of the resulting band structures can be well reproduced. As these shapes are symmetric under space inversion, all levels of the rotational band will have the same parity. The reflection-asymmetric shapes arise due to the octupole term of the interaction potential, which can also play a vital role in the excitation mechanism, though they are not as stable as the familiar quadrupole deformations [5]. Such a mode of excitation arises from the interaction between the opposite parity orbitals with $\Delta l = \Delta j = 3$ near the Fermi surface. This mode of excitation will result in a separation between the center of mass and center of charge of the nucleus, thereby leading to the observation of the alternating parity bands, which are connected by the enhanced $E1$ transitions [36].

A special case of rotational band like structure in weakly deformed nuclei may occur when the symmetry is broken with respect to the total angular momentum vector of two shears-like configurations. The perpendicular components of magnetic dipole moment vectors for the two shears are anti-aligned and cancel each other and, therefore, the $B(M1)$ values vanish. Due to the resemblance to the cancellation of magnetic moments in an antiferromagnet, this type of coupling has been called “antimagnetic rotation” (AMR)

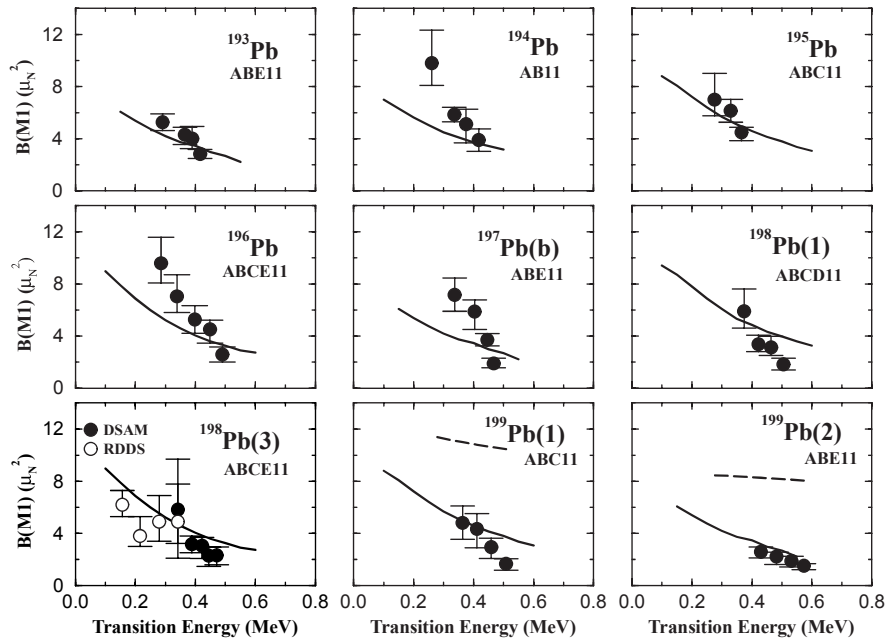


Figure 1.1: The variation of magnetic dipole transition rates ($B(M1)$) with the spin in the Pb isotopes adopted from the ref. [1].

[1–3]. For the AMR bands the angular momentum is generated by the simultaneous step-by-step closing of the two shears. Since the antimagnetic rotor is symmetric with respect to rotation by 180° about the angular momentum axis, the bands consist of sequences of energy levels differing in spin by $2\hbar$. Due to the small deformation of the core, these levels decay by weak $E2$ transitions, with $B(E2)$ values decreasing with increasing spin.

In a geometric model, the TAR can be understood in the framework of shears mechanism. The shears mechanism originates from a nearly perpendicular coupling of the angular momentum vectors of the high- j proton-particle and neutron-hole or vice-versa and the repulsive interaction between them. The possible existence of the MR and AMR excitations can occur for nuclei having proton and/or neutron near the shell closure. The MR bands have been observed in weakly deformed nuclei near magic or semi-magic proton numbers $Z = 80 - 83, 55 - 64, 45 - 50$ and $35 - 37$ and/or neutrons near $N = 110 - 120, 75 - 82, 55 - 64$ and $44 - 48$ in mass $A \sim 190, 140, 100$ and 80 regions [37]. The largest number of MR bands has been identified in mass $A \sim 190$ region. The experimental $B(M1)$ values show the characteristic decrease with spin in these nuclei thereby

establishing MR phenomena (Figure 1.1). Until today, the AMR band is observed in mass $A \sim 110$ and 140 regions [38–41] in weakly deformed even-even and odd mass nuclei. The recent observation of AMR in ^{143}Eu reports the maiden observation of AMR outside the $A \sim 100$ region [42] and simultaneous presence of AMR along with MR in the same system [42, 43].

The transitional nuclei of mass $A \sim 140$ region exhibits a variety of the interesting nuclear structure phenomena, which can be utilized to test a variety of nuclear models. Due to the proximity of the spherical shell closures and competing shape (prolate and oblate) driving effects of the high- j orbitals near the proton and neutron Fermi levels, several novel phenomena, like shears mechanism, octupole correlation, chiral symmetry breaking, etc. are expected to be observed in these nuclei. Since both the MR and AMR phenomena are the consequence of the shears mechanism, they are expected to be observed simultaneously in the same nucleus in this mass region. It is worth noting that, the anisotropy in the current distribution of the high- j orbital is the primary criterion for the existence of the AMR band in the weakly deformed nuclei. Therefore, there is no reason for not observing in the same in the weakly deformed systems with the appropriate high- j orbital occupancy to form the double shear structure. In mass $A \sim 140$ region, the $d_{5/2}$ and $h_{11/2}$ proton orbitals lie close together and near the Fermi surface, thereby, can form the basis for the octupole interaction. The interaction between such pairs of orbitals may induce instability in the mean-field towards β_3 deformations [44]. On the other hand, the $d_{5/2}$ and $g_{7/2}$ proton orbitals interact through the Y_{20} . This means that octupole correlation effects may be seen over a considerable range of proton numbers and/or might result in the dilution of the octupole effect [45]. Though these nuclei are investigated extensively both experimentally and theoretically, the underlying mechanisms of the above-mentioned novel phenomena are not yet perceived completely. The present thesis work aim to understand the mechanism of generating angular momentum in weakly deformed nuclei in mass $A \sim 140$ region. The main motivation of the thesis is to search the coexistence of the MR and AMR bands in an odd-odd nucleus in the $A \sim 140$ mass

region and in search for the fingerprints of the existence of the octupole correlation.

In the present thesis, the experimental investigations have been carried out using the in-beam gamma-ray spectroscopy technique which is regarded as one of the most effective tools for Nuclear Structure studies. The thesis reports the results of the spectroscopic investigations of $N = 79$ ^{141}Sm and ^{142}Eu and $N = 77$ ^{140}Eu nuclei populated through the fusion-evaporation reaction ^{31}P (^{116}Cd , p5n and 5n) and ^{32}S (^{112}Cd , 4n), respectively. The de-exciting γ rays were detected using the Indian National Gamma Array (INGA), an array of Compton-suppressed clover detector. The use of fusion evaporation reactions resulted in the population of high spin states and the clover detector facilitated linear polarization measurements which are of relevance for the determination of the electromagnetic nature of the γ -ray transitions. The precise level lifetimes of the bands of interest have been measured using the Doppler shift attenuation method. The development of collectivity at the high spin domain of the MR band in ^{141}Sm has been discussed in Chapter 4. In the same chapter, a possible transition in ^{141}Sm at high spin from a MR band (total angular momentum is in one of the principal plane: planar) to the chiral doublet band (total angular momentum is out of the plane: aplanar) has been proposed. The Chapter 5 reports the novel observation of the presence of octupole correlation between the two shears bands of ^{142}Eu . In the same nucleus the coexistence of MR and AMR has also been reported. The high spin level structure of ^{140}Eu has been discussed in Chapter 6.

CHAPTER 2

Nuclear Shape and Structure

The study of nuclear shape and structure at higher excitation energies allows us to investigate the different angular momentum generation mechanisms. No ab-initio theory exists which can fully describe the wealth of spectroscopic data, which have been collected across the periodic table over last four decades at different accelerator centres of the world. However, substantial progress has been and is being made with the aid of conceptual models designed to give insight into the underlying physics of the inherently complex situation.

One of the first bulk properties of the nucleus to be modeled is its binding energy. The successful model of the nuclear binding energy is the semi-empirical mass formula obtained after successive studies of the average binding energy (B/A) by Bethe & Weizsacker. This model proposed that the shape of the nucleus is similar to an in-compressible macroscopic liquid drop which has been very successful to predict the bulk properties of the nuclei. But it failed to explain the sudden jumps in the nucleon separation energies (binding energy of the last nucleons) at some definite nucleon numbers, called the magic numbers. This observation of the magic numbers led to the development of the Shell model in nuclear physics [46–48].

The development of the shell model in turn hinted that the accumulation of p-n

interaction strength may lead to additional configuration mixing and deviation from the spherical symmetry even in the ground state. This produces the asymmetry in mass distribution which results in permanent stable deformed shape, oblate or prolate, in nuclei and collective rotation is then possible around an axis perpendicular to the symmetry axis. The accumulation of the p-n interaction strength becomes largest for the mid-shell nuclei and consequently regular level sequences connected by $E2$ intraband transitions have been observed [49–51]. However, the rotation around any of the three principal axes; short, long and intermediate axes, is possible for the nuclei having triaxial nuclear mass distribution [52]. The rotational energy depends on the moment of inertia, which is characterized by the deformation parameters β and γ . Thus, the rotational energy around the shortest principal axis becomes favorable for $\gamma \approx 30^\circ$ which is observed for nuclei in $A \sim 60, 110, 140$ and 160 mass regions [53–57]. The rotation around the intermediate axis may become energetically favorable for $\gamma \approx -30^\circ$ when pairing correlations are considered [10], as observed in the recent studies in ^{77}Kr [58, 59].

In the present chapter, the different exotic excitation mechanisms arising due to the different nuclear shapes (spherical or weakly deformed, axially prolate and/or oblate deformed and triaxially deformed) will be discussed.

2.1 Shell Closure Nuclei

The primary aim for the study of the consequences of the nuclear shell structure is to obtain the wave functions and eigenvalues corresponding to one-particle motion in the nuclear potential. The short range character of the nucleonic forces suggests that the potential approximately resemble the density distribution and, thus, as a first approximation, it may be considered as a square well potential. A qualitatively similar harmonic oscillator potential is widely used. It plays the role, which is somewhat similar to the Coulomb potential in atomic physics. It is seen from Figure 2.1 that, if the nuclear po-

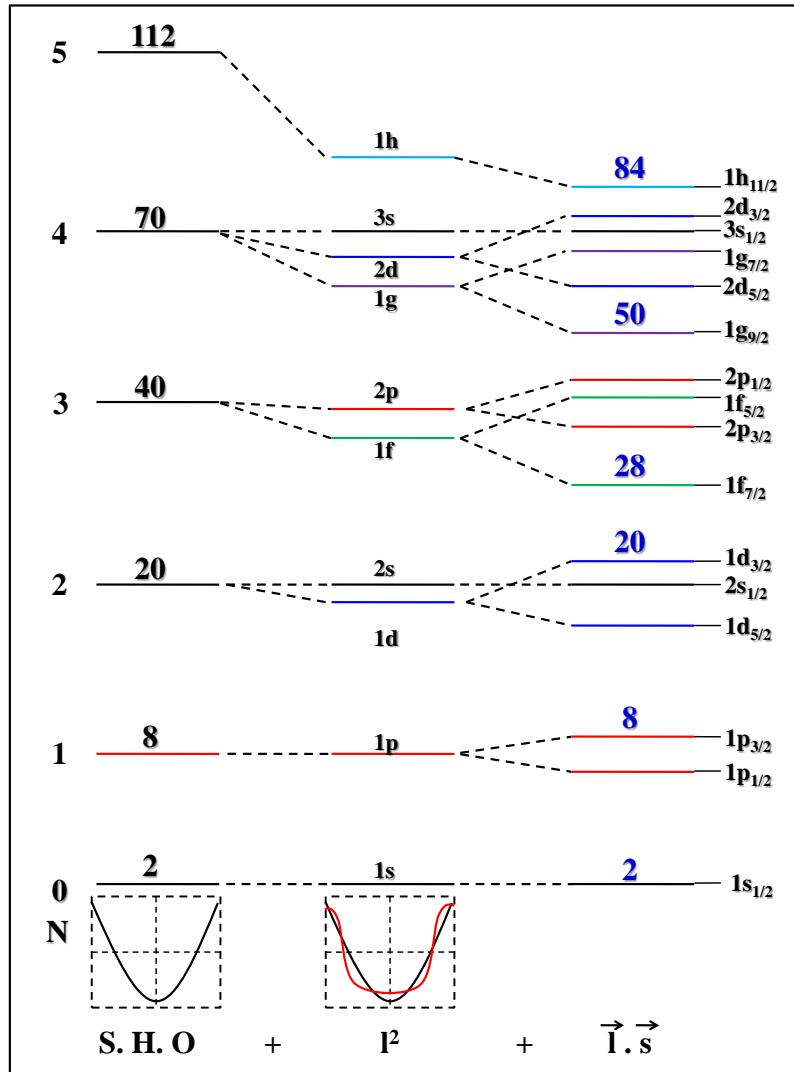


Figure 2.1: (Top) Illustration of the single-particle energy states for simple harmonic oscillator potential, simple harmonic potential with l^2 and spin-orbit interaction terms. (Bottom) Schematic diagram of the two shell model potentials, one is S. H. O. potential and another one is modified harmonic oscillator which simulates to some extent of the effect of l^2 term as in ref. [48].

tential were similar to that of a harmonic oscillator, then the major shell closings would occur at nucleon numbers 2, 8, 20, 40, 70, 112, and 168 [48]. The first three members of the series, correspond to the observed magic numbers, but not the higher ones.

The choice of a more realistic radial dependence somewhat modifies the detailed sequence of orbits. The main effect is to remove the harmonic oscillator degeneracy in such a way that the orbits of higher l are depressed with respect to the low l orbits. However, the decisive step in the development of the nuclear shell model was the recognition of a

strong spin-orbit interaction in the nucleonic motion, which led to a natural explanation of the magic numbers [60,61]. This coupling splits the levels with $j = l \pm 1/2$, which are degenerate in a spin-independent potential, and if the sign is chosen to lower the levels with $j = l + 1/2$, then the observed magic numbers are obtained.

The sequence of single-particle levels that results when the spin-orbit interaction is confirmed by a large body of evidence. The interpretation of the nuclear levels is particularly simple for low-lying configurations consisting of closed shells of neutrons and protons with only a single additional particle or with a single particle missing from such a closed configuration (a single hole). For nuclei with several particles outside closed shells, one might expect a rather complicated pattern of levels associated with the different ways of coupling the angular momenta of these particles. However, because of the pairing effect, one can obtain a qualitative description of the lowest states of an odd- A nucleus in terms of the orbits available to the unpaired odd particle. In this approximation, the degrees of freedom of the rest of the nucleons are neglected as these nucleons are assumed to remain in the paired state with $I^\pi = 0^+$. Most of the properties of the low-lying levels can be described by this assumption. However, the occurrence of additional levels in the low-energy spectra indicates the limitations of this simple description.

2.2 Mid-Shell Nuclei: Nilsson Model

A common feature of the nuclei which exhibit low lying rotational spectra is the existence of a “deformation”, which makes it possible to specify an orientation of the system as a whole. In a molecule, as in a solid body, the deformation reflects the highly anisotropic mass distribution, as viewed from the intrinsic coordinate frame defined by the equilibrium positions of the constituent atoms. In the nucleus, the rotational degrees of freedom are associated with the deformations in the nuclear equilibrium shape that result from the shell structure.

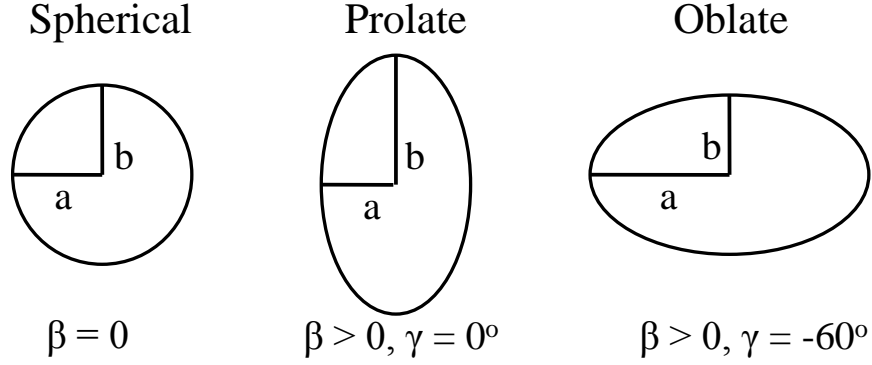


Figure 2.2: Schematic 2-d diagram of the three nuclear shapes (i) spherical (ii) prolate and (iii) oblate shape depending on the different values of the deformation parameters β and γ .

The experimental evidence of static nuclear deformation exists in nuclei in between the closed shells. Thus the spherical potential is can not be a good description and a deformed potential needs to be adopted [48, 49].

The deformation of the atomic nuclei is defined through the nuclear surface which is characterized by the surface coordinates $R(\theta, \phi)$ in terms of spherical harmonics $Y_{\lambda\mu}(\theta, \phi)$ as,

$$R(\theta, \phi) = R_0 \left(1 + \sum_{\lambda=0}^{\infty} \sum_{\mu=-\lambda}^{\lambda} \alpha_{\lambda\mu}^* Y_{\lambda\mu}(\theta, \phi) \right), \quad (2.1)$$

here, R_0 is the radius of a spherical nucleus having the same volume as deformed system and $\alpha_{\lambda\mu}^*$ represents the expansion coefficients.

For a nucleus with quadrupole deformation, $\lambda = 2$,

$$\alpha_{20} = \beta \cos \gamma, \quad \alpha_{21} = \alpha_{2-1} = 0, \quad \alpha_{22} = \alpha_{2-2} = \frac{1}{\sqrt{2}} \beta \sin \gamma, \quad (2.2)$$

where, the deformation β measures the extent of the quadrupole deformation and γ gives the degree of axial asymmetry. For $\gamma = 0^\circ$, 120° and 240° , the nucleus is extended

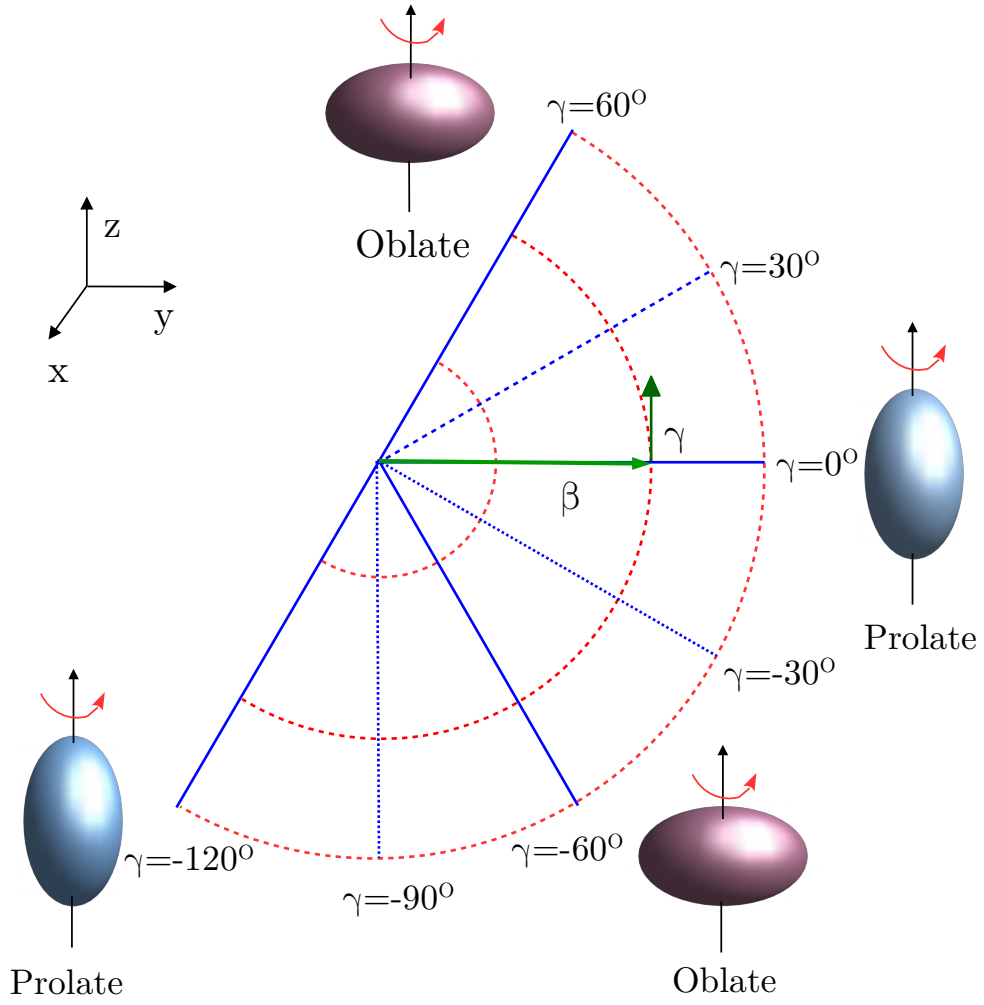


Figure 2.3: The different type of shapes of the nucleus depending upon the different β and γ values.

in the z -direction and compressed in x and y , which is called the prolate shape. For $\gamma = 60^\circ, 180^\circ$ and 300° , the nucleus assumes the oblate shape. $\gamma = 30^\circ, 150^\circ$ and 270° corresponds to the axially asymmetric shape.

The important quantities related to the quadrupole deformed nucleus are the moment of inertia and the quadrupole moment. Both the quantities can be written in terms of deformation as,

$$I = \frac{2}{5}AMR_0^2(1 + 0.31\beta) \quad (2.3)$$

and

$$Q_0 = \frac{3}{\sqrt{5\pi}} ZR_0^2\beta(1 + 0.16\beta). \quad (2.4)$$

The extended shell model calculation of the deformed nuclei can be done by assuming a modified harmonic oscillator potential. In an axially deformed nucleus, with deformation along the z axis, i. e., $x = y \neq z$, the Hamiltonian can be written as,

$$H = T + V = \frac{p^2}{2m} + \frac{1}{2}[\omega_x(x^2 + y^2) + \omega_z z^2] + Cl.s + Dl^2, \quad (2.5)$$

where, ω_x , ω_y and ω_z are the 1-d oscillators frequency in the x , y and z directions.

This deformed shell model is called the Nilsson model. The calculated single particle energy levels from the Nilsson model are labeled by,

$$K^\pi [Nn_z\Lambda],$$

where, K is the projection of the total angular momentum on the symmetry axis and π is the parity. The three quantum numbers inside the brackets are N , the principle quantum number of the major shell, n_z is the number of nodes in the wave function along the z direction and Λ is the component of the orbital angular momentum along the symmetry (z) axis. Thus, $K = \Lambda \pm \Sigma = \Lambda \pm 1/2$, where Σ is the projection of the spin angular momentum of nucleus on the symmetry axis. In the Nilsson model, the conserved quantities are K and π .

2.3 Nuclear Rotation

Many nuclei which are away from shell closure possess energy levels which form rotational bands similar to the bands observed in molecules. However, in nuclei there is no molecular skeleton to provide the inertia for the rotational motion. It is the nucleons themselves which generate it. As a consequence, nuclear rotation has features that are rather different from the rotation of molecules. For example, when we consider the rotation of a system composed of relatively few fermions at zero temperature, the moments of inertia deviate from the values for classically rotating solids or liquids. In addition, the rotational frequency (ω) can become comparable to the frequency of the nucleonic motion, which will then be substantially modified by inertial forces. The peculiarities of nuclear rotation become more evident in the high-spin regime. The rotational bands may terminate after a finite number of transitions. There may be uniform rotation about an axis, which is different from the principal axes of the density distribution. A nearly isotropic density distribution does not always prevent the appearance of rotational bands, which may be understood as the quantal rotation of a magnetic dipole. This section focuses on the features of rapidly rotating nuclei [46].

The total angular momentum of a rotating nuclei can be defined by the particle - core coupling,

$$\vec{I} = \vec{R} + \vec{J} \tag{2.6}$$

where \vec{J} is the intrinsic angular momentum and \vec{R} is the collective rotational angular momentum of the nucleus perpendicular to the symmetry axis. Such a system is rotational invariant about the symmetry axis and the component K of the total angular momentum \vec{I} is a constant of motion. The hamiltonian, for this system can be written in terms of intrinsic and collective hamiltonian as [62],

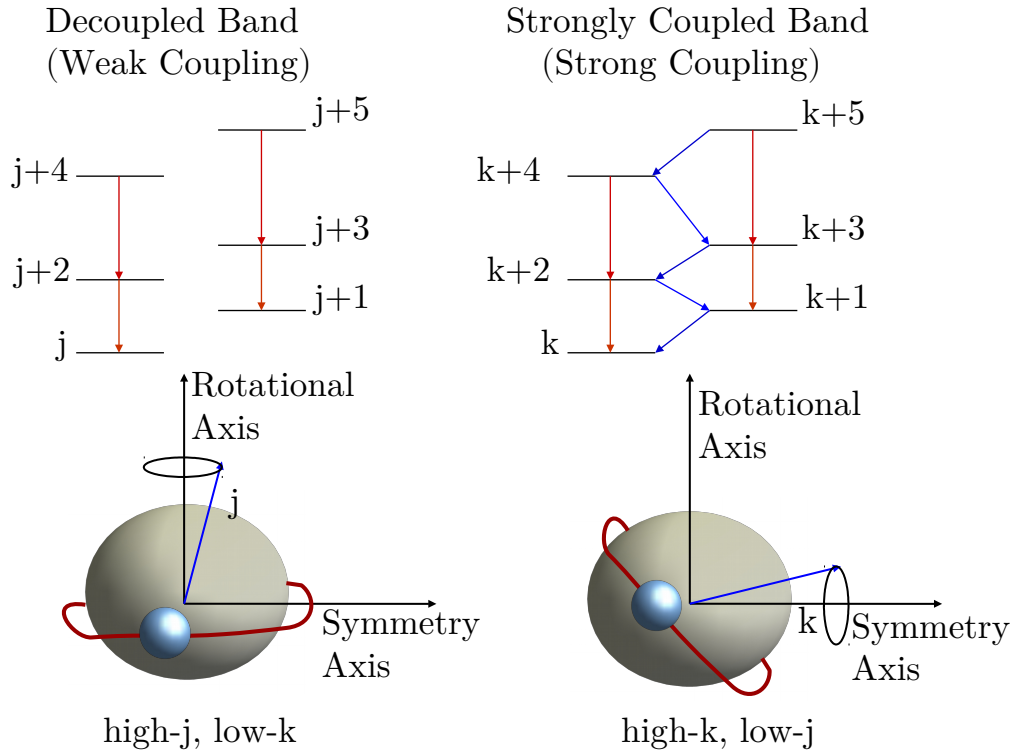


Figure 2.4: The angular momentum coupling of the single particle with the deformed core has been represented in the strong and weak coupling limit.

$$H = H_{col} + H_{intr} \quad (2.7)$$

where, H_{intr} is hamiltonian of the nucleons in the absence of collective rotation and using Eqn. 2.6, H_{col} can be written as,

$$H_{col} = \frac{\hbar^2}{2\mathfrak{J}}(\vec{I} - \vec{J})^2. \quad (2.8)$$

Here, \mathfrak{J} is the moment of inertia of the deformed core.

Now, the rotating hamiltonian is,

$$H_{col} = \frac{\hbar^2}{2\mathfrak{J}}[I(I+1) - K^2]. \quad (2.9)$$

In the absence of intrinsic particle motion ($K = 0$), the energies of the rotating nuclei is,

$$E_{rot} = \frac{\hbar^2}{2\mathfrak{J}_0} I(I + 1) \quad (2.10)$$

where, \mathfrak{J}_0 is the moment of inertia which remains fixed in case of an ideal rotor but in general, it varies with the rotational frequency. The rotational band can be formed on the ground state or on a single particle excited configuration. In the case of even - even nuclei, the intrinsic angular momentum component $K = 0$. Thus the excitation energies follows the $I(I + 1)$ pattern with $I = 0, 2, 4, 6, \dots$

The nuclei having odd mass number, the outer most odd nucleon can be coupled with the deformed core. The single particles can be coupled with the deformed core in two manners, the strong and the weak coupling schemes (Figure 2.4). In the strong coupling scheme, a rotational band with $\Delta I = 1$ is observed, where the collective angular momenta from the core (\vec{R}) is along the rotation axis (perpendicular to the symmetry axis) and the quasiparticle angular momenta is along the symmetry axis. On the other hand, in the weak coupling scheme, two $\Delta I = 2$ rotational bands are formed, in which the quasiparticle angular momentum is aligned to the rotation axis. The two rotational bands are characterized by the signature quantum number, which is discussed in the next section.

2.3.1 Principal axis rotation: The Cranking Model

The rotational symmetry of a nucleus breaks under deformation and the collective rotation around an axis perpendicular to the symmetry axis, was first described by Inglis [50, 51] within the framework of the Cranking Shell Model (CSM). The one dimensional cranking Hamiltonian is defined as,

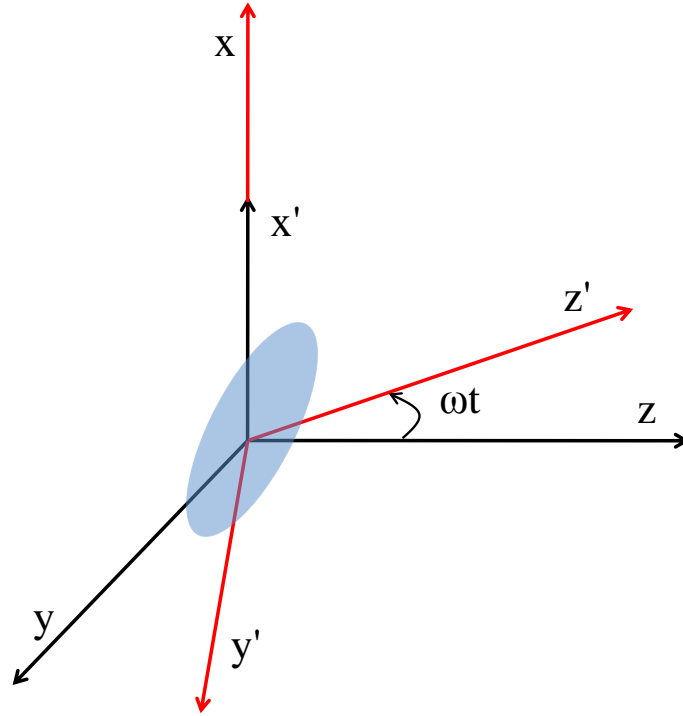


Figure 2.5: The schematic representation of the laboratory coordinate (x, y, z) and body-fixed (intrinsic) coordinate (x', y', z') system.

$$H^\omega = H_{intr} - \hbar\omega J_{x'}, \quad (2.11)$$

where, H^ω is Hamiltonian in the rotating frame, H_{intr} is the intrinsic Hamiltonian in the body-fixed frame and J'_x denotes the x component of the total angular momentum on the rotational axis.

The cranking Hamiltonian in Eqn. 2.11, breaks the time-reversal symmetry because of the presence of the $-\omega j_{x'}$ term. Therefore, Ω (the Nilsson quantum number, Λ) is no longer a good quantum number. The cranking Hamiltonian remains only parity invariant, which describes the symmetry under space inversion. The other symmetry is the invariance of H^ω under a rotation of 180° about the rotational axis (J'_x) and the corresponding operator is defined as,

$$\text{Re}'_x = e^{-i\pi J_{x'}}. \quad (2.12)$$

The eigenvalue of this operator can be written as,

$$r = e^{-i\pi\alpha}, \quad (2.13)$$

where, α is the signature quantum number which is conserved under the operation as in Eqn. 2.12. For integer value of spin I [46],

$$r = (-1)^I, \quad (2.14)$$

α is related to the nuclear spin by the relation [10],

$$I = \alpha \text{ mod } 2. \quad (2.15)$$

For the even number of nucleons $\alpha = 0$ or 1 ,

$$\begin{aligned} I = 0, 2, 4, 6, 8, \dots &\text{if } r = +1 \ (\alpha = 0) \\ &= 1, 3, 5, 7, 9, \dots &\text{if } r = -1 \ (\alpha = 1) \end{aligned} \quad (2.16)$$

while for the odd number of nucleons, $\alpha = \pm\frac{1}{2}$,

$$\begin{aligned} I = 1/2, 5/2, 9/2, \dots &\text{if } r = +i \ (\alpha = +1/2) \\ &= 3/2, 7/2, 11/2, \dots &\text{if } r = -i \ (\alpha = -1/2). \end{aligned} \quad (2.17)$$

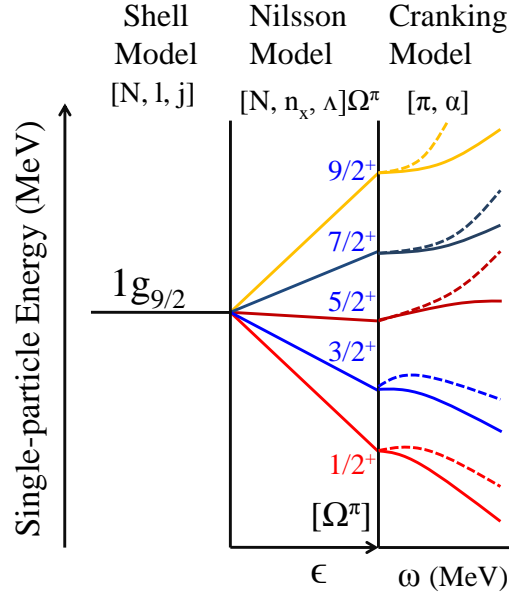


Figure 2.6: The effect of the deformed nuclear potential on a spherical shell model state, for example on $g_{9/2}$ state.

Thus, the rotational states of the nuclei are characterized with the parity π and the signature α .

The total nuclear routhian ξ , eigenvalue of the Eqn. 2.11, can also be expressed as the sum of the single-particle routhian e_μ as,

$$\xi = \sum e_\mu = \sum e_\mu^\omega + \hbar\omega \sum \langle \mu^\omega | j_{x'} | \mu^\omega \rangle, \quad (2.18)$$

where, $|\mu^\omega\rangle$ is the eigenstate of the cranking hamiltonian and e^ω is the expectation value of the single particle hamiltonian $h^\omega(i)$, which is defined as

$$H^\omega = \sum h^\omega = \sum h_{intr} - \sum \hbar\omega j_{x'}. \quad (2.19)$$

The single-particle routhian in equation 2.18 plotted as a function of ω in Figure 2.6, for the Nilsson potential with deformation parameter $\beta = 0.20$, $\gamma = 0^\circ$, which corresponds to the rotation of the axially symmetric prolate nucleus. The solid and dashed lines describe the states with the two signature quantum numbers. The aligned angular momentum $\langle \mu^\omega | j_{x'} | \mu^\omega \rangle$ can be estimated directly from the slope in the routhian, e_μ^ω :

$$\frac{de_\mu^\omega}{d\omega} = -\hbar \langle \mu^\omega | j_{x'} | \mu^\omega \rangle \quad (2.20)$$

But, the calculation of the total nuclear energy by the sum of the single-particle routhians does not provide an adequate description. In the presence of the pairing correlation and the shell correction, the total nuclear routhian is modified.

The modified total routhian $E_{tot,n}(Z, N, \beta)$ of a nucleus with deformation β and frequency ω can be calculated within the cranked Woods-Saxon Bogolyubov-Strutinsky approach [10, 25, 63] framework [10, 25, 63], which utilizes the macroscopic-microscopic shell correction developed by Strutinsky [10, 64]. Within this framework, the total energy of an n-quasiparticle configuration is given by,

$$E_{tot,n}(Z, N, \beta) = E_{macr}(Z, N, \beta) + E_{micr,n}(Z, N, \beta), \quad (2.21)$$

where, β implies for the complete set of the deformation parameters. The macroscopic part represents the bulk properties of the nucleus approximated by a liquid-drop model of the atomic nuclei. The microscopic part $E_{micr,n}$ can be divided into two parts: a contribution from the shell correction energy, E_{shell} and the pairing correlation, E_{pair} , both of which depend on the number of quasiparticles.

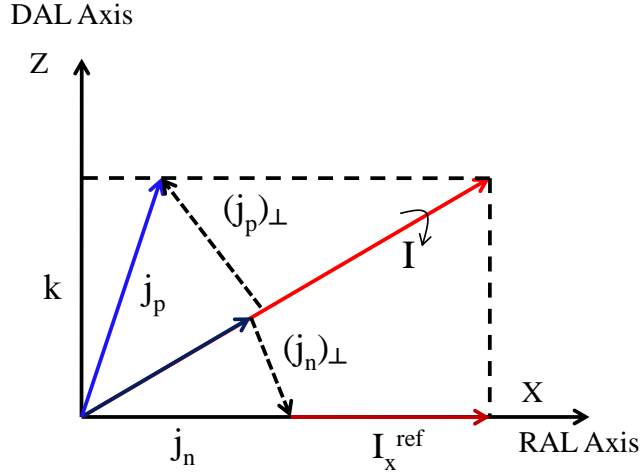


Figure 2.7: The quasi-particle coupling scheme of three quasiparticles configuration in Dönau model. Here, two quasiparticles supposed to be rotationally aligned (RAL) and the remaining one is assumed as deformed aligned (DAL). The magnetic dipole transitions are governed by the resultant perpendicular components of the magnetic moments of the quasiparticles.

2.3.1.1 Magnetic Dipole Transition Strengths: Dönau Model

The intrinsic representation of the multipole operator of radiation is derived based on the idea of the rotor-plus-quasi-particle coupling. This method can be applied to one and more high- j quasi-particle configuration via a semi-classical vector coupling scheme for the calculation of the transition strength of magnetic dipole ($M1$) transition. Considering a case of the axial prolate deformed nucleus, the particle angular momentum is aligned along the rotational axis (RAL). This direction corresponds to a maximal overlap of its doughnut shape-like mass distribution with the attractive potential, i. e., a condition of minimal energy. The angular momentum produced by the hole in a high- j orbital will align parallel to the symmetry axis or the deformed axis (DAL). This direction corresponds to the minimal overlap of the doughnut-like mass distribution with the repulsive potential. The roles of the particles and holes will reverse when the deformation of the nuclei becomes oblate. The vector diagram of the quasi-particle coupling scheme is shown in Figure 2.7. According to the semi-classical theory of Dönau [65], the intra-band $M1$ transition rate is given by

$$B(M1, I \rightarrow I-1) = \frac{3}{8\pi} \frac{1}{I^2} [(g^{(1)} - g_R)(\Omega^{(1)} \sqrt{I^2 - K^2} - i^{(1)} K) + (g^{(2)} - g_R)(\Omega^{(2)} \sqrt{I^2 - K^2} - i^{(2)} K)]^2, \quad (2.22)$$

where, $K = \Omega^{(1)} + \Omega^{(2)}$, the superscripts (1) and (2) stand for the deformation and rotational aligned configurations of the quasi-particles, respectively [65] and g 's are the g -factors of the orbital involved, g_R is the g -factor from the collective contribution of the nucleons, defined as, Z/A [66]. If the configurations involve more than one particles, effective g -factors can be represented as

$$g^{(2)} = \frac{\sum_i g_{\Omega_i} \Omega_i}{K}. \quad (2.23)$$

The better fit to the data can also be obtained when one rewrites Eqn. 2.22 in terms of a two quasiparticle configuration (2QP), where the two quasi-particles are not distinguishable but form a common structures [67]:

$$B(M1, I \rightarrow I - 1) = \frac{3}{8\pi} \frac{1}{I^2} [(g^{2QP} - g_R)(K \sqrt{I^2 - K^2} - i^{2QP} K)]^2. \quad (2.24)$$

The advantage of considering the 2QP configuration is that one can get i^{2QP} from the experimental alignment (i_x) plot and the g^{2QP} can be calculated using the g -factor coupling Eqn. 2.23.

2.3.1.2 Comparison of the Theoretical Calculation with Experimental Results

It is desired to correlate experimentally measured quantity to the theoretical estimation. But, it is not possible for the cranking model calculations as the model is based on the body fixed frame while all the observables are in the laboratory frame. Thus, the

comparison can only be achieved in the semiclassical approximation by transforming the experimental excitation energies and angular momentum into the intrinsic frame of the rotating nuclei. The excitation energy in the rotating frame i. e., the routhian ($E'(\omega)$) is [10, 68],

$$E'(\omega) = E - \omega I_x. \quad (2.25)$$

The rotational frequency ω corresponding to a transition between the angular momentum states $I + 1$ and $I - 1$ can be written as,

$$\hbar\omega(I) = \frac{dE(I)}{dI_x(I)} \quad (2.26)$$

where I_x is the component of angular momentum along the rotational axis which can be calculated using the relation [68],

$$I_x = \sqrt{I(I+1) - K^2} \approx \sqrt{\left(I + \frac{1}{2}\right)^2 - K^2}. \quad (2.27)$$

The rotational frequency ω can be approximated by the Eqn. 2.26 as,

$$\hbar\omega(I) \approx \frac{E(I+1) - E(I-1)}{I_x(I+1) - I_x(I-1)}. \quad (2.28)$$

The total experimental Routhian [$E'(\omega)$] as in Eqn. 2.25 with the measured angular momentum is then expressed as,

$$E'(\omega) = \frac{1}{2}[E(I+1) + E(I-1)] - \hbar\omega I_x(I), \quad (2.29)$$

where the average value of $E(I+1)$ and $E(I-1)$ is an approximation for $E(I)$.

The total routhian comprise of the energies from the collective and the quasiparticle contribution. The quasi-particle Routhian energy (e') and aligned angular momentum (i_x) are obtained by subtracting the collective contribution from the absolute values [68],

$$e'(\omega) = E'(\omega) - E_{ref}(\omega) \quad (2.30)$$

and

$$i(\omega) = I_x(\omega) - I_{x,ref}(\omega), \quad (2.31)$$

respectively, where the aligned angular momentum due to the core

$$I_{x,ref}(\omega) = (J_0 + \omega^2 J_1)\omega \quad (2.32)$$

and the collective energy

$$E_{ref}(\omega) = -\frac{1}{2}\omega^2 J_0 - \frac{1}{4}\omega^4 J_1 + \frac{\hbar^2}{8J_0}. \quad (2.33)$$

The J_0 and J_1 are the Harris parameters [69] and are obtained by fitting the ground state band of the nearest even-even nucleus, which originates purely from collective rotation.

These conversions allow the comparison of experimental quasiparticle routhian (e') and aligned angular momentum (I_x) with the cranking model calculations.

In general, the deviation from the axially symmetric shape of an atomic nucleus is expected at higher angular momentum [11]. This deviation results in a number of observables. For a nucleus having stable triaxiality, the rotational motion is possible about all the three axes. Thus, the rotational spectra of a triaxial nuclei are richer compared

to the axially symmetric nuclei. In addition, spin Chirality [4] and the Wobbling motion [46, 70] are the phenomena which have been uniquely associated with the stable triaxial shape in the nuclei.

2.4 Exotic Modes of Excitation

The phenomenon of spontaneous symmetry breaking is one of the main paradigms in physics. The spontaneous breaking occurs if a system, in its quest to attain the minimal energy, chooses a symmetry-violating state even though the underlying interactions are invariant under the concerned symmetry. Nevertheless, it is the nature of the interactions that determines which symmetries are broken and under which conditions. Therefore, the study of symmetry-violating states brings one closer to the understanding of the fundamental interactions. In the nuclear structure physics, one important example of spontaneous symmetry breaking is the existence of deformed nuclei. The departure from the spherical invariance leads to the appearance of the rotational bands. Depending on the conservation or violation of other symmetries, like the plane of reflection, the bands can have different structures, leading to the different types of the excitation mechanisms [3], which have been discussed in the following sub-sections.

2.4.1 Magnetic rotation

In the last few decades, rotational like sequence of gamma transitions have been found in near-spherical nuclei $^{197-200}\text{Pb}$ consisting of $M1$ transitions with weak or absent $E2$ cross-over transitions [1]. The weak or missing stretched $E2$ transitions indicate a small deformation. The spectrum of these rotational like dipole bands are similar to the spectrum of the super-deformed rotational band as shown in Figure 1 of reference [1], which is the best-known example of collective rotation in nuclei. At lower angular momentum, the observed level spacing is indicative of single-particle excitations. The appearance of

these regular band like structure occur for spin $I > 10$, when high- j orbitals have been involved. Till now, more than 175 bands possessing such properties have been observed in more than 60 weakly deformed nuclei [1, 2, 29, 30, 37].

The general feature of these bands summarize as follows

1. The energy of the states in these bands nearly follows the rotational like behavior $E(I) - E_0 \sim (I - I_0)^2$, where E_0 and I_0 are the band-head energy and spin, respectively [1].

2. The in-band transitions are magnetic dipole ($M1$) in nature and the cross-over stretched $E2$ transitions are either weak or missing. The reduced transition probability of the dipole transitions $[B(M1)]$ is large ($\sim 1 - 10 \mu_N^2$) and decreases with increase in angular momentum. The quadrupole transition strength $[B(E2)]$ lies in the range of $0.1 e^2 b^2$ or less implying small deformation ($\beta < 0.1$) and decreases with increase in angular momentum.

3. The ratio of the reduced transition probability of the $M1$ and $E2$ transitions, $B(M1)/B(E2)$ values are large ($\geq 20 \mu_N^2 (eb)^{-2}$).

4. The ratio of the dynamic moment of inertia and electric quadrupole transition probability ($\mathcal{J}^{(2)}/B(E2)$) is larger than $150 \hbar^2 \text{MeV}^{-1} (eb)^{-2}$, which is substantially higher compared to the value for well-deformed nuclei ($\sim 10 \hbar^2 \text{MeV}^{-1} (eb)^{-2}$) or for superdeformed nuclei ($\sim 5 \hbar^2 \text{MeV}^{-1} (eb)^{-2}$).

Initially, the bands in the Pb region were wrongly interpreted as based on proton configurations (involving $h_{9/2}$ and $i_{13/2}$ orbitals) with large components of their angular momenta along the deformed axis i.e., the non-collective rotation. But, the salient features of these bands, lead to the proposition that the structures may arise from a new excitation mechanism of angular momentum generations in atomic nucleus. A theoretical description of these $\Delta I = 1$ rotational bands (Magnetic Rotational (MR) bands) based on shears mechanism, was proposed by Frauendorf within the framework of the tilted axis cranking (TAC) calculations [11, 71]. Later, Macchiavelli *et al.* [1] developed a

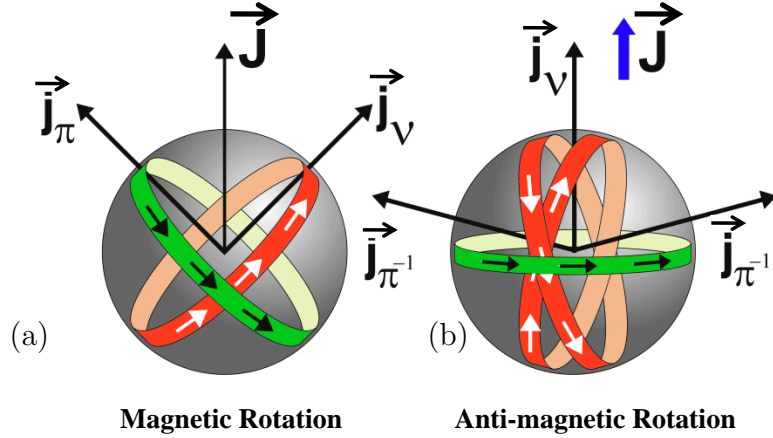


Figure 2.8: The schematic representation of the coupling scheme between the angular momentum vector for MR and AMR in the framework of the shears mechanism adopted from ref. [38].

semi-classical model for the angular momentum generation in these dipole bands and the $B(M1)$ and $B(E2)$ rates, based on the effective interaction between the neutron and the proton quasi-particles. It was also observed, that a small contribution from the core plays a crucial role and the interplay between the quasiparticles and core angular momentum led to an alternative framework called Shears mechanism with Principal Axis Cranking (SPAC) model [6–8].

2.4.1.1 Shears Mechanism

In weakly deformed nuclei, the angular momenta of the proton particles (holes) and neutron holes (particles) align perpendicular to each other as represented by the vector \vec{j}_π and \vec{j}_ν in Figure 2.8 (a) and (b). The high- j orbitals have toroidal mass density distributions, which are demonstrated by the two loops [3]. The repulsive interaction between the particles and the holes favors this perpendicular alignment, which ensures the smallest spatial overlap between the two loops. The total angular momentum along the band is generated by the gradual alignment of \vec{j}_π and \vec{j}_ν . This process is called the shears mechanism because of it resembles with the motion of the closing of a pair of sheep-shears, which have a spring to keep the blades of the shears open. Thus, the

dipole bands are also known as the shears bands.

The particular arrangement of the high- j orbitals in the shears mechanism gives rise to a large transverse component of the magnetic dipole moment (μ_{\perp}) shown in Figure 2.9. The proton sector contribute to the total magnetic dipole moment (μ_{tot}) both from the orbital part and the spin part ($g_{\pi} > 0$) to the magnetic moment, which is parallel to proton angular momentum \vec{j}_{π} and large in magnitude. On the other hand, the neutrons contribute by the spin part only, which is anti-parallel to neutron angular momentum ($g_{\nu} < 0$) and is small in magnitude. Thus, the added transverse components of μ_{tot} is along the direction of proton angular momentum that rotates and generates the strong magnetic dipole radiation. The magnetic dipole moment is the order parameter, which specifies the orientation angle between the \vec{j}_{π} and \vec{j}_{ν} . Frauendorf *et al.* [72, 73] has suggested calling this excitation mechanism of angular momentum generation as ‘magnetic rotation’.

As the pair of shears blades formed by \vec{j}_{π} and \vec{j}_{ν} close, the magnitude of the transverse component of magnetic dipole moment (μ_{\perp}) decreases (Figure 2.9) resulting in the decrease of the reduced transition probability according to the relation [1],

$$B(M1, I \rightarrow I - 1) = \frac{3}{8\pi} \mu_{\perp}^2 = \frac{3}{8\pi} g_{eff}^2 j_{\pi}^2 \sin^2 \theta_{\pi} (\mu_N^2), \quad (2.34)$$

where $g_{eff} = g_{\pi} - g_{\nu}$ is the effective gyromagnetic factor.

An expression for $B(E2, I \rightarrow I - 2)$ value, which is proportional to the square of the electric quadrupole tensor can be written as,

$$B(E2, I \rightarrow I - 2) = \frac{5}{16\pi} (eQ)_{eff}^2 \frac{3}{8} \sin^4 \theta_{\pi} (e^2 b^2), \quad (2.35)$$

where $(eQ)_{eff} = e_{\pi} Q_{\pi} + \frac{j_{\pi}^2}{j_{\nu}^2} e_{\nu} Q_{\nu}$, Q_{eff} is effective quadrupole moments of proton and neutron quasiparticles. The $B(E2)$ values also decrease as the shears close because the

charge distribution tends to become more symmetric around the rotation axis.

2.4.1.2 Shears Mechanism with Principal Axis Cranking Model

The shears mechanism represents an excitation mechanism that is fundamentally different from collective rotation. Generally, one may expect these two modes to compete and it is important to establish when and how they will dominate.

Recently, number of MR bands have been observed in which the states have the notable contribution of core rotational angular momentum to the total angular momentum vector. Several efforts have been made to take into account the core rotation into the shears mechanism and an extra term representing the rotational energy of the core is added to a total energy of the excited state of spin I . The total energy of the excited state is expressed as [6],

$$E(I) = E(\text{core}) + E(\text{shears}) + \text{constants}. \quad (2.36)$$

Here the first term represents the core contribution to the energy $E(I)$ and expressed as

$$E(\text{core}) = \frac{R^2(I, \theta_\pi, \theta_\nu)}{2\mathcal{I}} \quad (2.37)$$

and

$$E(\text{shears}) = v_2 P_2(\cos(\theta_\pi - \theta_\nu)) \quad (2.38)$$

is the interaction energy between the shears blade j_π and j_ν , and v_2 is the total particle-hole interaction strength, whereas, R is the core angular momentum expressed as [6],

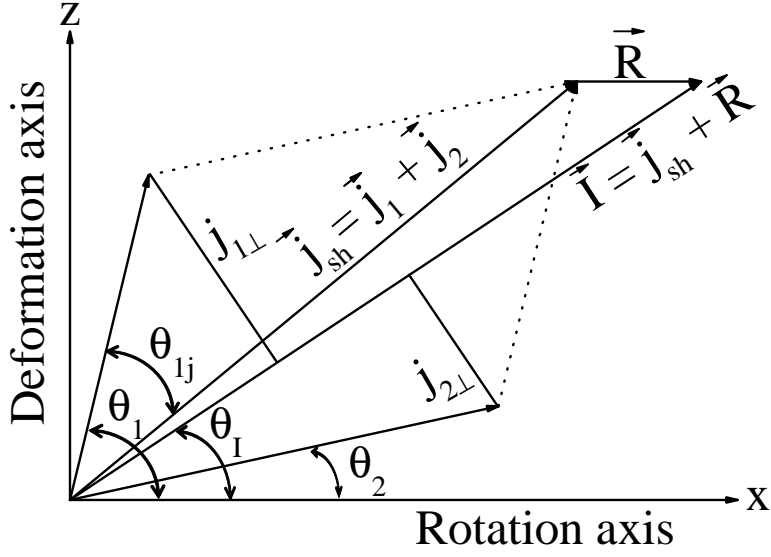


Figure 2.9: The angular momentum coupling scheme in the framework of shears mechanism for the initial alignment. The notations used have been explained in the text.

$$R = \sqrt{I^2 - (j_1 \sin \theta_1 + j_2 \sin \theta_2)^2} - j_1 \cos \theta_1 - j_2 \cos \theta_2. \quad (2.39)$$

Here θ_1 and θ_2 are the angles of j_1 and j_2 blades with the rotation axis. This geometrical model is called Shears mechanism with the Principal Axis Cranking (SPAC). In recent times, the SPAC model has been established as an important tool to explore the quasiparticle configurations, intrinsic character and rotational contribution of the deformed core in the shears band structure. The experimental energy (E_γ), spin (I), rotational frequency (ω), $B(M1)$ and $B(E2)$ values of the MR bands for weakly deformed nuclei in $A \sim 100, 140$ and 200 regions have been well reproduced in the framework of the SPAC model [7, 8, 32, 37].

In the framework of SPAC model, the $B(M1)$ values can be written as [6],

$$B(M1, I \rightarrow I - 1) = \frac{3}{8\pi} [j_\pi g_\pi^* \sin(\theta_\pi) - \theta_I - j_\nu g_\nu^* \sin(\theta_I) - \theta_\nu]^2, \quad (2.40)$$

where $g_\pi^* = g_\pi - g_R$, $g_\nu^* = g_\nu - g_R$ and $g_R = (Z/A)$; Z and A are the atomic and

mass number of the nucleus, respectively. The θ_I and θ_π are the angle between the total angular momentum vector (I) and the proton angular momentum vector with the rotational axis, respectively.

The $B(E2)$ rates can be written within the framework of SPAC as

$$B(E2, I \rightarrow I - 2) = \frac{15}{128\pi} [(eQ)_{eff} \sin^2 \theta_\pi + (eQ)_{coll} \cos^2 \theta_I] \quad (2.41)$$

where Q_{eff} and Q_{coll} are the quasiparticle and collective quadrupole moments of the nuclei, respectively.

The total energy in Eqn. 2.36 is minimum for each value of I , θ_1 and θ_2 and the minimization condition is,

$$\frac{\partial^2 E(I, \theta_1, \theta_2)}{\partial \theta_1 \partial \theta_2} = 0. \quad (2.42)$$

In general, any orientation of j_1 and j_2 is possible. For the normal initial alignment [7, 8], the direction of j_2 is along the rotational axis. Thus the two-dimensional energy minimization condition of energy is replaced by one-dimensional minimization condition as,

$$\frac{\partial E(I, \theta_1)}{\partial \theta_1} = 0, \quad (2.43)$$

which is then used to obtain the θ_1 value for each excited state with angular momentum I .

To get quantitative measures of the core rotation to the total angular momentum, a dimensionless quantity $\chi = \frac{J(I)}{j_1^2/3v_2}$ can be calculated, which determines the rotational contribution from the deformed core in the shears structure. The reduced energy, ($\hat{E}(\hat{I}) = E(I) \frac{J(I)}{2j_1^2}$) and reduced spin ($\hat{I} = I/2j_1$) can be introduced in Eqn. 2.36 as,

$$\hat{E}(\hat{I}) = \hat{I}^2 + \frac{1+a^2}{4} - \frac{1}{2} \left[\sqrt{4\hat{I}^2 - \sin^2 \theta_1} (a + \cos \theta_1) + \sin^2 \theta_1 \right] + \frac{a}{2} \cos \theta_1 + \frac{\chi}{4} \cos \theta_1 - \frac{\chi}{12} \quad (2.44)$$

where $a = j_2/j_1$ represents asymmetry in the angular momentum blades.

The shears angle (θ_1) between the angular momentum vectors (\vec{j}_1 and \vec{j}_2) can be obtained for each value of the reduced angular momentum \hat{I} from the reduced energy minimization condition [6],

$$\sqrt{4\hat{I}^2 - \sin^2 \theta_1} + \frac{\cos \theta_1 (a + \cos \theta_1)}{\sqrt{4\hat{I}^2 - \sin^2 \theta_1}} - (2 + \chi) \cos \theta_1 - a = 0. \quad (2.45)$$

The reduced rotational frequency ($\hat{\omega}$) with reduced spin (\hat{I}) can be calculated by,

$$\hat{\omega} = 2\hat{I} \left(1 - \chi + \frac{\sqrt{4\hat{I}^2 - \sin^2 \theta_1} - a}{\cos \theta_1} \right). \quad (2.46)$$

The value of the shears angle (θ_1) obtained from energy minimization is used to calculate the reduced transitions probabilities $B(M1)$ and $B(E2)$ following Eqns. 2.40 and 2.41, respectively. This provides the self consistency check of the calculation.

The advantage of this modified model over the SPAC model is the reduction in the number of free parameters. For the values of $\chi < 0.5$ shear mechanism dominates and for $\chi > 0.5$ core rotation dominates for the generation of angular momentum in the MR band [6].

2.4.2 Antimagnetic Rotation

A special case of rotational-like spectra consisting of stretched $E2$ transition in the weakly deformed nuclei has been observed Cd, Pd nuclei in mass $A \sim 110$ [38–41, 74, 75]

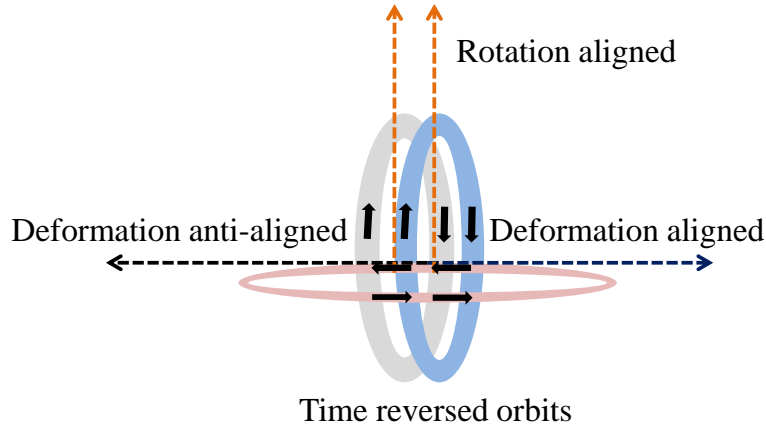


Figure 2.10: The angular momentum coupling scheme in the framework of shears mechanism for AMR phenomenon.

region and in ^{143}Eu outside the $A \sim 110$ region [42]. The strength of the reduced transition probability $B(E2)$, has been found to decrease with spin [74]. Here, the angular momentum is generated by two back to back shears-like configurations of valence particles and holes, termed as double shears structure, which has π rotational symmetry about the axis of total angular momentum. The high spin states along the band are generated by the simultaneous closing of the two blades of the conjugate shears. The transverse magnetic dipole moment (μ_{\perp}) produced by each shear are anti-aligned and they cancel out. This situation resembles with the antiferromagnetic substance where one half of the atomic dipole moments are aligned on one sublattice and the other half are aligned in the opposite direction on the other sublattice in the crystalline structure (Figure 2.10). Due to this similarity, the mechanism of generating a $E2$ rotational like band is called antimagnetic rotation (AMR). As the shears close $B(E2)$ transition rates decrease with increasing spin according to Eqn 2.35. At the band head, these valence holes are initially aligned in time-reversed orbits. Since the conjugate shears have π rotational symmetry about the axis of total angular momentum, the rotational band consist of a sequence of energy levels with $\Delta I = 2\hbar$. The levels in the band decay by a weak $E2$ transition as the deformation of the nuclei is very small [2, 3].

2.4.2.1 Semi-classical particles-plus-rotor model

A classical particles-plus-rotor model was conceived by Macchiavelli *et al.* to study the competition between the shears mechanism and the core rotation, discussed in the earlier section [6]. The total energy was expressed in Eqn. 2.36 as the sum of the rotational energy of the core and an effective interaction $V_2 P_2(\theta)$ between the blades. This model can be extended for anti-magnetic rotation and the total energy $E(I)$ of a state of spin I can be expressed in this model as [7],

$$E(I) = \frac{(\mathbf{I} - \mathbf{j}_\pi - \mathbf{j}_\nu)^2}{2\mathcal{I}} + \frac{V_{\pi\nu}}{2} P_2(\cos\theta) + \frac{V_{\pi\nu}}{2} P_2(\cos(-\theta)) - \frac{V_{\pi\pi}}{n} (P_2(\cos 2\theta) - 1), \quad (2.47)$$

where, $V_{\pi\pi}$ and $V_{\pi\nu}$ symbolize the attractive particle-particle and the repulsive particle-hole interaction strengths, respectively, and ‘ n ’ is the scaling factor between $V_{\pi\pi}$ and $V_{\pi\nu}$ which is calculated from the number of particle-hole pairs for a single particle configuration [40, 41]. The effective interaction for the particle-particle combination is 0 at $\theta = 0$ which is accomplished by the functional form ‘ $P_2(\cos\theta) - 1$ ’ of the interaction [7].

From Eqn 2.47 and by the energy minimization condition $[\frac{dE}{d\theta}]_I = 0$, the total angular momentum is

$$I = aj + 2j\cos\theta + \frac{1.5\mathcal{I}V_{\pi\nu}\cos\theta}{j} - \frac{6\mathcal{I}V_{\pi\pi}\cos 2\theta\cos\theta}{nj}, \quad (2.48)$$

where, $j_\nu = aj_\pi = aj$ [40, 41]. The rotational frequency ω is calculated from Eqns 2.47 and 2.48 using $\omega = \frac{dE}{dI} = [\frac{dE}{d\theta}]/[\frac{dI}{d\theta}]$ relation

$$\omega = \frac{1.5V_{\pi\nu}\cos\theta}{j} - \frac{6V_{\pi\pi}\cos 2\theta\cos\theta}{nj}. \quad (2.49)$$

The angular momentum state for a given energy and the corresponding $B(E2)$ transition strength and rotational frequency ω can be calculated using the Eqns 2.35 and 2.49.

2.4.3 Chiral Symmetry Breaking

The occurrence of spin chirality in nuclei was first predicted in the year 1997 by Frauendorf and Meng [4]. This phenomenon is expected to occur in triaxially deformed nuclei in which there are high- j valence particles and holes. The triaxial nuclei have three mutually perpendicular axes namely short (s), intermediate (m) and large (l). The angular momentum contribution from the valence particles, \mathbf{j}_p , is aligned along the short axis because of the torus-like density distribution of the gives the maximum overlap with the triaxial core. The high- j hole angular momentum \mathbf{j}_h tends to align along the large axis because its dumbbell shape density distribution has maximum overlap with the triaxial core. The core angular momentum vector \mathbf{R} tends to align along the intermediate axis, which leads to the largest moment of inertia. These three mutually perpendicular angular momenta in the lab frame can form two systems of opposite handedness, right-handed and left-handed depending upon the direction of the core angular momenta \mathbf{R} . The total angular momentum, \mathbf{J} does not lie in any of the plane of the three angular momentum vectors \mathbf{j}_p , \mathbf{j}_h and \mathbf{R} . The two systems transform into each other by a combination of time-reversal operator and rotation by 180° , $\chi = TR(\pi)$. The restoration of the chiral symmetry in the laboratory frame results in degenerate doublet dipole $\Delta I = 1$ bands of the same parity. The formation of the chiral geometry may be a dynamical process as a function of spin. At the bandhead where the core angular momentum \mathbf{R} is small, the total angular momentum \mathbf{J} lies on the principal plane formed by \mathbf{j}_p and \mathbf{j}_h . As the spin increases, \mathbf{R} becomes comparable to the \mathbf{j}_p and \mathbf{j}_h , and the \mathbf{J} turns aplanar from planar. With further increase in spin, the total angular momentum vector \mathbf{J} may slowly align towards the rotational axis and became planar again.

The first experimental evidence of nuclear chiral doublet bands as in ^{134}Pr [76] where a doublet band is observed based on the $\pi h_{11/2}^{+1} \otimes \nu h_{11/2}^{-1}$ configuration and its partner band but without any interpretation of spin chirality.

A number of experimental fingerprints have been suggested for spin chirality:

1. Observation of nearly degenerate dipole band of same spin and parity based on the same single-particle configuration. Near the bandhead, there is larger energy separation between the doublet bands due to the admixtures of the planer solution.

2. Chiral doublet bands should show smooth variation in energy i.e., there is no staggering of the quantity $S(I)$ defined as $S(I) = [E(I) - E(I - 1)]/2I$ i.e., $S(I)$ should be independent of spin in the chiral region because of the absence of Coriolis interaction between perpendicularly aligned core and particle-hole angular momenta.

3. The inband reduced transitions probabilities $B(M1)$ and $B(E2)$ strength are very similar to the partner band and show characteristic staggering of the ratio of $B(M1)/B(E2)$ implying the same configurations of the doublet band.

4. All the physical observables like quasiparticle alignment, the moment of inertia and other electromagnetic properties should be similar for the chiral doublets bands.

2.4.4 Octupole Deformation and Correlations

The quadrupole deformation is a common phenomenon for atomic nuclei. The next relevant moment is the octupole, which leads to the spontaneous breaking of intrinsic reflection symmetry in nuclei with pear-like shapes. This has been explored in recent years both from the experimental and the theoretical observations in the actinide nuclei. The experimental footprints for such reflection-asymmetric nuclear shapes are the appearance of ground-state rotational bands of alternating parity with enhanced in-band $E1$ transitions between the levels of alternating parity. The $B(E1)$ values in the actinide

mass regions range from 10^{-4} to 10^{-2} s. p. u. (typical values of $B(E1)$ is lesser than 10^{-6}). The nuclear dipole moment is the measure of the shift between the center of mass and the center of charge of the nucleus. For the reflection symmetric system both mass and charge center coincides and results in no intrinsic dipole moment of the nuclei. But, the reflection asymmetric density distribution can lead to a large static electric dipole moment. Such a dipole moment manifests in an enhanced $E1$ transition strength between the opposite parity bands [5, 36]. For an axially deformed system $\langle x \rangle = \langle y \rangle = 0$ and the intrinsic dipole moment is aligned along the deformed axis (z -axis). Assuming the axial shape of the nuclei, there is a simple relationship between reduced transition probability $B(E1)$ and intrinsic dipole moment D_0 of state I [77]

$$B(E1; IK \rightarrow I'K) = \frac{3}{4\pi} D_0^2 \langle IK10 | I'K \rangle^2. \quad (2.50)$$

However, in most of the situation experimental determination $B(E1)$ value may not be possible, D_0 value can be extracted from the $B(E1)/B(E2)$ branching ratios. The $B(E2)$ rates are given by,

$$B(E2) = \frac{5}{16\pi} Q_0^2 \langle IK20 | I'K \rangle^2, \quad (2.51)$$

where Q_0 is the intrinsic quadrupole moment assumed to be constant throughout the band and can be determined from the $B(E2)$ rates for the $2^+ \rightarrow 0^+$ or $3^- \rightarrow 1^-$ transitions.

The alternating-parity band is the characteristic for reflection-asymmetric nuclear shapes. This can be explored more quantitatively by plotting the energy difference δE between the opposite parity bands as proposed by Nazarewicz and Olanders [78]

$$\delta E = E(I^-) - \frac{(I+1)E((I-1)^+) + IE((I+1)^-)}{2I+1}. \quad (2.52)$$

The rotational frequency ratio is defined by the relation,

$$\frac{\omega_-(I^-)}{\omega_+(I^+)} = 2 \frac{E((I+1)^+) - E((I-1)^-)}{E((I+2)^+) - E((I-2)^+)}. \quad (2.53)$$

In the limit of the stable octupole deformation, $\delta E(I)$ should be close to zero and the frequency ratio should approach to one. These limiting values have been observed for $^{222,224,226}\text{Th}$, which are the best candidates for a stable octupole deformation [79]. However, for the transitional nuclei $^{228,230,232}\text{Th}$, $\delta E(I)$ varies linearly with I and appear to undershoot the limit $\delta E(I) = 0$. The ratio $\omega_-(I^-)/\omega_+(I^+)$ saturates to 0.8 for high spin. A comparison of D_0 value for the Thorium isotopes $^{222,224,226}\text{Th}$ establishes stable octupole deformation (D_0 large) while $^{228,230,232}\text{Th}$ are proposed to be octupole soft/octupole vibration like structures [79]. The static octupole deformation is very scarce and has been observed in few even radium and thorium isotopes around $A \sim 224$ [79] and in ^{144}Ba [80]. The reflection asymmetric bands can also arise due to the octupole coupling between intruder orbital (l, j) and normal parity subshell ($l-3, j-3$) near the fermi energy surface. The dynamical interaction between these orbitals called “octupole correlation”, can lead to the reflection symmetry breaking bands connected by enhanced $E1$ transitions [5, 36].

2.5 Summary

In summary, the different aspects of nuclear models are explored in this chapter. The properties of the shell closure nuclei have been discussed. A basic description of the deformed shell model (Nilsson model) and cranking shell model have been presented. These model predictions are used for the comparison with experimental results. At the end, different exotic excitation mechanisms like, shears mechanism, chiral symmetry breaking, octupole deformation and correlation have been reviewed. The next chapter describes the different experimental techniques used for nuclear structure studies at high

spin.

CHAPTER 3

Experimental Techniques and Data Analysis

The detailed understanding of the finite many-body quantal system, nucleus, could be possible by studying its behavior at extreme conditions like high excitation energy and angular momentum. The fusion between two nuclei results in a compound nucleus with high angular momentum and high excitation energy and by measuring the various characteristics of the discrete γ transitions of the residual nuclei, we can study the nuclear structure at high angular momentum.

3.1 Fusion Evaporation Reaction

For the population of the high spin states of nuclei one needs a reaction that will impart the maximum angular momentum to the nucleus under study. The fusion evaporation reaction is the most suitable one for populating the high angular momentum states. The angular momentum transfer to the compound system can be estimated by the classical relation $L = r \times P$, where, r is the impact parameter of the reaction and P are the linear momentum of the incident particle in the Center of Mass (CM) frame. Thus, higher the incident momentum P larger is the angular momentum transfer, which implies that the heavy-ion induced fusion is more favorable.

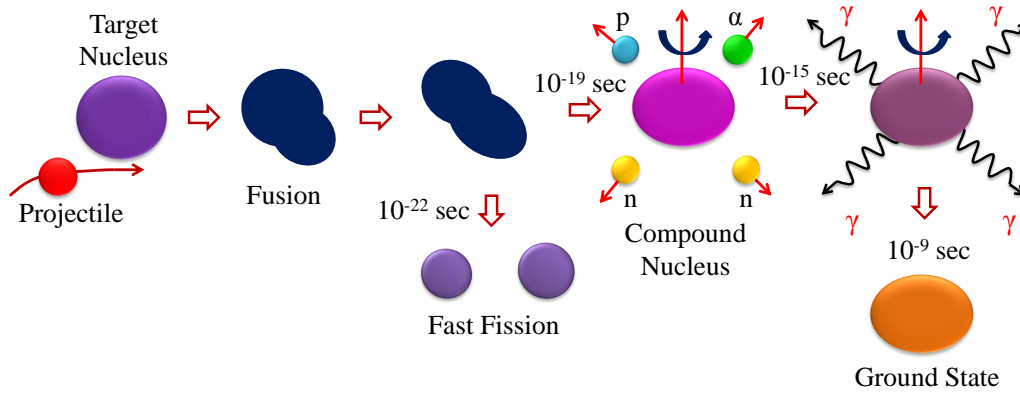


Figure 3.1: The representation of different steps involved to the heavy-ion incident fusion-evaporation reaction.

In the fusion evaporation reaction, the incident projectile and the target nuclei fuse together within $\approx 10^{-20}$ sec to form a compound nucleus. The incident projectile energy in the center of mass frame is converted into the excitation energy of the compound nucleus at high angular momentum. At this stage, it decays via fast fission or gets de-excited via particle-gamma evaporation depending upon the excitation energy. In the beginning, the excitation energy is larger than the particle evaporation threshold, which results in the evaporation of proton, neutron and alpha particles along with the emission of the high-energy γ -rays such as Giant Dipole Resonance (GDR) gammas. Since the protons and the alpha-particles have to tunnel through the Coulomb barrier, the charged particle emission is less probable compared to neutron evaporation. As the compound system move towards the neutron deficient side after the neutron evaporation, the separation energy of neutron increases and the charged particle (proton and alpha) evaporation competes with the neutron emission. Since the evaporated particles carry 5-8 MeV energy per nucleon and only 1-2 \hbar angular momentum, the residual nuclei are produced at very high angular momentum but near the yrast line. In general, the residual nuclei formed through the emission of fewer evaporated particles have higher excitation energy and angular momenta compared to those formed through the higher

particle evaporation channels.

3.2 Decay of Residual Nuclei

The residual nuclei produced from the compound nucleus with high angular momentum, de-excites by γ -decays before reaching to the ground state. It is a challenge for the nuclear spectroscopic study to build up the excited level schemes of the residual nuclei from the information provided by the detection of these discrete γ -rays.

3.3 Interaction of γ -Rays with Matter

The excited states of a residual nucleus can decay in more than one way of which the γ -ray emission is most common. The characteristics of the gamma rays depend on the initial and final state of the residual nucleus.

The detection of these γ -rays is possible as a result of their interaction with the detector material. The three major interactions with the matter are *photoelectric absorption*, *Compton scattering* and *pair production*. These interaction processes lead to the partial or complete deposition of the incident gamma energy.

3.3.1 Photoelectric Interaction

In the photoelectric process, a photon undergoes an interaction with the electron of the absorber atom, which is knocked out from one of the shells of the atom thereby depositing its complete energy. The kinetic energy of the electron is the incident photon energy ($h\nu$) minus the binding energy of the electron in its original shell (E_b). For a typical gamma ray, the photoelectron is most likely to emerge from the K shell, for which its typical binding energy is in range of few keV for materials with a low atomic number

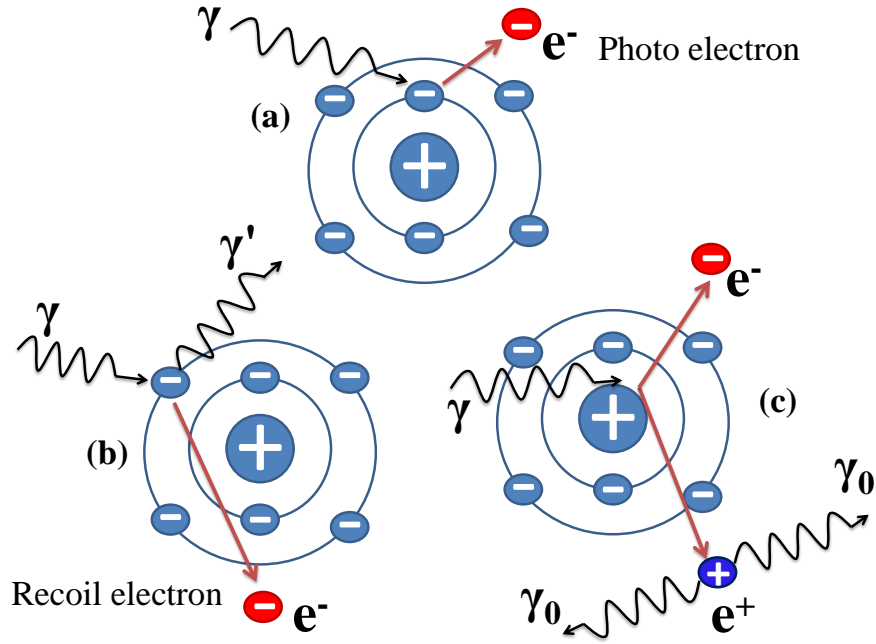


Figure 3.2: The graphical representation of the three interaction processes of γ -ray with the matter: (a) Photoelectric effect, (b) Compton scattering and (c) Pair production.

(Z) to tens of keV for material with high-Z.

$$E_{e^-} = h\nu - E_b, \quad (3.1)$$

Thus, the effect of photoelectric absorption is the generation of a photoelectron, which carries off most of the γ -ray energy, along with one or more low-energy electrons corresponding to the absorption of the original binding energy of the photoelectron. The differential distribution of the electron kinetic energy for a series of photoelectric absorption events can be a simple delta function.

3.3.2 Compton Scattering

The Compton scattering takes place between the incident γ -ray photon and an electron in the absorbing material. In this process incident photon is deflected by an angle θ with respect to its original direction and transfer a portion of its energy to the atomic

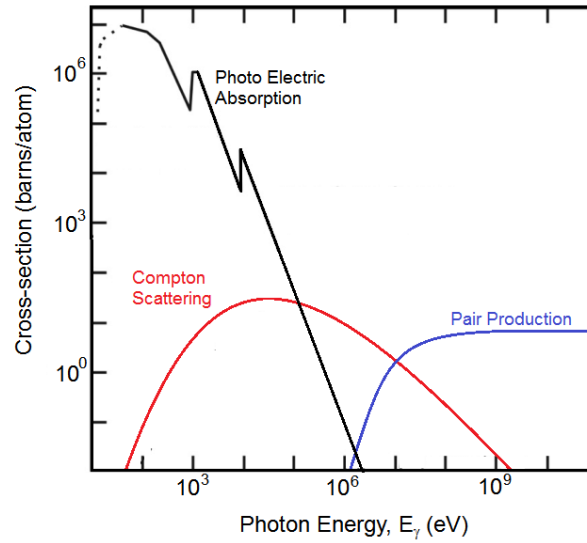


Figure 3.3: The cross-section of three interaction processes of γ -ray with the matter: (a) Photoelectric effect, (b) Compton scattering and (c) Pair production as in ref. [81].

electron. The remaining energy of gamma ray after the scattering can be expressed as,

$$h\nu' = \frac{h\nu}{1 + \frac{h\nu}{m_0c^2}(1 - \cos\theta)}, \quad (3.2)$$

where m_0c^2 is the rest mass energy of the electron. The Compton scattering leads to partial energy deposition which contributes to the undesirable continuous background referred as Compton background.

3.3.3 Pair Productions

If the incident γ -ray energy exceeds twice the rest mass energy (1.02 MeV) of an electron, the pair production is energetically possible in which a γ -ray photon by interacting with detector material creates an electron - positron ($e^- - e^+$) pair. The excess energy above the 1.02 MeV carried in by the gamma, goes into the kinetic energy shared by the electron and the positron. The created $e^- - e^+$ pair will travel a few millimeters before losing all their kinetic energy to the absorbing medium. Because of the very short lifetime, e^+ annihilates with an electron of the medium and generates two gamma photons each with

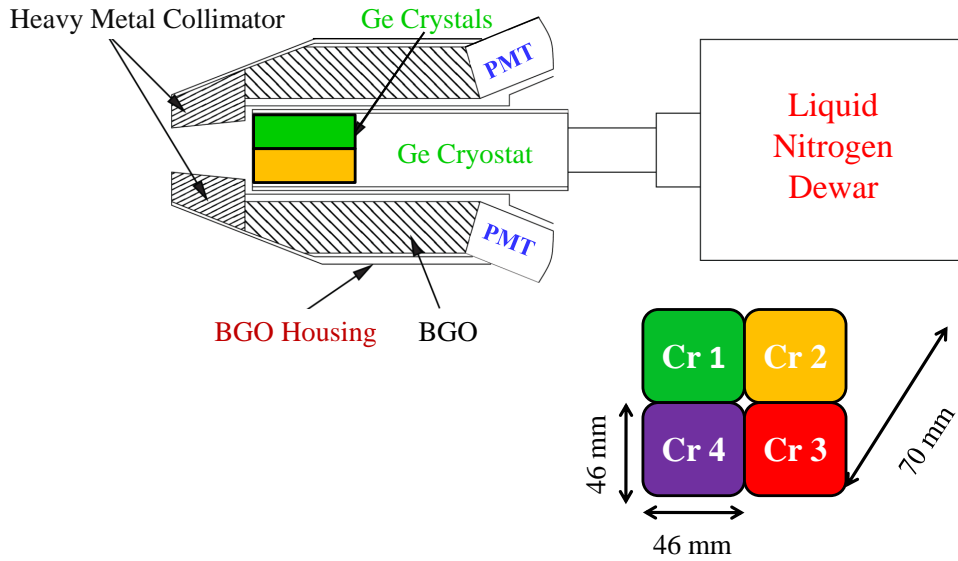


Figure 3.4: The schematic diagram of the clover detector representing the typical geometry and size of the detector.

the energy of 511 keV. These photons can deposit their total energy by interacting further with the detector medium through Compton scattering and photo electric absorption or may escape.

3.4 Detection of γ -rays: Clover Detector

The discrete γ -rays contain all the structural information of the residual nucleus. Thus, the detector used for the detection of these γ -rays should have excellent energy resolution with a substantial detection efficiency along with a good timing response. The semiconductor detectors fulfil this criterion. The size of the detector also plays an important role. A larger detector has higher detection efficiency but the larger solid angle results in a considerable Doppler broadening of the observed γ -rays thereby leading to the deterioration of the energy resolution.

An economical way to circumvent this problem is to mount more than one small Ge crystal (110 cm^3) within the same cryostat surrounded by the common Anti-Compton

Shield (ACS) (Figure 3.4). The clover detector is such a type of composite detector which consists of four separate co-axial n-type High Purity Germanium (HPGe) crystals packed together in a four-leaf clover arrangement. The crystals are 50 mm in diameter and 70 mm in length. The typical dimensions of the clover detector are shown in Figure 3.4. The crystals are tapered in the front face to enable the close packing (Ge-Ge distance of about 0.2 mm). The total active volume of a clover detector is $\sim 470 \text{ cm}^3$ which is 89% of the total volume. Figure 3.4 shows the schematic diagram of a clover detector encased in an Anti-Compton Shield (ACS) and attached to a liquid nitrogen Dewar. The ACS consist of the scintillation detectors which are made of Bismuth Germanate, $\text{Bi}_4\text{Ge}_3\text{O}_{12}$ (BGO) and are used to detect the Compton scattered γ rays which escape from Ge crystals. Each of the four crystals is an individual detector with independent preamplifier output. This permits the option of the addition of time correlated energies deposited in more than one crystal by Compton scattering. This procedure of adding up the time-correlated Compton scattered event is called add back and it significantly enhances the photopeak efficiency, particularly in the high energy regime (~ 1.5 times) because of the higher Compton scattering probability. The small opening angles of the individual crystals ensure that the observed γ transitions are not Doppler broadened. The clover detectors have another important advantage over single crystals. The intrinsic Clover geometry makes it suitable for the use as a Compton polarimeter to measure the linear polarization of γ -rays.

3.4.1 The Indian National Gamma Array

The Indian National Gamma Array (INGA) is a multi-detector array of clover detectors, which is a collaborative effort of Saha Institute of Nuclear Physics (SINP), Tata Institute of Fundamental Research (TIFR), Bhabha Atomic Research Centre (BARC), Variable Energy Cyclotron Centre (VECC), UGC DAE Consortium for Scientific Research, Inter University Accelerator Center (IUAC) and many Universities in India. The detector

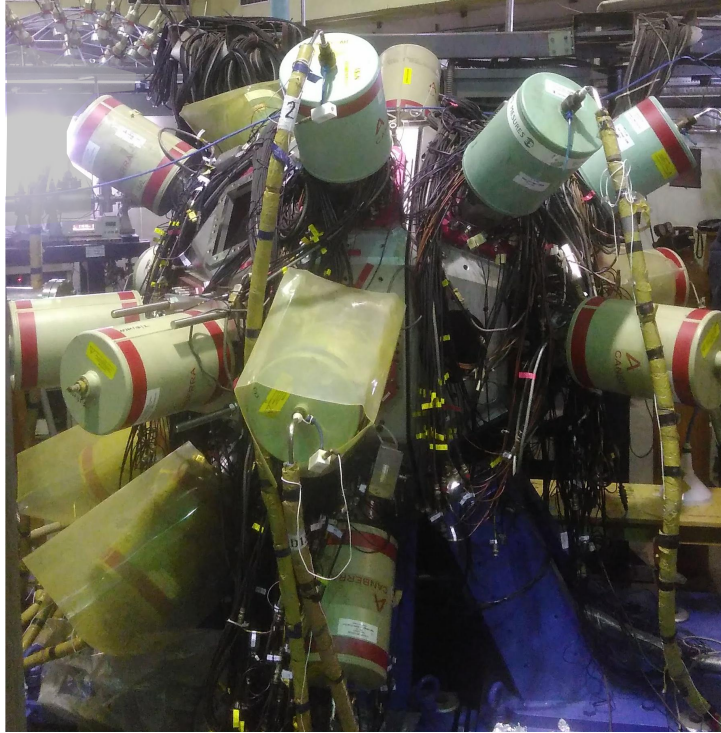


Figure 3.5: Indian National Gamma Array (INGA) set-up at IUAC, New Delhi in the year 2018 with sixteen Compton suppressed clover detectors.

mounting stand at TIFR has provision for 24 number of Compton suppressed clover detectors positioned at six different angles with three detectors each at 23° , 40° , 65° , 115° , 140° , and 157° and six detectors at 90° with respect to the beam axis. The stand at IUAC also supports for 24 clover detectors which are arranged in five different angles with four detectors each at 32° , 57° , 123° , 148° and eight detectors at 90° with respect to the beam direction as in Figure 3.5. The detector number varies at the time of experiment depending on the availability of the clover detectors. At the center of the array the target is placed at a distance ~ 25 cm. The overall photo peak efficiency $\sim 5\%$ can be achieved with this array at $E_\gamma \sim 1$ MeV.

This array requires a fast data acquisition system to provide energy and timing information (time stamped events) of all the 24 clover detectors (96 crystals) and to store the in-beam data as single or multi-fold events. The detectors at various angles are used to measure the angular distribution, polarization asymmetry and lifetime of the excited

nuclear states through Doppler Shift Attenuation Method (DSAM). In the present thesis work, the in-beam data were taken from two experiments performed at TIFR and IUAC with INGA as detection system containing 19 and 16 Compton suppressed clover detectors, respectively.

3.5 Data Analysis Techniques

The data acquired from the fusion-evaporation reactions are analyzed in offline. The digitally converted information are obtained from the preamplifier pulses, which contain the relative timing and the energies of the detected γ transitions decaying from the excited nuclear states. The detectors are calibrated for γ energies and detection efficiencies with the help of the ^{133}Ba and ^{152}Eu radioactive γ sources. The prompt γ rays are chosen by selecting an appropriate coincidence window of ≈ 200 ns in the *Ge* timing spectra and the add-back energies are then sorted into $E_\gamma - E_\gamma$ coincidence matrices and $E_\gamma - E_\gamma - E_\gamma$ cube. More than one detectors firing within the coincidence timing-window produce a point in a $E_\gamma - E_\gamma$ matrix for each combination of the two γ transition energies. This coincidence matrix is then symmetrized so that the coincidence information can be obtained by choosing a slice around certain transition energy along one axis and analyze the projection of this slice onto the other axis. In addition, specific angle dependent asymmetric matrices are also built from the coincidence data.

3.5.1 Energy Calibration and Gain matching

In order to generate the add-back spectrum for each of the clover detectors in the array and to determine the energies of γ -rays observed in the de-excitation of the nuclei, the detectors must be accurately calibrated with the standard γ -ray sources. The energy calibration has been performed using the known γ -ray energies from the radioactive source ^{152}Eu . The energies are plotted against channel number and fitted using the

Table 3.1: The measured calibration coefficients a_0, a_1, a_2, a_3, a_4 using ^{152}Eu radio active source.

a_0	a_1	a_2	a_3	a_4
-5.51	$+2.66 \times 10^{-01}$	$+4.84 \times 10^{-07}$	-2.59×10^{-11}	$+1.14 \times 10^{-01}$
-3.70	$+2.83 \times 10^{-01}$	-2.94×10^{-07}	$+2.16 \times 10^{-11}$	$+1.52 \times 10^{-01}$
-3.97	$+2.77 \times 10^{-01}$	-1.96×10^{-07}	$+1.38 \times 10^{-11}$	-1.21×10^{-01}
-6.66	$+2.79 \times 10^{-01}$	-3.54×10^{-07}	$+2.27 \times 10^{-11}$	-2.32×10^{-01}
-3.04	$+2.91 \times 10^{-01}$	-7.20×10^{-07}	$+5.87 \times 10^{-11}$	-2.37×10^{-01}
-3.85	$+2.61 \times 10^{-01}$	-7.24×10^{-07}	$+3.67 \times 10^{-11}$	-1.05×10^{-01}

polynomial,

$$E_\gamma = a_0 + a_1x + a_2x^2 + a_3x^3 + a_4\sqrt{x}. \quad (3.3)$$

Here, x is the ADC channel number and the calibration coefficients a_0, a_1, a_2, a_3, a_4 are determined for each crystal. The values of these coefficients for a typical calibration are shown in Table 3.1.

The calibration is the prerequisite for the gain matching process. The different crystals have different gain factors at a given high voltage. So the voltage pulses for a particular γ -ray energy have the different ADC channel number after digitization. The gain matching is a procedure to generate the same ADC channel number for all the crystals for a particular γ -ray energy. The gain matching is achieved as follows. Using Eqn. 3.3 each crystal of the clover is energy calibrated in terms of ADC channel number by knowing calibration coefficients, which were different for individual ADC's as shown in Table 3.1. This energy value is then divided with the chosen scaling factor, which remains the same for all ADC's. (Typical values of the scaling factor used are 0.5 keV/channel or 1 keV/channel.) This represents a new ADC channel number, which is gain matched. Mathematically it is expressed as,

$$C_{gm} \text{ (Randomized Gain matched channel number)} = E_\gamma \text{ (keV)} / \text{Scaling factor} \\ \text{(keV/channel)} + \text{Random No.},$$

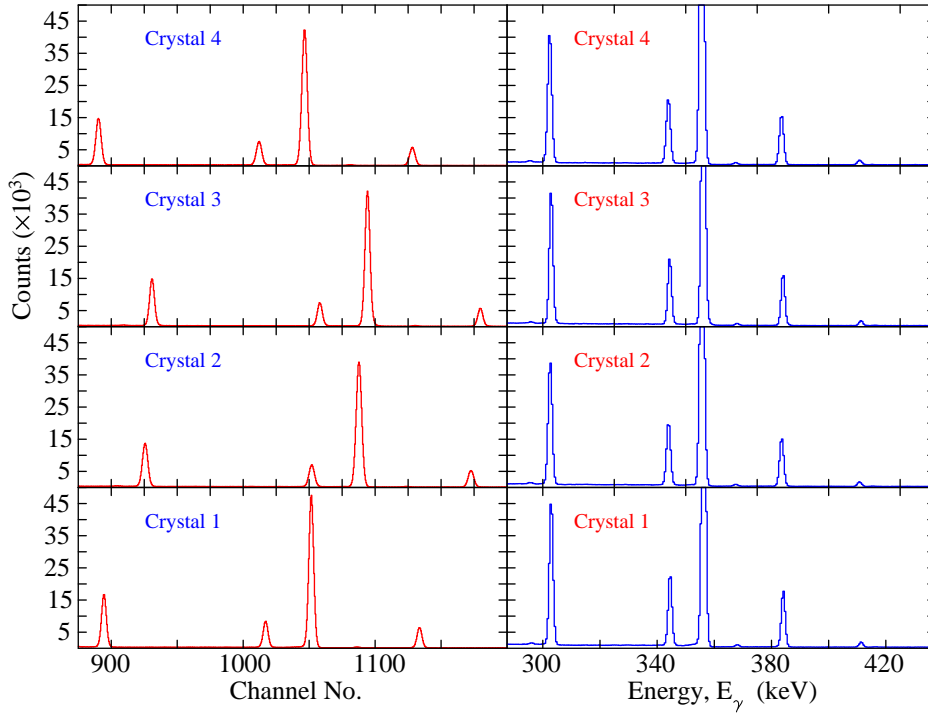


Figure 3.6: The consequence of the energy calibration and the gain matching on the spectra of each of the four crystals of a clover detector. The four panels on the left side depict the 303, 356 and 384 keV γ transitions of ^{133}Ba and 344 keV γ transition of the ^{152}Eu radioactive source in the uncalibrated spectra of the four crystal. The right panels show the energy calibrated and gain matched (1 keV/channel) spectra of the same.

where extra random number is added to retain the smoothness of the resulting ADC (gain matched) spectrum and C_{gm} is the gain matched channel number.

The typical projected spectra before and after the gain matching are shown in Figure 3.6, which was obtained during the course of present work.

3.5.2 Efficiency Calibration and Add-back factor

To determine the relative intensity of the de-excited γ -rays it is necessary to know the relative efficiency of the INGA set up. The relative detection efficiency is obtained with the radioactive sources ^{133}Ba and ^{152}Eu placed at the target position. The experimental data points are fitted by a theoretical function, using the RADWARE [82, 83] package which expressed as,

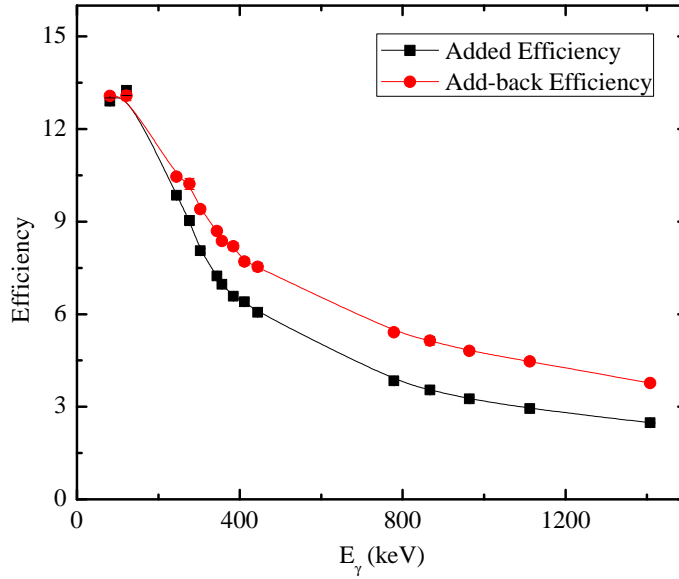


Figure 3.7: The relative photopeak detection efficiency of the γ -ray transitions of the ^{152}Eu radioactive source obtained from a clover detector in the INGA array at TIFR as a function of γ -ray energy.

$$\ln(\epsilon) = [(A + Bx + Cx^2)^{-G} + (D + Ey + Fy^2)^{-G}]^{1/G}, \quad (3.4)$$

where ϵ is efficiency, $x = \ln(E_\gamma/100)$ and $y = \ln(E_\gamma/1000)$, the parameters A , B and C determine the lower energy part of the efficiency curve whereas D , E and F determine the high energy part of the efficiency curve. The parameter G determines shape in the turn over the low energy region of the efficiency curve. The efficiency curve for the sum of four crystals in a typical clover detector in the INGA array is shown in Figure 3.7.

The add-back factor is defined as the ratio of detection efficiency of a clover detector to the time-uncorrelated sum of detection efficiency of the four separate single crystals of that clover detector. At lower energies (~ 150 keV) the add-back factor is ~ 1 , but at higher energies (~ 1 MeV), the add-back factor of a clover detector is ~ 1.5 (Figure 3.8). Thus, due to the Compton compensation at higher energies, the clover efficiency is almost six times larger than the relative efficiency of a single 110 cm^3 crystal.

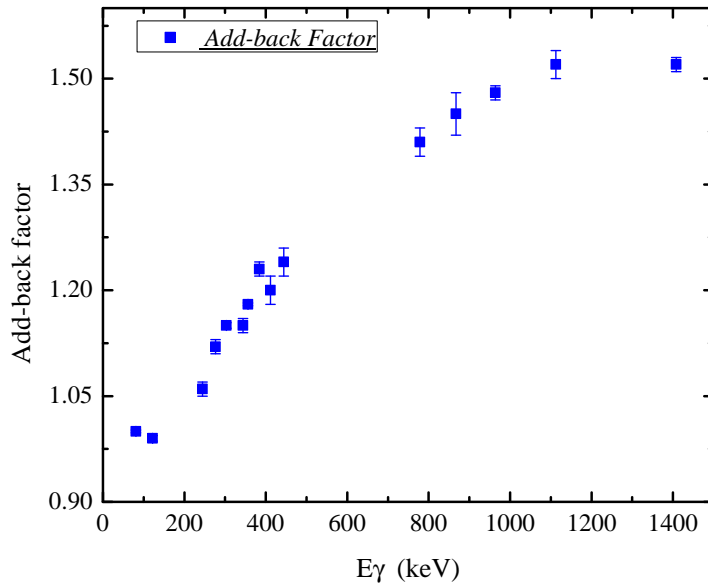


Figure 3.8: The variation of the add-back factor with γ -ray energy for a Compton suppressed clover detector used in INGA at TIFR.

3.5.3 Coincidence Measurements and Analysis

The add-back ADC channel numbers of the two or three coincident clover detectors are stored in a matrix or in a cube. In the case of the matrix, only a single gate can be set on one of the energy axis and the resulting spectrum is projected on the other axis. In case of the cube, the projected spectrum can be obtained by setting two gamma-gates along the two energy axis. These analysis have been carried out using the RADWARE and the INGASORT software packages [82–84].

The level scheme of a nucleus is a way of pictorially representing the excited energy levels in increasing order from which several structural patterns can be identified. The coincidence relation is the first and the crucial step in the direction of level scheme construction. When gated by a particular γ -ray, only those γ -rays that are in coincidence to the gating γ -ray transition are present in the projected spectrum. Consequently the γ -rays belonging to two different bands in the same nucleus will not be in coincidence with each other (E_{γ_3} and E_{γ_8} are in coincidence but E_{γ_2} and E_{γ_6} are not in coincidence as shown Figure 3.9). Thus a large set of gated spectra are generated and the coincidence

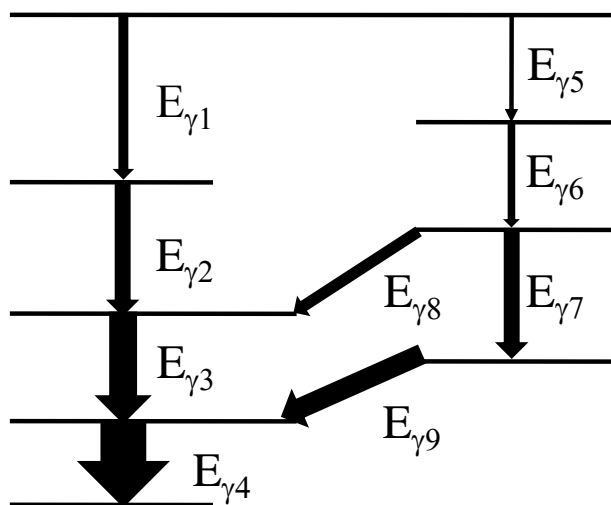


Figure 3.9: A representative partial level-scheme showing coincidence relation and relative intensity balance (I_γ).

information from all are used in a self consistent way to generate the level scheme. The spin and parity of the excited level can be assigned by measuring the multipolarity and the electric/magnetic nature of the deexciting γ -ray provided the lower level spin and parity is known.

3.5.4 Angular Distributions Measurements

In order to determine the spins of the excited states of the nuclei populated in the fusion evaporation reactions, one can measure the angular distribution of the depopulating γ transitions. In the fusion evaporation reaction, the angular momenta of the residual nuclei are aligned perpendicular to the reaction plane (i. e., $m = 0$). This preferential alignment fixes the quantization axis and thereby the anisotropy of the γ -transitions can be measured. Two different techniques are discussed in the following sections.

In the first case, by the fusion-evaporation reaction the compound nucleus is formed in a state with its angular momentum vector perpendicular to the axis defined by the direction of the beam ($\mathbf{l} = \mathbf{r} \times \mathbf{p}$). The orientation of the nucleus is slightly attenuated ($m \sim 0$) by the emission of the evaporated particles (neutrons, protons, and alpha-

particles) and γ -rays. When a nucleus in such a state emits γ -radiation, the relative intensities at different angles with respect to the beam-axis depend on the multipolarity of the transition ‘ l ’ and can be expressed using Legendre polynomials as,

$$W(\theta) = \sum_{l=0}^l A_{2l} P_{2l}(\cos\theta) = A_0 + A_2 P_2(\cos\theta) + A_4 P_4(\cos\theta) + \dots + A_{2l} P_{2l}(\cos\theta), \quad (3.5)$$

where $W(\theta)$ is the γ -ray intensity measured at an angle θ to the beam direction, A_{2l} 's are angular distribution coefficients and P_{2l} 's are the Legendre polynomials. The A_{2l} 's depend on the m -state population of the nuclei and the initial and final angular momentum states. Generally, in the fusion evaporation reactions, multipolarities of the γ transitions can be restricted to angular momentum values of $2\hbar$ or less (i.e. usually only the $E2$ ($l = 2$, quadrupole), $M1$ or $E1$ ($l = 1$, dipole) decays were observed). Thus the angular distribution of γ transitions can be expressed as,

$$W(\theta) = A_0 + A_2 P_2(\cos\theta) + A_4 P_4(\cos\theta) = A_0 [1 + a_2 P_2(\cos\theta) + a_4 P_4(\cos\theta)]. \quad (3.6)$$

By measuring the intensity of the γ -ray at the different angles about the incident beam direction and by fitting the intensity distributions by the Eqn. 3.6, the values of the coefficients a_2 and a_4 can be obtained. These coefficients give an idea about the multipolarity of the γ transitions. In case of mixed multipolarity transitions ($M1/E2$), the mixing ratio can also extracted from the measured angular distribution coefficients.

3.5.4.1 Mixing Ratio Calculation

The angular distribution coefficients a_2 and a_4 for a particular γ transition can also be calculated theoretically, considering the partial degree of alignment as described by

Yamazaki [85] and by Mateosian and Sunyar [86]. The mixing ratio (δ) has been calculated by comparing the measured and calculated a_2 and a_4 coefficients. The angular distribution for the partial alignment of the m -state is defined as

$$a_k = \alpha_k A_k^{max}, \quad (3.7)$$

where, α_k is attenuation coefficients which depend on the m -state population of angular momentum state J , tabulated in [86] and A_k^{max} is the angular distribution coefficients for fully align states, defined as

$$A_k^{max} = \frac{f_k(J_i L_1 L_1 J_f) + 2\delta f_k(J_i L_1 L_2 J_f) + \delta^2 f_k(J_i L_2 L_2 J_f)}{1 + \delta^2} \quad (3.8)$$

where, L_1 and L_2 are the possible multipolarities of the γ transition between angular momentum states J_i and J_f , the ' f ' coefficients found from the tabulated values [85] and δ is the mixing ratio of the γ ray. The standard deviation (χ^2) between the calculated and measured angular distribution coefficients a_2 and a_4 can be expressed as [87],

$$\chi^2 = \frac{(a_2^{exp} - a_2^{cal})^2}{3(\Delta a_2^{exp})^2} + \frac{(a_4^{exp} - a_4^{cal})^2}{3(\Delta a_4^{exp})^2}, \quad (3.9)$$

here, a_2^{exp} , a_4^{exp} values are experimentally measured coefficients with uncertainties Δa_2^{exp} and Δa_4^{exp} , respectively, which are obtained by fitting the angular yield of a γ transition with the Eqn. 3.6. The a_2^{cal} and a_4^{cal} are the angular distribution coefficients of the same transition calculated with the help of Eqns. 3.7 and 3.8. These calculated coefficients are varied by varying the mixing ratio (δ) (Eqn. 3.8) and the corresponding χ^2 values are calculated. If, for a particular value of δ , the standard deviation (χ^2) reaches its minimum (i. e., $\chi_{min}^2 < 0.1\%$ of the maximum deviation, χ_{max}^2), then that δ value is the measure of the mixing ratio for that transition. The uncertainty in mixing ratio is calculated by finding the range of δ for which $\chi_{min}^2 + 1$ value is reached, which

is the universal procedure for χ^2 test.

3.5.5 DCO Analysis

The quantization axis can also be fixed by detecting one of the coincident γ -rays in a particular direction. In this case the other γ -ray will exhibit the angular anisotropy. It is clear from the preceding discussion that the angular correlation may be considered as a special case of angular distribution, in the sense that a particular orientation is chosen by the observation of one transition in a fixed direction.

The angular correlation of the coincident γ transitions depends on the multiplicities of both the transitions. The multiplicity of a γ transition can be conjectured from the measurements of the Directional Correlations Orientation (DCO) ratio [8, 88] provided that multiplicity of one transitions is known. The DCO ratio is expressed as,

$$R_{DCO} = \frac{I_{\gamma_1}(\text{measured at } \theta_1; \text{gated by } \gamma_2 \text{ at } \theta_2)}{I_{\gamma_1}(\text{measured at } \theta_2; \text{gated by } \gamma_2 \text{ at } \theta_1)}, \quad (3.10)$$

where I_{γ_1} is the intensity of γ_1 observed at an angle θ_1 (θ_2) in coincidence with γ_2 at θ_2 (θ_1), whose multiplicity is known. The maximum response of the R_{DCO} can be achieved by choosing $\theta_1 \sim 0^\circ$ and $\theta_2 \sim 90^\circ$ with respect to the beam direction. For the stretched transitions, the value of the R_{DCO} is close to unity when the gated and the observed transitions have the same multiplicity and for different multiplicities the value is ~ 0.5 or 2.0 depending upon the definition. These values are calculated numerically using the ANGCOR code [89]. For the experiment performed at TIFR, $\theta_1 = 140^\circ$ and $\theta_2 = 90^\circ$ were chosen.

For the determination of DCO ratio, one angle-dependent two-dimensional E_γ - E_γ matrix is built from the 2-fold coincident data, where the gamma energies detected at 140° detector and 90° detector are stored along the two axes, respectively.

3.5.5.1 Width of the Substate Population (σ/j)

The sub-state population (σ/j) width of a reaction is an important parameter to determine the electromagnetic character of the γ transitions. In order to estimate the values of σ/j , pure dipole (mostly $E1$ as $M2$ mixing probability is too small) transitions are selected. The DCO ratios (R_{DCO}) are extracted by gating on the stretched $E2$ transitions for the selected electric dipole $E1$ transitions. Theoretically, R_{DCO} values are calculated (using ANGCOR) for the chosen transitions, by varying σ/j ratio. The value for σ/j is estimated from the best fit to the experimental R_{DCO} values. The average of the σ/j for the selected $E1$ transitions is the measure of the width of the substate population in a given reaction which has been adopted for the mixing ratio (δ) calculation of the γ transitions.

3.5.6 ADO Analysis

The value of R_{DCO} for some of the transitions can not be evaluated because of its weak nature in a single gamma gate. So for spin assignment of these weak transitions, Angular Distribution from Oriented Nuclei (ADO) ratio [8, 90] can be used. The ADO ratio of a γ transition is defined as,

$$R(\theta) = \frac{I_{\gamma}(\text{measured at } \theta_1; \text{ gated by all})}{I_{\gamma}(\text{measured at } \theta_2; \text{ gated by all})}, \quad (3.11)$$

where I_{γ} was the intensity of the observed γ transitions at an angle θ_1 (θ_2) by gating all other angles. The sensitivity of the ADO ratio is maximum when $\theta_1 \sim 0^\circ$ and $\theta_2 = 90^\circ$ with respect to the beam axis.

For the experiment performed at TIFR, the detectors are used at $\theta_1 = 140^\circ$ and $\theta_2 = 90^\circ$. As far as the present geometry is concerned, the value of $R(\theta)$ for pure dipole (pure quadrupole) transitions is expected to be ≈ 0.6 (1.6) and the transitions which deviate

from this values have mixed type of multipolarity.

For the estimation of the ADO ratio, two angle-dependent E_γ - E_γ matrices are constructed from the 2-fold coincident data. In one matrix, the events which are detected by the 140° detector and all other coincidence events are placed along the two axes, respectively. Likewise, another matrix is formed by replacing the events from the 140° detector events by 90° detector events.

3.5.7 Linear Polarization Measurements

A γ -ray of multipolarity L between two states J_i and J_f of parity Π_i and Π_f , respectively, is

$$\begin{aligned} &\text{Electric type, when, } \Pi_i\Pi_f = (-1)^L; \text{ and} \\ &\text{Magnetic type, when, } \Pi_i\Pi_f = (-1)^{L+1}. \end{aligned} \tag{3.12}$$

As a result, one can ascertain the relative parity between two states by measuring the electric or magnetic character of the γ -ray. The method used to assign the γ type (electric/magnetic) is known as ‘Polarization by Directional Correlation of Oriented states’ or *PDCO*.

The electric or magnetic nature of the γ -ray is directly related to the direction of the γ -ray after Compton scattering inside the detector. For the electric character of the γ photon, the reaction plane (defined by the outgoing γ -ray and the beam axis) is perpendicular to the Compton scattering plane (defined by the plane of direction of the Compton scattered photon). In case of magnetic nature, the reaction plane is parallel with the Compton scattering plane. The segmented Clover detector has the required geometry for measuring this asymmetry of Compton scattered events in the parallel and perpendicular direction as shown in Figure 3.10. The normalized difference in the number

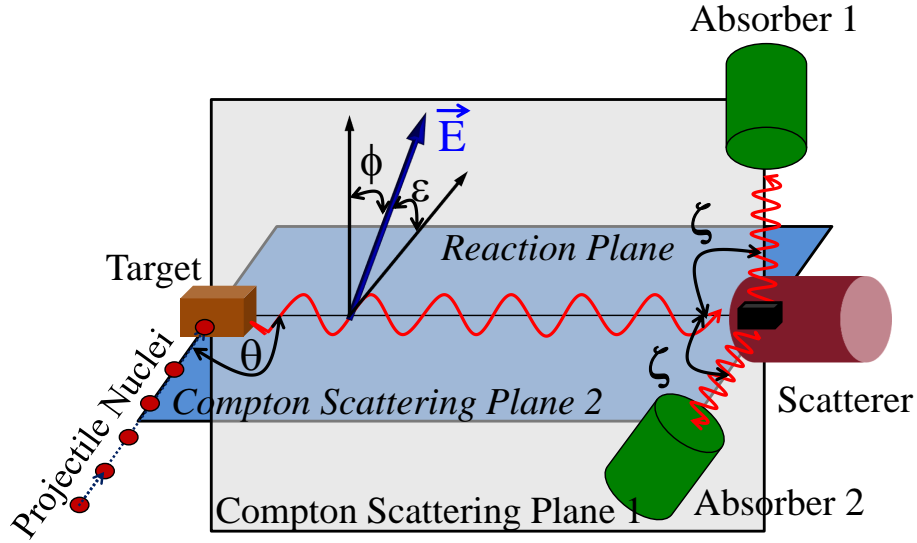


Figure 3.10: The schematic arrangements of the conventional Compton polarimeter for the linear polarization measurement, consisting of one scatterer and two absorber, three planes and four relevant angles. The \vec{E} stands for the electric vector.

of perpendicularly and parallelly Compton scattered photons is termed as *PDCO* and it is defined as [8,91,92],

$$\Delta = \frac{a(E_\gamma)N_\perp - N_\parallel}{a(E_\gamma)N_\perp + N_\parallel}; \quad (3.13)$$

where N_\perp and N_\parallel are the number of perpendicular and parallel Compton scattered γ 's, respectively and $a(E_\gamma)$ is the asymmetry correction factor to take into account the different detection efficiencies of the four segments of the clover. This factor can be determined from [8,91,92]

$$a(E_\gamma) = \frac{N_\parallel}{N_\perp}, \quad (3.14)$$

using unpolarized radioactive γ -ray source ^{152}Eu and ^{133}Ba . The electric and magnetic character of the γ -rays correspond to the negative and positive values of the PDCO, respectively.

But, as the γ energy increases, the Compton scattering probability decreases. Thus the *PDCO* is corrected for the polarization sensitivity and the polarization P can be written as [8, 91, 92]

$$P = \frac{\Delta}{Q(E_\gamma)}, \quad (3.15)$$

where Q is the polarization sensitivity defined as,

$$Q = Q_0(p_1 E_\gamma + p_2) \quad (3.16)$$

with

$$Q_0 = \frac{1}{\frac{E_\gamma}{0.511} + \frac{0.511}{E_\gamma + 0.511}}, \quad (3.17)$$

where Q_0 represents the sensitivity for a point-like absorber and E_γ is in units of MeV. The extended solid angle of an absorber (segmented clover) is taken into account by two parameters p_1 and p_2 . These parameters and sensitivity, Q , are experimentally extracted using γ lines with known polarization values. For the experiment performed at TIFR, $p_1 = 0.74(0.10)$ and $p_2 = 3.5(1.1) \times 10^{-4}$ in keV^{-1} . Thus, by knowing the sensitivity, Q as a function of the incident γ photon energy, the linear polarization can be measured using the measured *PDCO* values.

3.5.8 Level Lifetime Measurements

In the fusion evaporation reaction, a population of nuclei (N_0) produced at an excited level at the time $t = 0$ will decay according to the law: $N(t) = N_0 e^{-t/\tau}$, where τ is the excited level lifetime. The level lifetime is a direct measure of the electromagnetic transition probability which is linked to the initial (ϕ_i) and final state (ϕ_f) wave-functions

and the electromagnetic transition operators, which are well known. Thus by comparing the measured and calculated level lifetimes from a model, the validity of the model wavefunctions can be determined. In this way it is possible to set an insight to the nuclear single particle level structures.

If the nuclear level lifetime $\tau > ns$, the lifetime can be measured by the direct timing method with the help of a Germanium detector by using the delayed coincidence technique. For the shorter lifetime measurements, an indirect method has to be used. In the Recoil Distance Method (RDM), lifetime within the range picoseconds to nanoseconds can be measured [93].

If the slowing down time in the target/backing ($\sim 10^{-12}$ sec) medium is comparable with a level lifetime of the states, i. e., for sub-picosecond lifetimes the RDM technique is not suitable as the target-to-stopper recoil distance becomes too small. However, if the history of the slowing down process of the recoil nuclei inside the target-backing medium can be estimated, one may use the Doppler broadened lineshape to determine the nuclear lifetime. This method is known as the Doppler Shift Attenuation Method [93, 94].

If a γ -ray of transition energy E_O emitted at an angle θ from a recoil nuclei with recoil velocity β , the Doppler shifted energy E_S [93] (Figure 3.11) is given by,

$$E_S \approx E_O \left(1 + \frac{\beta}{c} \cos\theta \right). \quad (3.18)$$

As the recoil velocity decreases continuously (β to zero) in the target-backing medium, the γ -ray energy spectrum will show a continuous lineshape (Figure 3.11).

The slowing down process of the recoil nuclei as a function of time is usually taken from the Northcliffe and Schilling or Ziegler [95]. The stopping process of the recoil nuclei consists of two different processes, electronic and nuclear stopping. This is usually accounted by using either the Blaugrund formalism or using Monte Carlo simulations of the recoil velocity profiles [94]. In this thesis work, the slowing down process of

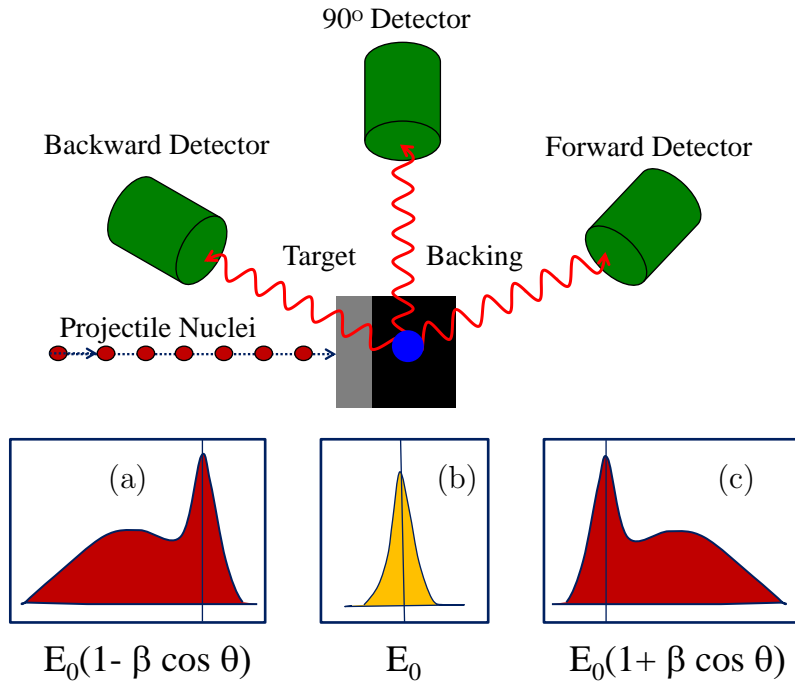


Figure 3.11: The schematic representation of the experimental lineshapes of a γ transition depopulating from a state having lifetime $\sim ps$. In (a) the shape at the backward angle ($-\theta$) detector, (b) the unshifted peak of energy E_0 at the 90° detector and (c) the shape at the forward angle ($+\theta$) detector, have been shown.

recoil nuclei inside the target-backing medium has been simulated using the Monte Carlo technique incorporated in the LINESHAPE program [96,97]. The program LINESHAPE is a combination of the program DSAMFT, which has been combined with the least-squares minimization routine MINUIT [98]. Through the Monte Carlo simulation, it is possible to track both the scattering directions and velocities of the recoiling nuclei. The slowing down time of the recoiling nuclei in the target and backing material (Pb) was divided into 2000 time steps which provide a complete set of lineshape ranging from fully shifted to stop peak. DSAMFT calculates lineshape using the Monte Carlo simulated velocity profiles assuming lifetime values of the observed transitions and also of unobserved side-feeding transitions. The side-feeding has been modeled with a cascade of five transitions and having a moment of inertia which is the same as that of the band under consideration, feeding into each state. A direct feeding (100% side-feeding) has been assumed for the topmost transition and the lineshape of this transition has been fitted to obtain an effective lifetime of this state. This effective lifetime is used

as the top-feeding lifetime for obtaining the level lifetime of the next lower state in the cascade. Throughout the fitting process quadrupole moment of the side-feeding cascades, quadrupole moment of the in-band transitions, contaminant peak parameter and background parameter is kept fixed. For each set of parameters, the simulated lineshape is calculated and a global minimization has been carried out for each angle using χ^2 minimization routines MINUIT [98], simultaneously, where only the quadrupole moment of the side-feeding cascades and the in-band transitions of each state have been kept as a free parameter. After getting a global minimum of χ^2 , the uncertainties in the lifetimes are determined from the nature of χ^2 in the vicinity of its minimum value (χ_{min}^2), over the region where $\chi^2 \leq \chi_{min}^2 + 1$. This corresponds to the “one-standard-deviation” in terms of least-squares fitting method. The uncertainty in a given parameter could be determined by varying that parameter in a step higher and lower of its best value and in every step, this parameter is set fixed and χ^2 have been re-minimized by setting all the other parameters free.

To determine the level lifetime from the experimental data, E_γ - E_γ asymmetric matrices have been used to construct the background-subtracted gated spectra at different angles. The asymmetric matrices contain events recorded by the other detectors at a specific angle (forward, backward and 90°) along one axis and the coincidence events of all the detectors on the other axis. The gates have been set on the transitions below the levels of interest. The spectra at 65° , 90° and 140° have been fitted simultaneously to extract the level lifetimes. The spectra at 90° are specifically used for identifying the contaminant peak in the fitting region.

These experimental techniques have been used to investigate the high spin behavior of the ^{141}Sm , ^{142}Eu and ^{140}Eu , which have been discussed in the following three chapters.

CHAPTER 4

Structural Evolution in ^{141}Sm

4.1 Introduction

The ^{141}Sm ($Z = 62$, $N = 79$) is a weakly deformed nuclei with the semi magic ^{146}Gd ($Z = 64$, $N = 82$) as the core. Thus, the proton particles can be easily excited to $h_{11/2}$ orbital across the semi-major shell gap and this forms the favorable particle-hole configuration for observing shears mechanism (MR or AMR). In addition with that, as ^{141}Sm is slightly away from the shell closure, the collective excitation of the core may interplay with the shears mechanism in this nuclei. For the study of such competition between collective rotation with the shears mechanism and its possible evolution in shape from planar to aplanar, ^{141}Sm is a suitable candidate.

The high spin states of the ^{141}Sm first studied by Cardona *et al.* [99] using the $^{116}\text{Cd}(^{29}\text{Si}, 4n)$ reaction. They had reported a dipole band with band-head $25/2$ at an excitation energy of 3.3 MeV without any parity assignment. Later ^{141}Sm studied by Latch *et al.* [100] using the reaction $^{142}\text{Nd}(\alpha, 5n)$ and the spin-parities of the dipole band was assigned up to $I^\pi = 33/2^-$ levels.

4.2 Experimental Details and Data Analysis

In the present work, the level structure, ^{141}Sm has been re-investigated by populating it using the fusion evaporation reaction $^{116}\text{Cd}(^{31}\text{P}, p5n)$ at the beam energy of 148 MeV obtained from the Pelletron-LINAC facility at TIFR, Mumbai. The deexciting γ -rays were detected by the INGA set-up. At the time of experiment, 19 Compton suppressed clover detectors were present in the array. The multipolarities and the electromagnetic characters of the observed γ transitions for assigning the spin-parity of the levels were determined from the measurements of the DCO ratio [101, 102], ADO ratio [90], and the linear polarization [103]. The experimental details and the data analysis procedures have been described in the Chapter 3.

In the present experiment, the detectors positioned at 140° and 90° with respect to the beam direction were used for the DCO ratio evaluation. These values were compared with the theoretical values for the multipolarity assignment of the γ transitions. The theoretical DCO ratios were calculated using the code ANGCOR [89]. The estimated DCO ratios for stretched quadrupole (dipole) transitions gated by a pure dipole (quadrupole) transition are $\sim 2.0(0.5)$. For a mixed type of transitions, the values depend on the mixing ratio (δ).

4.3 Experimental Result

The $^{116}\text{Cd}(^{31}\text{P}, xpyn)$ reaction produced several strongly populated channels viz. ^{142}Sm , $^{142,143}\text{Eu}$ nuclei and the ^{141}Sm was observed with a reasonably good cross-section (10% of the total reaction cross-section) (Figure 4.1 (a)). In the coincidence measurements, the gate list created by the transitions of energy 634.8, 1089.0 and 1418 keV shows all the previously observed transitions along with the other transitions of the dipole band of interest (Figure 4.1 (b)) [99, 100].

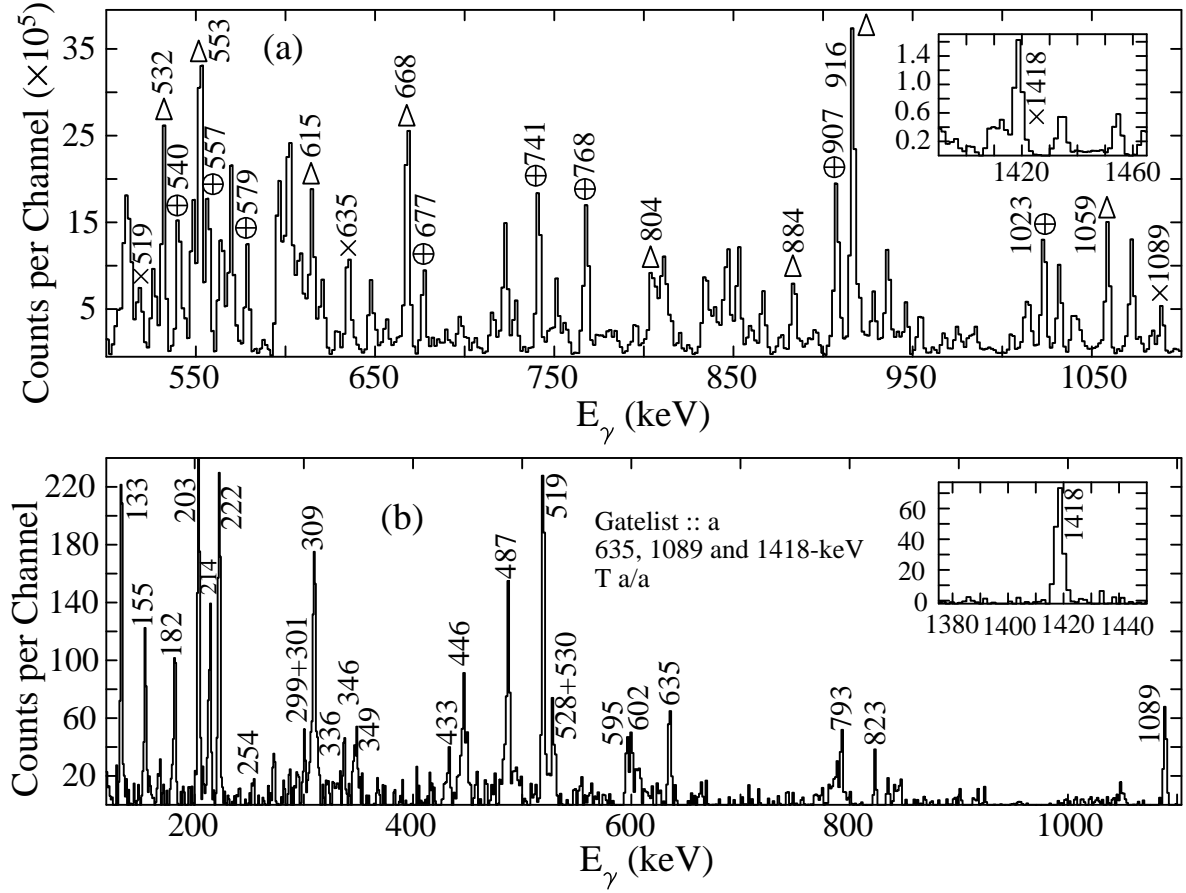


Figure 4.1: (a) The total projection spectrum of the E_γ - E_γ - E_γ cube populated in the present reaction. The γ energy transitions in ^{143}Eu , ^{142}Sm , and ^{141}Sm are marked with the symbols “ Δ ”, “ \oplus ”, and “ \times ”. (b) The added double gated spectrum of 643.8, 1089.0, and 1418.0 keV showing the transitions of the ^{141}Sm .

In the current analysis, all the transitions reported by the Cardona *et al.* were confirmed [99]. The partial level scheme above the excitation energy of 3377 keV is shown in Figure 4.2 as derived from the coincidence relationships, relative intensities, DCO ratio, ADO ratio, and linear polarization measurements. The intensities of the γ -rays above the 3377 keV state ($25/2^-$) excited state were calculated from the symmetric $E_\gamma(90^\circ)$ - $E_\gamma(90^\circ)$ matrix. The relative intensities have been determined by normalizing to the intensity of 132.6 keV ($27/2^- \rightarrow 25/2^-$) transition. The measured spectroscopic parameters, such as transitions energy (E_γ), relative Intensity (I_γ), spin of the involved states (J^π), DCO ratio (R_{DCO}), ADO ratio (R_θ), linear polarization (P) and mixing ratio (δ) have been tabulated in the Table 4.1.

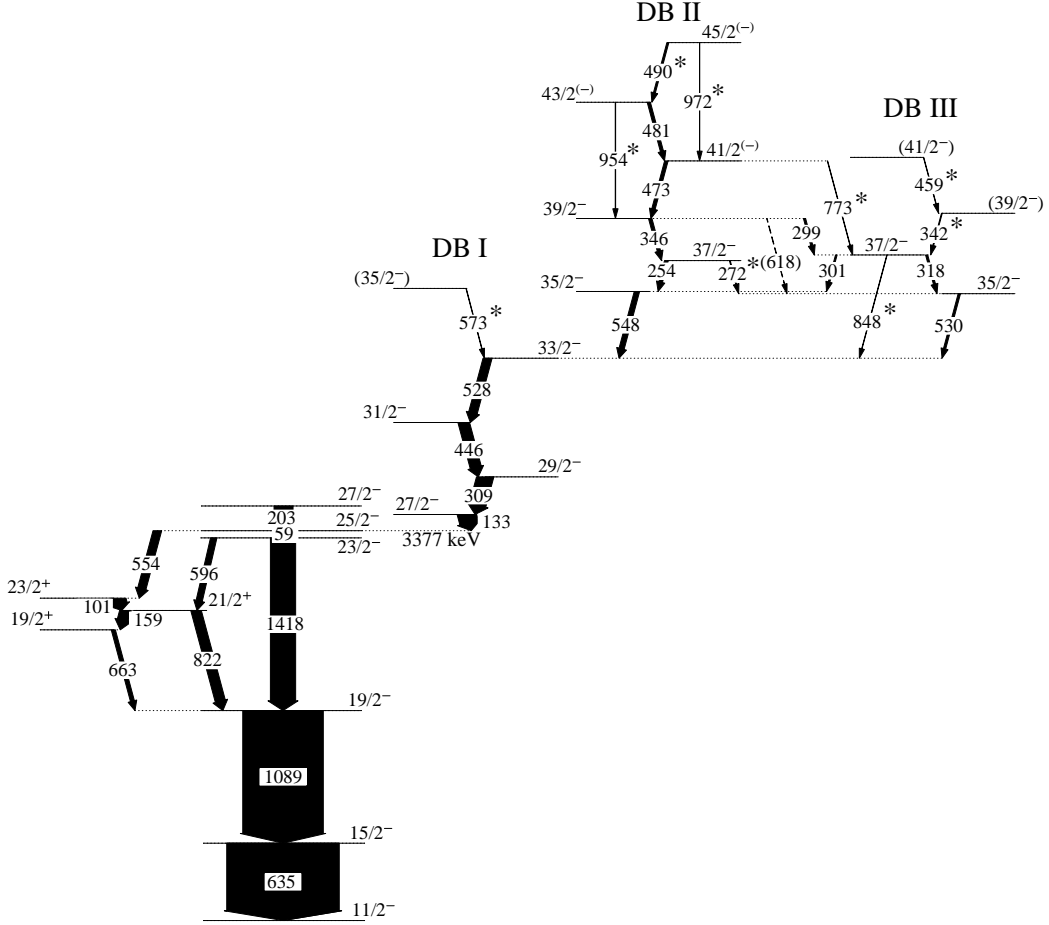


Figure 4.2: The partial level scheme of ^{141}Sm derived from the present work. The γ -ray energies are rounded off to the nearest keV. The widths of the arrows are proportional to the intensities of the transitions. The asterisk marked γ transitions are newly observed. The dipole bands above the 3377 keV level is the key interest in this nuclei.

The spin-parity assignment of the dipole structure can be done only when the multipolarity of the low energy 132.6 keV transition is properly established. In the earlier reported level scheme of ^{141}Sm , this transition was proposed as purely magnetic dipole transition ($M1$) without any polarization measurement and the deexciting state of 132.6 keV transition was assigned as $27/2$ without any parity [100]. However, negative parity was proposed for the dipole structure. The DCO ratio value for the 132.6 keV transition was found to be 1.31(11), indicating a mixed character which is in contrast with the previous measurement [99, 100]. The measured DCO ratio value of the 132.6 keV can be theoretically reproduced by assuming it to be a dipole transition ($L = 1$) with quadrupole ($L = 2$) admixture ($M1 + E2$ or $E1 + M2$) or a quadrupole ($L = 2$) one with octupole ($L = 3$) admixture as in Figure 4.3 (a). The single particle estimation tells

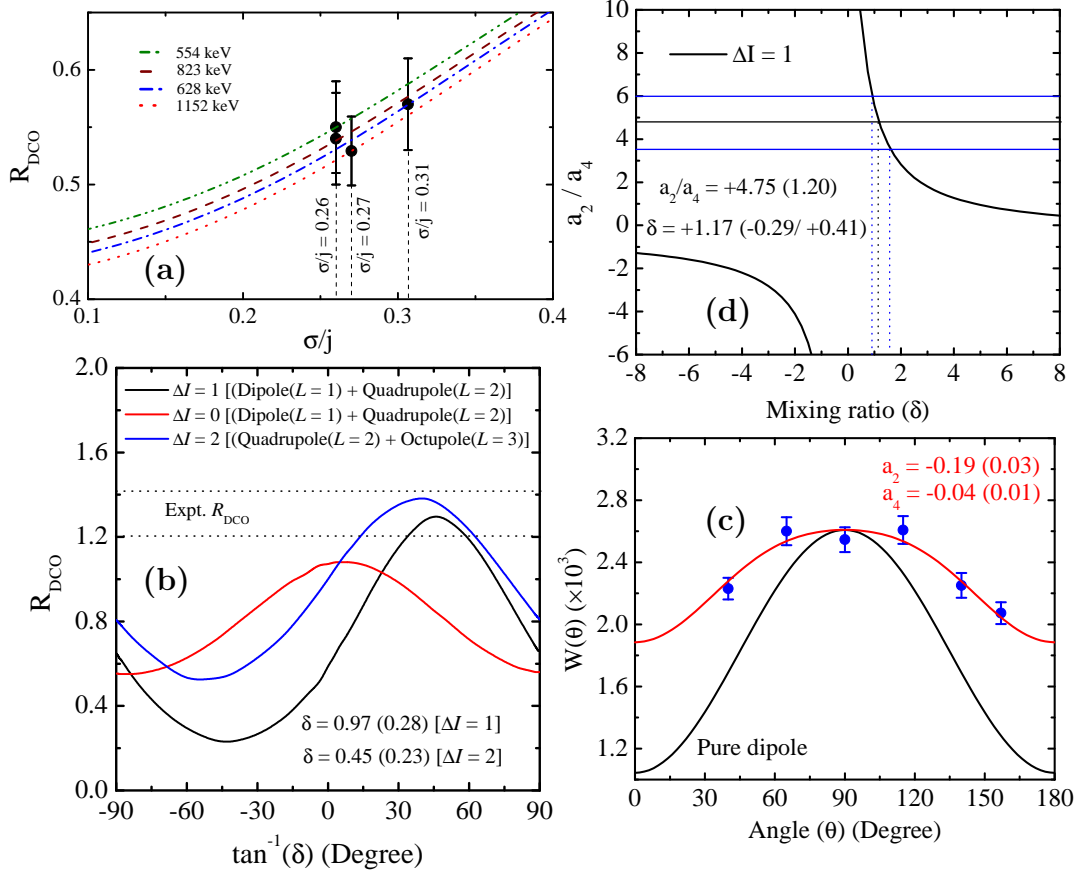


Figure 4.3: In the panel (a) Theoretical DCO ratios (R_{DCO}) for different σ/j value of the reaction (solid curve) for the present experimental setup, calculated using ANGCOR program are plotted. Experimental R_{DCO} values for the 1151.6 keV ($17/2^+ \rightarrow 15/2^-$) $E1$ transition in ^{143}Eu and 553.6 ($25/2^- \rightarrow 23/2^+$), 628.3 ($19/2^+ \rightarrow 17/2^-$) and 823.1 ($21/2^+ \rightarrow 19/2^-$) keV $E1$ transitions in ^{141}Sm (represented by open circle), reproduced assuming $\sigma/j = 0.27$ and $0.26, 0.31$ and 0.26 , respectively. Panel (b) shows the variation of the R_{DCO} with the mixing ratio (δ) having different multipolarity for the 132.6 keV transitions in ^{141}Sm . In the panel (c) angular distribution of the γ transitions 132.6 keV ($27/2^- \rightarrow 25/2^-$) in ^{141}Sm plotted. The solid red line represents the fitted curve of the experimental data points. The solid black line represents the fitted value of the pure dipole transitions. The variation of the ratio of the angular distribution coefficients (a_2/a_4) as a function of mixing ratio is plotted in the panel (d) for the 132.6 keV ($27/2^- \rightarrow 25/2^-$) transitions.

that if the transition is of multipolarity $M1 + E2$ or $E1 + M2$ type, the level lifetime of the depopulating state should be \sim ps and for $M2 + E3$ or $E2 + M3$ case, the level lifetime is \sim μs . The observed level lifetime value is 2.37_{-39}^{+45} ps as measured by DSAM technique (see Table 4.2). This excluded the second possibility ($L = 2 + L = 3$) of multipolarity for the 132.6 keV transition. Thus 132.6 keV transition has dipole character with a substantial amount of quadrupole admixture ($M1 + E2$ or $E1 + M2$), having a mixing ratio of 0.97(28). The mixing ratio has been estimated from the ANGCOR code.

The angular distribution measurement for the 132.6 keV has been carried out to

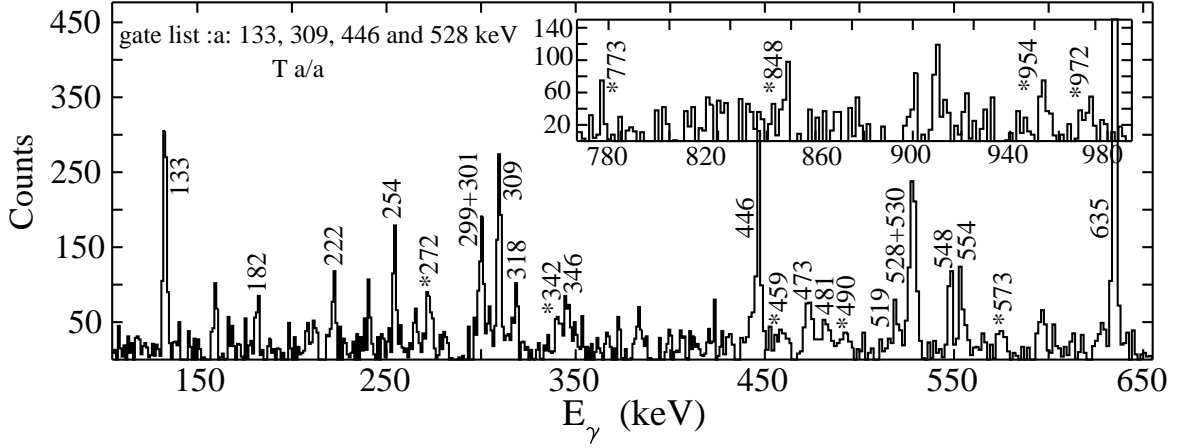


Figure 4.4: The summed double-gated γ -ray spectrum of the 132.6, 309.4, 446.4, and 527.8 keV transitions showing the presence of γ transitions of ^{141}Sm . The asterisk marked peaks are the newly observed member of the dipole bandlike structures in ^{141}Sm .

further resolve the nature of this transition (Figure 4.3 (c)). The normalized yield of the 132.6 keV transition at different detector position was measured and fitted with the Legendre polynomial function [85],

$$W(\theta) = A_0[1 + a_2P_2(\cos\theta) + a_4P_4(\cos\theta)], \quad (4.1)$$

where a_2 and a_4 are the angular distributions coefficients [85]. The fitted values of the a_2 and a_4 coefficients are -0.19(3) and -0.04(1), respectively (Figure 4.3 (c)). It is also in compliance with a mixed dipole ($M1 + E2$) character, of the transition.

The angular distributions coefficients a_2 and a_4 , have also been calculated for 132.6 keV transition by the Yamazaki's prescription [85] as a function of the mixing ratio δ . The ratio of the theoretically calculated angular distribution coefficients a_2/a_4 has been plotted as function of δ . The experimentally measured ratio of a_2/a_4 then plotted on the same graph. From the intersection points, the value of δ (Figure 4.3 (d)) was found to be 1.17^{+41}_{-29} . This value is in compliance with the value obtained from the DCO ratio analysis. Thus, the state deexciting with the 132.6 keV γ -ray emitted is assigned as $I^\pi = 27/2^-$.

Table 4.1: The transition energy (E_γ), the relative intensity (I_γ), the R_{DCO} , the R_θ , the linear polarization (P), the mixing ratio (δ) and the assignment of the γ transitions in ^{141}Sm .

E_γ^a	I_γ^b	J_i^π	J_f^π	R_{DCO}^c	R_θ	P	δ	Assignment
132.6	100.0	$27/2^-$	$25/2^-$	1.31(11)	1.11(7)		0.97(28)	M1/E2
253.7	20.1(28)	$37/2^-$	$35/2^-$	0.72(9)	0.84(7)	-0.23(15)	0.13(8)	M1
272.0	1.7 (4)	$37/2^-$	$35/2^-$					(M1)
299.3	11.5(18)	$39/2^-$	$37/2^-$		0.66(8)	-0.13(10)		M1
300.7	8.5(12)	$37/2^-$	$35/2^-$		0.75(9)	-0.15(11)		M1
309.4	94.1(51)	$29/2^-$	$27/2^-$	0.68(7)	0.63(5)	-0.13(9)	0.11(7)	M1
318.0	11.4(19)	$37/2^-$	$35/2^-$		0.78(9)	-0.21(15)		M1
342.0	3.5(6)	$(39/2^-)$	$37/2^-$					(M1)
345.5	18.4(21)	$39/2^-$	$37/2^-$	0.75(8)	0.81(6)	-0.12(10)	0.16(7)	M1
446.4	63.3(41)	$31/2^-$	$29/2^-$	0.77(10)	0.70(5)	-0.22(11)	0.18(8)	M1
459.0	2.4(5)	$(41/2^-)$	$(39/2^-)$					(M1)
473.0	18.3(35)	$41/2^{(-)}$	$39/2^-$		0.89(10)			(M1)
481.4	16.6(27)	$43/2^{(-)}$	$41/2^{(-)}$		0.92(9)			(M1)
490.0	11.2(21)	$45/2^{(-)}$	$43/2^{(-)}$		0.79(12)			(M1)
527.8	49.7(54)	$33/2^-$	$31/2^-$	0.81(10)	0.69(6)	-0.23(16)	0.22(9)	M1
530.0	12.6(19)	$35/2^-$	$33/2^-$		0.52(4)	-0.18(14)		M1
548.0	28.4(40)	$35/2^-$	$33/2^-$	0.79(8)	0.84(9)	-0.19(12)	0.20(7)	M1
573.0	3.1(6)	$(35/2^-)$	$33/2^-$					(M1)
618.0		$39/2^-$	$35/2^-$					(E2)
773.0	2.9(6)	$41/2^{(-)}$	$37/2^-$					(E2)
848.0	2.3(7)	$37/2^-$	$33/2^-$					(E2)
954.0	1.8(5)	$43/2^{(-)}$	$39/2^{(-)}$					(E2)
972.0	1.1(3)	$45/2^{(-)}$	$41/2^{(-)}$					(E2)

^aUncertainty in γ -ray energy is \pm (0.1-0.3) keV.

^bIntensities of γ rays are normalized to the 132.6 keV transition.

^cDCO ratios are obtained from stretched E2 transition.

The multipole nature of the 132.6 keV was also confirmed from the intensity balance. In the level structure of ^{141}Sm [100], the 132.6 keV transition feeds to $25/2^-$ level, which deexcites through the 553.6 ($25/2^- \rightarrow 23/2^+$) and 59.0 keV ($25/2^- \rightarrow 23/2^-$) transitions. In the current measurements, the clover detectors have insufficient detection efficiency for the low energy γ transitions. As a result intensity of the 59.0 keV transition could not be determined precisely. The 59.0 keV feeding into $23/2^-$ which decays via two transitions of energies 594.7 and 1417.8 keV. The intensities of these decaying transitions were assumed to be the intensity of the feeding transition 59.0 keV. Thus the total feed-out intensity of the decaying transitions of $25/2^-$ (553.6 and 59.0 keV) state can be

compared with the feed-in intensity to the $25/2^-$ state (132.6 and 203.4 keV). The 203.4 keV transition was previously identified as a magnetic dipole [100]. The measured total intensity of the feed out transitions from the $25/2^-$ level is 36.1(42), whereas the feeding intensities for the 203.4 and 132.6 keV transitions were 17.2(14) (including the effect of the internal conversion [104]) and 9.8(11) (without considering the internal conversion), respectively. Therefore, the ratio of the maximum missing intensity to the observed intensity for the 132.6 keV transition and was to be 0.93(18), which is the maximum limit for the total internal conversion coefficient for this transition. Now, if the transition is $M1 + E2$ the total internal conversion coefficient is 0.81_{-1}^{+2} as calculated using the experimentally obtained mixing ratio $\delta = 1.17_{-29}^{+41}$ [104]. This result is in good agreement with the maximum conversion coefficient value 0.93(18). On the other hand, if we assume the 132.6 keV transition as $E1 + M2$, then the conversion coefficient obtained by the calculation is 3.42_{-81}^{+98} [104] using the same mixing ratio. Thus, the intensity balance argument unambiguously assigns the $M1 + E2$ character to the 132.6 keV γ transition in contrast with the pure $M1$ nature established by the earlier analysis.

The other members of the dipole cascade in ^{141}Sm with transitions energy 309.4, 446.4 and 527.8 keV were re-investigated through the DCO ratio, ADO ratio, linear polarization and mixing ratio (δ) measurements in the present analysis, which established them as dipole $M1$ transition with small $E2$ admixture in compliance with the previous measurement [100]. This measurements confirmed the spin-parity assignment the $33/2^-$ level. Above this excited state, Lach *et al.* [100] had also reported the γ transitions of energies 548.1 and the 299.9 keV only. However, Cardona *et al.* [99] proposed a complex structure above the $33/2^-$ level consisting of the 548.0, 530.0, 318.0, 300.7, 299.3, 253.7, and 345.5 keV γ transitions and extended the level scheme up to $I = 39/2$ without any parity assignment.

In the present analysis, a double-gated spectrum was created by the gate list with γ energies 132.6, 309.4, 446.4 and 527.8 keV. In this spectrum, a new weak transition of

573.0 keV has been observed (Figure 4.4). This new transition was found to be absent in the coincidence spectrum produced by the gate list and the 548.0 keV transition. Hence, the newly observed 573.0 keV transition placed above the 527.8 keV and in parallel to the 548.0 keV feeding to the $33/2^-$ level (Figure 4.2). Because of the weak nature of the 573.0 keV transition, the DCO ratio, the ADO ratio and the linear polarization measurement were not possible. Thus, 573.0 keV transition has been tentatively assigned as of dipole nature. The dipole structure formed by the transitions of energies 132.6, 309.4, 446.4, 527.8 and 573.0 keV has been designated as dipole band I (DB I) in Figure 4.2. In the double gates between the any one transition of the DB I and the 299.3 or 300.7 keV transition, the 253.7 and 345.5 keV transitions were found to be absent which upholds the proposition of Cardona *et al.* [99]. For the 548.0, 253.7 and 345.5 keV γ transitions, the values of the DCO ratio, ADO ratio, linear polarization measurement, and δ values confirmed their mixed ($M1/E2$) character and the spin-parity of the deexciting states were assigned as $35/2^-$, $37/2^-$ and $39/2^-$ respectively. The estimated ADO ratio and the linear polarization values for the 530.0 and 318.0 keV transitions indicate their $M1$ nature and the states depopulating through these transitions have been established as $35/2^-$ and $37/2^-$, respectively. Due to the weak nature of the 473.0 and 481.4 keV transitions, only the ADO ratio measurement was possible, which confirmed their dipole character. Therefore, the spin-parity of the corresponding levels were tentatively assigned as $41/2^{(-)}$ and $43/2^{(-)}$, respectively. Above the $43/2^{(-)}$ state a new γ transition of energy 490.0 keV was observed and placed. For this transition the DCO ratio and the linear polarization measurements could not performed due to low statistics. However, the measured R_θ value indicated a dipole character and the spin-parity of the corresponding state was assigned as $45/2^{(-)}$. We have also observed two weak crossover $E2$ transitions of energies 972.0 keV and 954.0 keV, which confirmed the present level structure. The dipole cascade consisting of the 283.7, 345.5, 473.0, 481.4 and 490.0 keV has been labeled as dipole band II (DB II) as shown in Figure 4.2. Two new transitions of 342.0 and 459.0 keV (Figure 4.4) were observed above the 318.0 keV and parallel to the DB II. We could

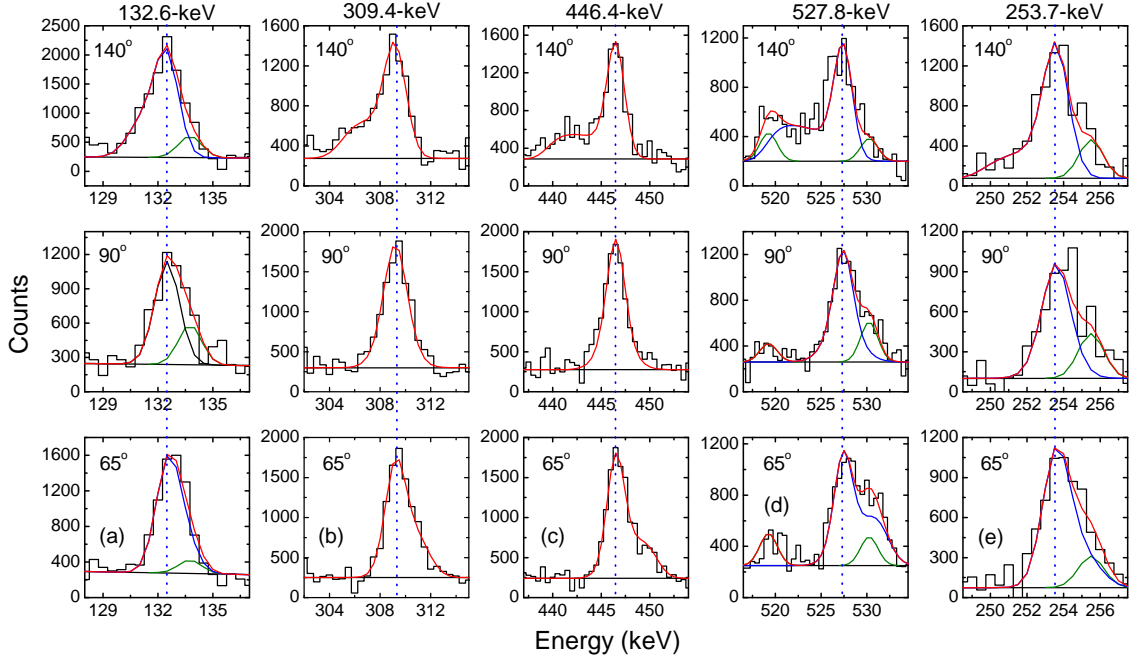


Figure 4.5: The observed line shapes along with the fitted curve for the γ transitions (a) 132.6, (b) 309.4, (c) 446.4 and (d) 527.8 and (e) 253.7 keV of the dipole sequence DB I and DB II in ^{141}Sm . The top, middle and bottom rows stand for the shapes at the 140° , 90° and 65° detectors, respectively. The experimentally obtained line shapes of γ transitions, the contaminant peaks, and the total line shapes are represented by the blue, olive and red curves, respectively. The dotted lines represent the peak position for each transition.

not perform the spectroscopic measurements of these two γ transitions owing to their weak nature. The states decaying by the 342.0 and 459.0 keV transitions, have been tentatively assigned as $(39/2^-)$ and $(41/2^-)$, respectively. This dipole band structure has been assigned as dipole band III (DB III) (Figure 4.2). In the sum of double gated spectrum (Figure 4.4) we have observed three interband transitions from DB II to DB III, namely 272.0, 299.3 and 773.0 keV, and one from DB III to DB II, namely, 848 keV.

In order to explore the nature of DB I, DB II and DB III, the level lifetime measurements have been performed. The Doppler-broadened line shapes were observed for the transitions above the $I^\pi = 27/2^-$ in ^{141}Sm . The level lifetimes of the high spin states have been extracted by fitting the observed lineshapes with the LINESHAPE code of Wells and Johnson [97].

In DB II, 345.5 keV γ transition ($39/2^- \rightarrow 37/2^-$) is the topmost transition for which a clear line shape was observed in the experimental gated spectra. An effective

lifetime of 1.15 ps was estimated for $I^\pi = 39/2^-$. This effective lifetime has been used in the subsequent fitting of the lineshapes for the lower states. The $35/2^-$ level is fed by two transitions of 253.7 and 300.7 keV, both from two different $37/2^-$ levels and both the transitions show Doppler shapes. The level lifetime of the $37/2^-$ state depopulating by the 253.7 keV transition was determined by the same procedure discussed above. But the lifetime determination of the other $37/2^-$ state of DB III, depopulated by the 300.7 keV transition, was difficult due to the presence of the overlapping 299.3 keV transition ($39/2^-$ state in band II to $37/2^-$ state in band III). The 299.3 keV (DB II) and 300.7 keV (DB III) transitions were fitted simultaneously and the lifetime of the $39/2^-$ state was kept fixed at 1.15 ps (obtained from the lineshape fitting of the 345.5 keV transition). This way, the lifetime of the $37/2^-$ state deexciting through the 300.7 keV transition was estimated. Subsequently, the intensity weighted average lifetimes of the $37/2^-$ states depopulating by the 253.7 and 300.7 keV transitions were used as the feeding time for the lineshape fitting of the 548.0 keV transition. The lineshapes were not observed for the 530.0, 318.0, 473.0, 481.4 and 490.0 keV transitions. This may be due to the less statistics. The uncertainties in the level lifetime have been calculated from the standard procedures of χ^2 fit in the vicinity of χ_{min}^2 . The typical fitted spectra are shown in Figure 4.5. The systematic errors as a result of the uncertainty in the stopping power of the target/backing medium, which can be as large as 15%. This uncertainty has not been included in the quoted errors of the level lifetimes. The extracted level lifetimes and the corresponding reduced transition probability $B(M1)$ values have been tabulated in Table 4.2.

4.4 Discussion

The DB I shows regular spacing in its transition energies starting from the state $I^\pi = 25/2^-$ to $I^\pi = (35/2^-)$ in ^{141}Sm . Similar dipole bands have also been reported in the neighboring nuclei $^{139,142}\text{Sm}$, $^{141,143}\text{Eu}$ and ^{142}Gd . These dipole bands have been

Table 4.2: The measured level lifetimes and the corresponding $B(M1)$ values for the dipole bands I and II in ^{141}Sm .

Band	I_i^π	$E_\gamma(k\text{eV})$	$\tau(\text{ps})$	$B(M1)\mu_N^2$
I	$27/2^-$	132.6	2.37_{-39}^{+45}	2.92_{-48}^{+55}
	$29/2^-$	309.4	1.05_{-18}^{+21}	1.54_{-26}^{+31}
	$31/2^-$	446.4	0.72_{-13}^{+15}	0.75_{-14}^{+16}
	$33/2^-$	527.8	1.11_{-15}^{+23}	0.29_{-4}^{+6}
II	$35/2^-$	548.0	0.40_{-8}^{+8}	0.72_{-14}^{+14}
	$37/2^-$	253.7	1.88_{-35}^{+40}	1.45_{-27}^{+31}
	$39/2^-$	345.5	1.15^a	0.97^b
III	$37/2^-$	318.0	1.14_{-18}^{+21}	0.89_{-14}^{+16}

^aEffective lifetime is obtained assuming 100% side-feeding intensity.

^bLower limit of the $B(M1)$ value.

identified as magnetic rotation (MR) bands based on the characteristic decrease in the $B(M1)$ values with increase in angular momenta along the band [1]. The observed $B(M1)$ values in DB I were found to be comparable with values of the dipole bands in $^{139,142}\text{Sm}$, $^{141,143}\text{Eu}$ and ^{142}Gd nuclei, and the values also show a decreasing trend with increasing spin (Table 4.2). The observed $B(M1)$ values for DB II are comparatively smaller and does not change significantly with spin (Table 4.2).

The properties of the dipole bands in weakly deformed nuclei can be described by the semi-classical model calculations within the framework of Shears Mechanism with the Principal Axis Cranking (SPAC) model [6–8]. In this model, the shears angular momentum (\mathbf{j}_{sh}) generated from the coupling of proton-neutron quasiparticles is coupled with the collective angular momentum (\mathbf{R}) of the weakly deformed core to produce the observed angular momentum state I .

The odd mass $N = 79$ nuclei in the mass region $A \sim 140$, ^{139}Nd [105, 106], ^{141}Sm [99, 100] and ^{143}Gd [107] has dipole bands above the $25/2^-$ state at the excitation energies 3.8, 3.4 and 3.1 meV, respectively. The dipole bands in odd mass $N = 77$ ^{139}Sm [9] and $N = 78$ ^{141}Eu [33] also exist above the same angular momentum state at the excitation energies 3.3 and 2.8 MeV, respectively. Among them, the dipole bands in ^{139}Sm and ^{141}Eu were

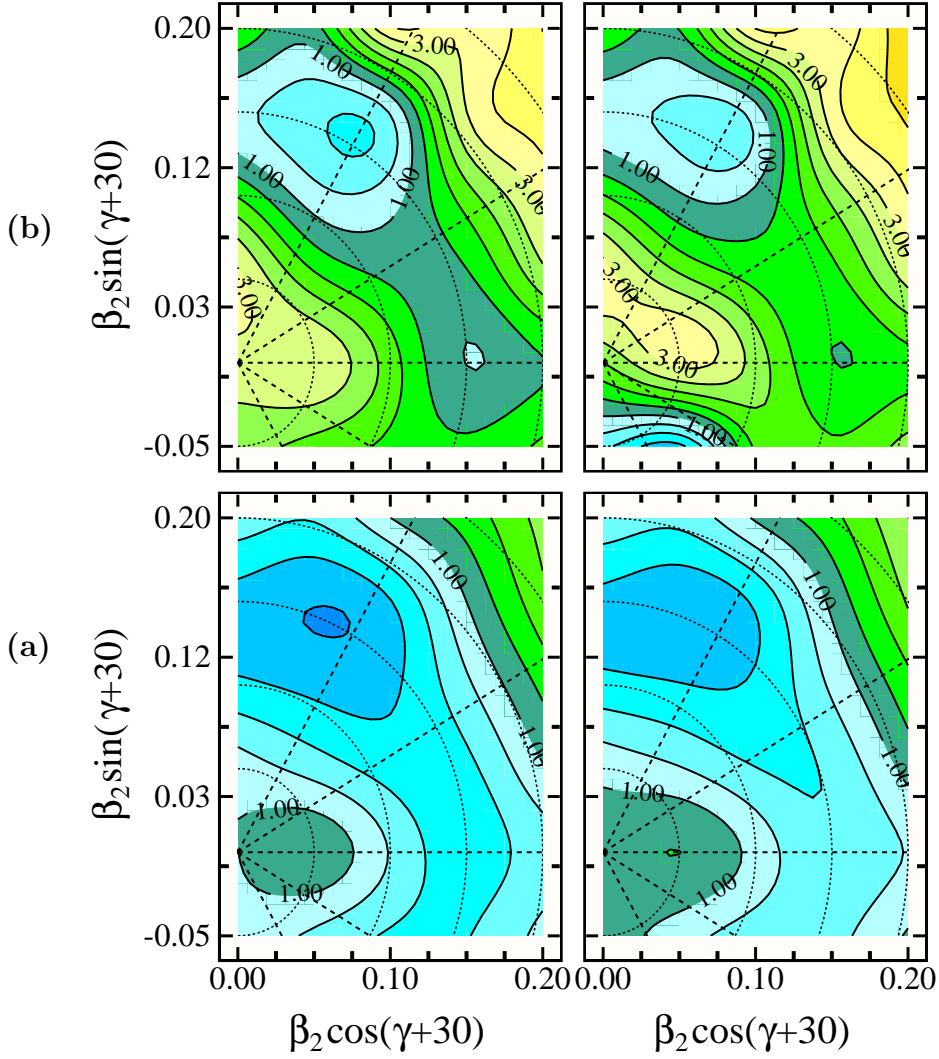


Figure 4.6: The TRS contour plots for the configurations (a) $\pi h_{11/2}^2 \otimes \nu h_{11/2}^{-1}$ and (b) $\pi h_{11/2}^2 \otimes \nu h_{11/2}^{-3}$ corresponding to DB I and DB II, respectively. The rotational frequency (ω) used for the calculations are (a) 0.17 and (b) 0.21 MeV. The energy spacing between two contours is 0.40 MeV.

identified as magnetic rotational band with the configurations $\pi h_{11/2}^2 \otimes \nu h_{11/2}^{-1}$ and $\pi h_{11/2}^1 \otimes \nu h_{11/2}^{-2}$, respectively. Hence, the dipole bands with bandhead energy ≈ 3.0 MeV in the odd mass nuclei in mass $A \sim 140$ region may arise from three quasiparticle configuration and all are in $h_{11/2}$ orbital. Thus, the configuration of the DB I in ^{141}Sm has been assumed to be $\pi h_{11/2}^2 \otimes \nu h_{11/2}^{-1}$. This configuration could reproduce the bandhead spin with a small angular momentum contribution from core rotation ($1\hbar$). To understand the shape (prolate/ oblate /triaxial) of the ^{141}Sm nucleus associated with the above-mentioned configuration, the Total Routhian Surface (TRS) calculation [25, 63] has been

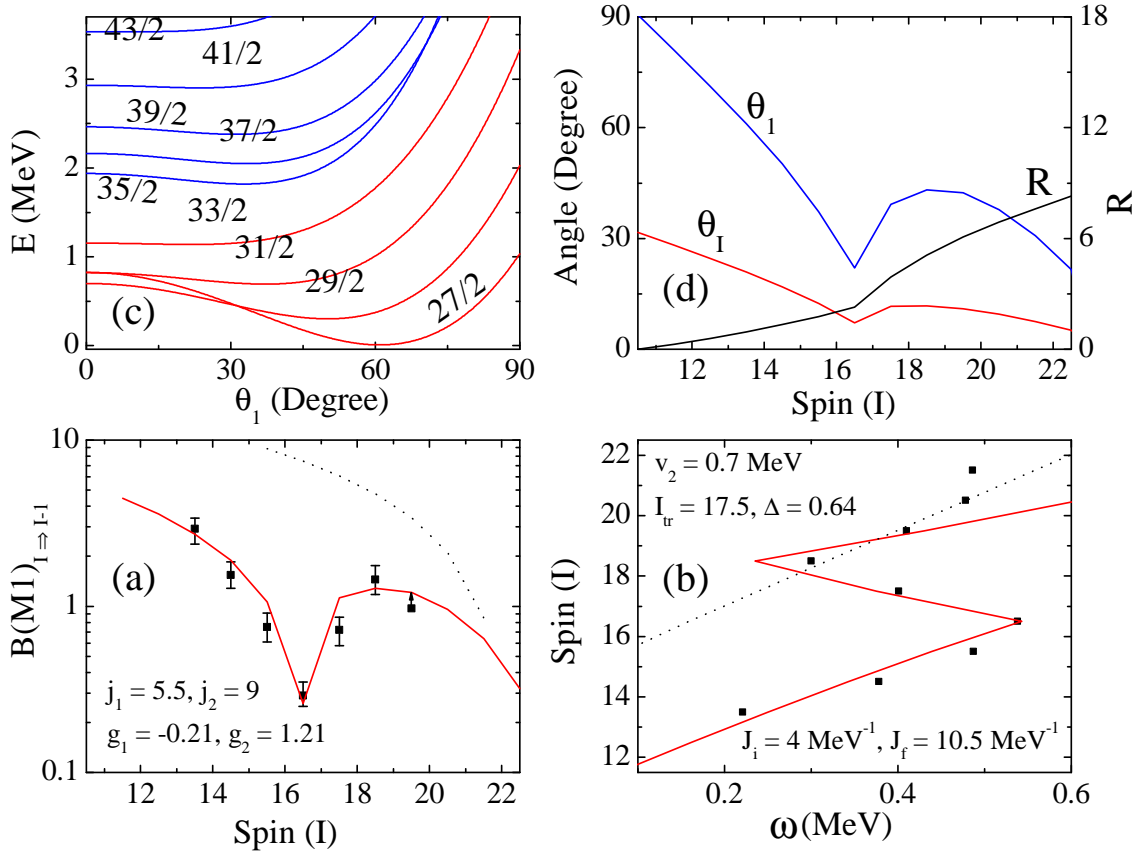


Figure 4.7: Comparison of the experimental results (solid squares) for the sequence DB I and DB II in ^{141}Sm in the SPAC model calculations (solid lines): (a) $B(M1)_{I \Rightarrow I-1}$ values against angular momentum (I), (b) Total spin (I) vs ω , (c) total energy of the excited states as a function of θ_1 and (d) Variation of the angle θ_1 (solid blue line), θ_I (solid red line) and core angular momentum (R) (solid black line) as a function of spin for the DB I and DB II. Here, θ_I is the angle between the total angular momentum vector (I) and the collective core rotational angular momentum (R). The parameters used for the calculations are given in the figures.

performed. The contour plots from the TRS calculations are shown in Figure 4.6. It can be noted from Figure 4.6, the DB I has a minimum potential energy for prolate deformation $\beta_2 \approx 0.15$. Thus, this deformation has been considered in the SPAC model calculation with normal initial alignment [8].

Thus, SPAC calculation has been performed for DB I, using the proposed configuration $\pi h_{11/2}^2 \otimes \nu h_{11/2}^{-1}$ and assuming the unstretched condition of the angular momenta with $j_1 = 5.5\hbar$, $j_2 = 9\hbar$, $g_1 = -0.21$ and $g_2 = +1.21$ [8]. Under these assumptions, the energy levels, the $B(M1)$ values and the spins were well reproduced by the one dimensional minimization condition as shown in Figure 4.7 (a), (b) and (c). The spin dependence of the θ_1 , θ_I and R are depicted in Figure 4.7 (d). The observed reduced transition

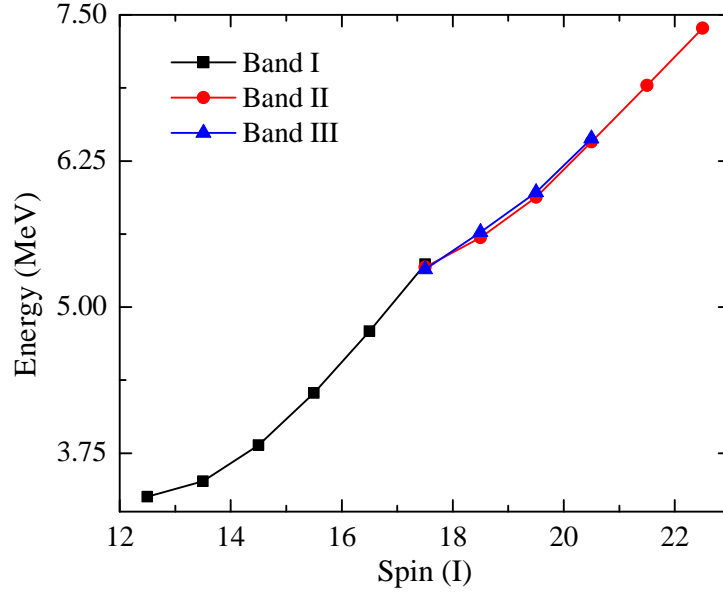


Figure 4.8: The variation of excitation energies with spin for the dipole bands DB I, DB II and DB III in ^{141}Sm .

probabilities for the dipole transitions of DB I and the rotational frequency ($\hbar\omega$) have been plotted as a function of the total angular momentum along with the calculated values (Figure 4.7 (a)). The experimental $B(M1)$ values decrease from $2.92_{-48}^{+55} \mu_N^2$ to $0.29_{-4}^{+6} \mu_N^2$ which have been well reproduced by the numerical values for the proposed configuration $\pi h_{11/2}^2 \otimes \nu h_{11/2}^{-1}$, which could generate maximum angular momentum state $35/2^-$. The SPAC calculation predicted that at this spin, the $B(M1)$ value vanishes, which could be attributed to the fact that the shears blades formed by the particles and the holes angular momentum vectors were almost parallel. As a result, the transverse component of the magnetic dipole moment (μ_{\perp}) vanished. Hence, no high spin state beyond $35/2^{(-)}$ could be generated from the $\pi h_{11/2}^2 \otimes \nu h_{11/2}^{-1}$ configuration assigned for the DB I. Thus, the 573.0 keV transition above the $33/2^-$ level represent the termination of the DB I.

Above the $33/2^-$ level, two dipole bands, DB II and DB III have been observed. As discussed earlier, DB I has the three quasiparticle configuration $\pi h_{11/2}^2 \otimes \nu h_{11/2}^{-1}$. Figure 4.8 shows the excitation energy ($E(I)$) against spin (I) for the DB I, DB II and DB III in ^{141}Sm . From this figure it may be concluded that DB II and DB III have a quasiparticle

configuration which is different from three quasiparticle configuration ($\pi h_{11/2}^2 \otimes \nu h_{11/2}^{-1}$) assigned to DB I. The Figures 4.9 (a) and (b) show the quasiparticle alignment (i_x) and the experimental routhians (e') plot as a function of the rotational frequency (ω) for the DB I, DB II and DB III. It may be noted that the DB I and DB II cross at the rotational frequency ~ 0.37 MeV and the DB II has an alignment gain $\sim 6\hbar$ with respect to the DB I.

The particles alignment in this mass region occur mostly in the low Ω $h_{11/2}$ protons and the high Ω $h_{11/2}$ neutrons orbitals. For prolate shapes ($\gamma = 0^\circ$), the alignment frequency for the lower midshell $h_{11/2}$ protons is ≈ 0.30 MeV, whereas upper-midshell $h_{11/2}$ neutrons have much higher alignment frequency (≈ 0.40 MeV). However, as the nucleus moves toward more triaxial shape ($\gamma > 0^\circ$) with increase in excitation, the crossing frequency for the protons increases while it decreases for the neutrons. In this mass $A \approx 140$ region, the nuclei are best known for γ softness. Thus the observed crossing (at $\omega \sim 0.37$ MeV) may be either due to the alignment of a pair of neutrons or protons. The observed gain ($\sim 6\hbar$) of the aligned angular momentum is not consistent with the alignment of two protons in low Ω orbitals of $h_{11/2}$. However, this gain is well understood if one considers the alignments of neutrons in high Ω orbitals of $h_{11/2}$. Such high Ω neutron alignment has been observed in neighboring nuclei [108, 109]. Thus, the five quasiparticle configuration $\pi h_{11/2}^2 \otimes \nu h_{11/2}^{-3}$ has been assigned to the DB II.

The TRS calculations for the above-mentioned configuration predict a prolate minimum at $\beta_2 \approx 0.16$ (Figure 4.6). The SPAC model calculation has been performed for the DB II with of $j_1 = 10.5\hbar$ and $j_2 = 9\hbar$ for the proposed configuration $\pi h_{11/2}^2 \otimes \nu h_{11/2}^{-3}$, and by assuming the same contribution from the core as in DB I (moment of inertia of the core $J \sim 4.0 \hbar^2/\text{MeV}$). These calculations failed to reproduce the measured $B(M1)$ and $I(\omega)$ values simultaneously, as shown by the dotted line in Figure 4.7 (a) and (b). This seems to indicate that the DB II may not originate solely from the coupling of the multi-quasiparticles angular momenta (shears mechanism) with minimum contribution

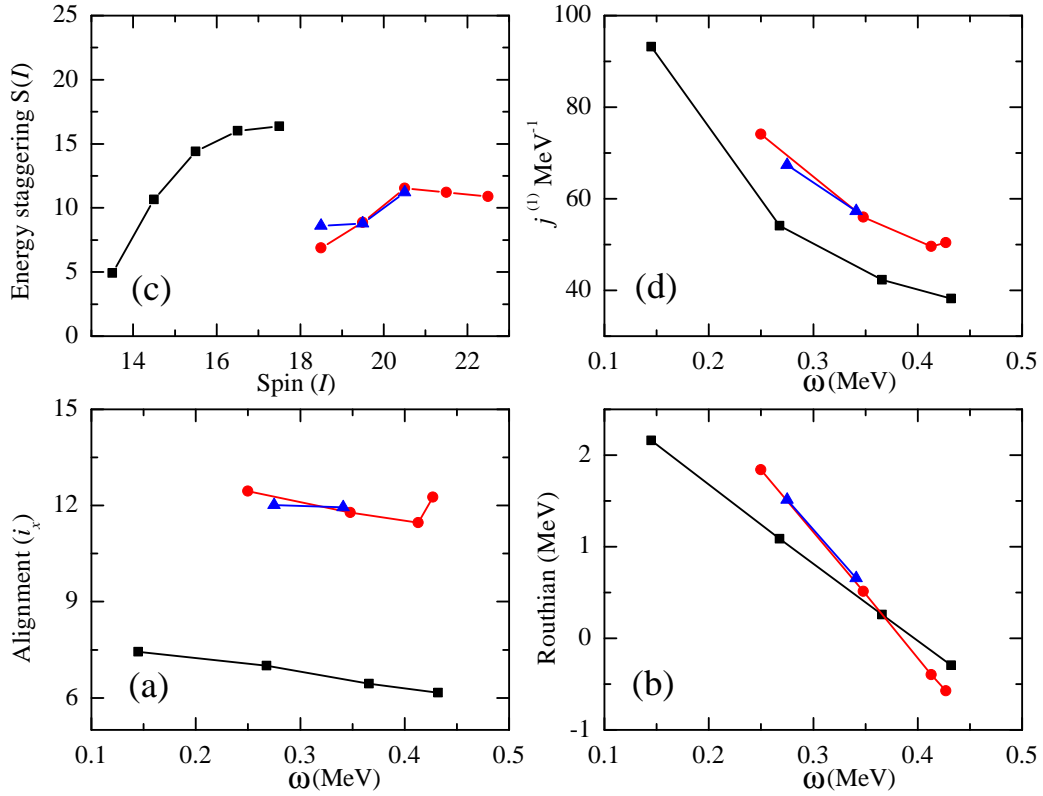


Figure 4.9: The comparison of the experimental results of (a) the quasiparticle aligned angular momentum (i_x), (b) the quasiparticle routhians (ϵ), (c) the energy staggering $S(I) = [E(I) - E(I-1)]/(2I)$ and (d) the kinetic moment of inertia ($j^{(1)}$) for the dipole bands DB I, DB II and DB III in ^{141}Sm .

from core rotation. Therefore, the core contribution was included in the SPAC model calculations through the variation of the core moment of inertia (J) as specified in the ref. [110]. This modification leads to a good reproduction of the experimental $B(M1)$ and $I(\omega)$ values, using the one-dimensional minimization condition as demonstrated in Figure 4.7. The calculations show that the rotational contribution (R) increases rapidly from the $I^\pi = 33/2^-$ as depicted in Figure 4.7 (d). Consequently, the spins (I) of the states of the DB II are found to increase rapidly with a small increase in rotational frequency ω as shown in Figure 4.7 (b).

To investigate this phenomena, the experimentally observed spins (I) are plotted against the rotational frequency ($\hbar\omega$) for the MR bands reported in Sm, Eu, Gd [8, 9, 33, 34] isotopes in Figure 4.10. The spins (I) are found to increase smoothly with the rotational frequency except in the case of ^{139}Sm and ^{141}Sm nuclei. In ^{139}Sm nucleus, sub-

stantial angular momentum is generated with small increase in the rotational frequency at the end of the band. The Tilted Axis Cranking (TAC) calculations for this MR band showed that the experimental results are better reproduced with the assumption that the contribution from the collective angular momentum is increasing with rotational frequency (ω), which is due to the rotation around the intermediate axis of a triaxial core [9]. Also, the experimental $B(M1)$ values at low spin states can be well explained for the $\gamma = 0^\circ$, but at higher spins, the agreement is better for $\gamma = -25^\circ$. A similar situation may arise in the case of ^{141}Sm . In this case, the $I(\omega)$ plot show a back-bending followed by a sudden increase of the collectivity at the end of the band. Thus, the quasiparticle alignment in ^{141}Sm may lead to a more deformed shape. In this case the rate of fall in the $B(M1)$ values is expected to be slower than that for DB I. But, these transitions rated could not be measured above the $39/2^-$ level due to the lack of statistics in the line shape spectra. However, it may be noted that two new $E2$ transitions have been observed above $I^\pi = 39/2^-$ level while they are absent below. This may also indicate increase of collectivity. Nonetheless, more investigation is needed to explore the structure of the states above the $39/2^-$ state (DB II) in ^{141}Sm , for an unambiguous interpretation.

The DB III has the same parity and very similar in excitation energy and aligned angular momentum to that of the DB II. These observations indicate that both the dipole bands DB II and DB III are associated with the same proton-particle and neutron-hole configuration. The existence of several linking transitions between the DB II and DB III also implies that they have similar quasiparticle structure. Thus, the DB III probably has the five quasiparticle configuration $\pi h_{11/2}^2 \otimes \nu h_{11/2}^{-3}$. This quasiparticle configuration is favorable for a chiral system, because the angular momentum vectors of the valence protons and the neutrons occupy the high- j particle-like and the high- j hole-like $h_{11/2}$ orbitals which align along the short and long axes, respectively and the angular momentum vector due to the core rotation can orient along the intermediate axis. This mutual perpendicular coupling of the three angular momenta opens up the possibility of the observation of the spin chirality. The chiral doublet bands have been observed

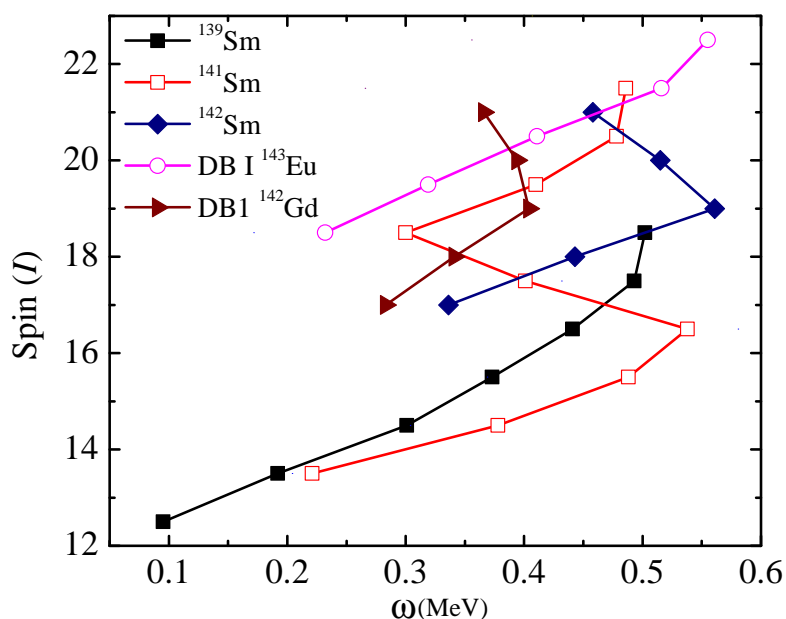


Figure 4.10: The comparison of the observed angular momentum of the $^{139,141,142}\text{Sm}$, ^{143}Eu and ^{142}Gd nuclei [8, 9, 33, 34] with rotational frequency (ω).

in several odd-odd and odd- A nuclei are built on two and three quasiparticle configurations [111–118]. Recently, a four quasiparticle chiral doublet band has been identified in ^{194}Tl [117].

The partner bands DB II and DB III, in ^{141}Sm show excellent similarities in the measured quasiparticle alignment, quasiparticle routhians, energy staggering and kinetic moment of inertia, as shown in Figs. 4.9 (a), (b), (c) and (d), support the chiral scenario. The absence of staggering of the $S(I)$ values for the dipole bands II and III indicates weak Coriolis interactions resulting from perpendicular angular momenta coupling of the single particles and of the core. Also the levels of DB II and DB III are nearly degenerate (separated by not more than 50 keV) in the observed spin region $I = 35/2$ to $41/2$ (Figure 4.8). Thus DB II and DB III exhibits all the features of chiral doublets.

This proposition needs to be tested through the measurement of the electromagnetic transition rates in DB II and DB III. However, the observed properties of DB II and DB III suggest that the ^{141}Sm has triaxial deformed nuclear shape at the higher spin states. Thus, it may be inferred that a transition of the nuclear shape, from prolate to triaxial

exist in ^{141}Sm , which can be associated with the alignment of a pair of neutrons in the high Ω orbitals of $h_{11/2}$ in ^{141}Sm .

4.5 Summary

In summary, high spin dipole structures in ^{141}Sm have been investigated using the reaction $^{116}\text{Cd} (^{31}\text{P}, \text{p}5\text{n})$. The dipole bands DB I, DB II and DB III have been established from the DCO ratio, anisotropy and linear polarization measurements of the associated γ -ray transitions. The level lifetimes of these bands have been measured using the DSAM technique. The experimental $B(M1)$ values, as well as the rotational frequencies (experimental routhian), have been well reproduced with the SPAC model calculation for the DB I. These calculations indicate that the excited states of the DB I originate from the shears mechanism.

The dipole bands DB II and DB III exhibit excellent similarities in all the observed spectroscopic properties. The five quasiparticle configuration $\pi h_{11/2}^2 \otimes \nu h_{11/2}^{-3}$ has been assigned to these bands, which have been identified as a possible candidates for the chiral partner bands. The emergence of the doublet bands indicate a possible evolution from the prolate to the triaxial shape in ^{141}Sm .

CHAPTER 5

Structural Evolution in ^{142}Eu

5.1 Introduction

The nucleus, ^{142}Eu ($N = 79$, $Z = 63$), has one proton hole in the $g_{7/2}/d_{5/2}$ orbitals and three neutron holes in $h_{11/2}$ orbitals. The protons can be easily promoted to the $\pi h_{11/2}$ orbital, thereby, generating a favorable configuration for the shears mechanism (or TAR) [8, 33, 34, 42, 43]. Also, the occupancy of valence nucleons (proton particles and neutron holes) in the shape driving $h_{11/2}$ orbital may lead to the deviation of the mass/charge distribution from its spherical symmetry [34, 119]. In conjunction, the presence of the proton particles in the $d_{5/2}$ and $h_{11/2}$ orbitals may lead to the emergence of octupole correlation in ^{142}Eu . Consequently, the ^{142}Eu nucleus is a prospective system to exhibit the quadrupole (deformed), octupole and the quasiparticle (weakly deformed shape) excitations and possible interplay in between them leading to the coexistence of all these three modes. The earlier reported level scheme of ^{142}Eu is indicative of such coexistence [90]. Recently, the chiral symmetry breaking bands [120] connected by octupole correlations in ^{124}Cs [121] have been reported, which offers a classic example of the interplay between axially asymmetric and reflection-asymmetric shapes. Furthermore, the octupole correlations between multiple chiral doublet bands ($M\chi D$) [122] has been

reported in ^{78}Br [123], which has been supported by the calculations based on microscopic multidimensionally-constrained covariant density functional theory (MDC-CDFT) [18–20]

Thus, the present work aims to establish the presence of the MR band along with AMR in the odd-odd ^{142}Eu isotope along with the search for the octupole correlations in the same system.

5.2 Experimental Results

The nucleus ^{142}Eu was studied previously by M. Piiparinen *et al.* [90] using the $^{110}\text{Pd}(^{37}\text{Cl}, 4n)$ reaction with the NORDBALL Compton-suppressed multidetector array facility. Different quadrupole and dipole bandlike structures above the state 10^+ were reported. The spin - parity of the states were assigned only by the anisotropy ($R(\theta)$) measurements. In the present experiment high spin states of ^{142}Eu were populated by the fusion evaporation reaction $^{116}\text{Cd}(^{31}\text{P}, 5n)$ at a beam energy of 148 MeV obtained from the Pelletron - LINAC facility at TIFR, Mumbai. The depopulating γ rays were detected by INGA. During the experiment, INGA consisted of 19 Compton suppressed clover detectors at six different angles.

All the previously observed transitions in the negative parity structure and the positive parity states in ^{142}Eu (Figure 5.1) were confirmed in the present work from the coincidence intensities (Figure 5.2), DCO ratio (R_{DCO}), ADO ratio (R_θ), mixing ratio and linear polarization (P) measurements [8, 43]. The level structures in ^{142}Eu which are relevant to the present thesis, are discussed in following sections.

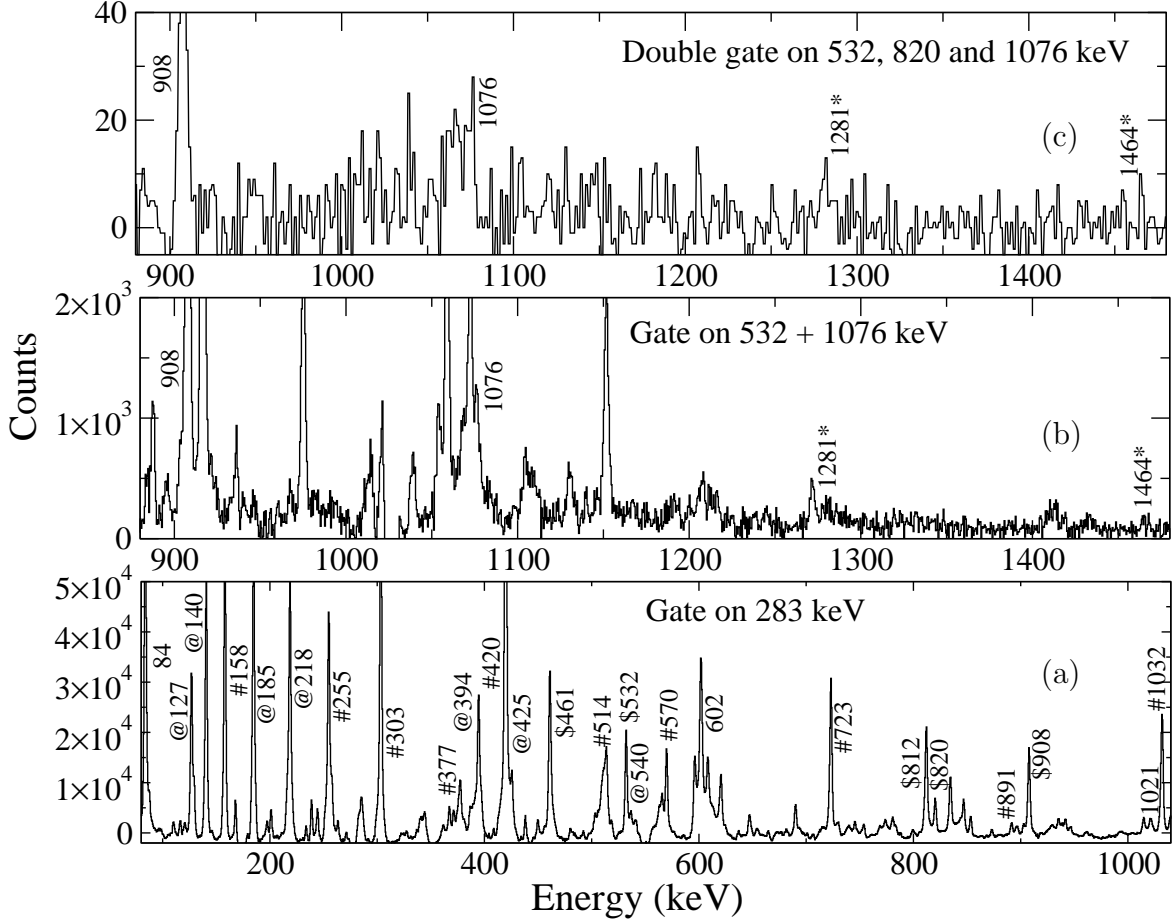


Figure 5.2: (a) The coincidence spectrum of the ground state transition 282.6 keV of ^{142}Eu . This spectrum shows the γ transitions of QB I, DB I and DB II marked by ‘\$’, ‘#’ and ‘@’, respectively; (b) and (c) represent the coincidence spectra in which two newly observed transitions (asterisk marked) of QB I were identified.

5.2.1 Quadrupole structure QB I

The earlier investigation on ^{142}Eu has reported a cascade of $E2$ transitions of energies 811.7, 907.6, 460.6, 532.0, 820.1 and 1075.8 keV, respectively, above the 1397 keV state (11^+), which was found to depopulate via the 601.5, 1021.1 and 1104.5 keV γ transitions. The spin - parity (I^π) of this state was assigned to be 11^+ based on the $R(\theta)$ measurements of the depopulating transitions. In the present work, this assignment has been scrutinized by re-evaluating the electromagnetic character of the de-exciting transitions and the state has been reassigned as $I^\pi = 11^-$ (Figure 5.1). The measured angular distribution along with the fitted curve for the three 601.5, 1021.1 and 1104.5 keV feed out transitions from the 1397.0 keV level are shown in Figure 5.3 (a), (b). The angular distribution

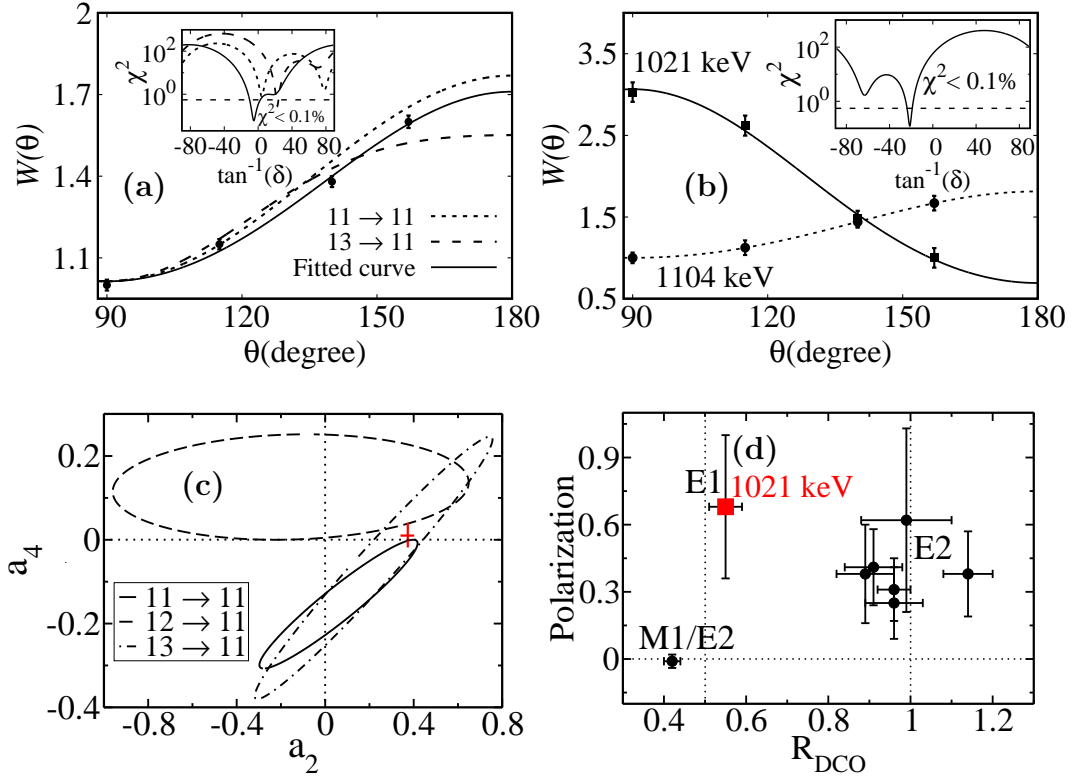


Figure 5.3: (a) The measured angular distribution (in arbitrary unit) along with the fitted curve (solid line) for the 601.5 keV transition. The theoretical distribution of this transition for the spin sequences $13 \rightarrow 11$ (dashed line) and $11 \rightarrow 11$ (dotted line) are also shown. The χ -square of angular distribution coefficients for different mixing ratio (δ) plotted in the inset of this figure for the spin sequence $13 \rightarrow 11$ (dotted line), $12 \rightarrow 11$ (dashed line) and $11 \rightarrow 11$ (solid red line), respectively; (b) shows the experimental angular distributions along with the fitted curves for the 1021.1 (solid line) and 1104.5 keV (dotted line) transitions. The χ -square analysis assuming the spin sequence $12 \rightarrow 11$ is shown in the inset of this figure and gives the mixing ratio $\delta = -0.39(0.01)$; (c) the angular distribution coefficients a_2 vs. a_4 plot for different mixing ratio (δ) using multiple spin sequence [85]. The red cross indicates the data point for the 601.5 keV transition; (d) the polarization value against DCO ratio (R_{DCO}) for different transitions of the observed quadrupole structure QB I in ^{142}Eu . The value of 1021.1 keV transition has been highlighted in red

of the 1021.1 keV transition (Figure 5.3 (b)) exhibits a pure dipole like nature with coefficients $a_2 = -0.75(1)$ and $a_4 = +0.07(6)$, whereas the 1104.5 keV transition displays a quadrupole like character with angular distribution coefficients $a_2 = +0.42(1)$ and $a_4 = +0.03(1)$. Along with that the measured R_{DCO} and the $R(\theta)$ values for the 1021.1 keV transition (given in Table 5.1), indicate it as a pure dipole like transition, which is in contradiction with the previous measurement as mixed dipole transition [90]. The mixing ratio δ of value 0.39(0.01) for this transition has been estimated by the χ^2 minimization in Figure 5.3 (b) inset, which is very small depicting its pure nature. The linear polarization value of 1021.1 keV transition is 0.68(32) (Figure 5.3 (d)) establishing it as an electric

dipole transition ($E1$), which again does not match with the earlier assignment [90]. Consequently the spin-parity of the state 1397 keV is reassigned as $I^\pi = 11^-$. This assignment requires the $E1$ nature of the 601.5 keV ($\Delta I = 0$) and the $M2$ character for the 1104.5 keV transition. But, due to the less statistics at 90° , the polarization measurement for the 1104.5 keV transition was not possible. The multipolarity measurement for the 601.5 keV transition was consistent with the 11^- assignment for the 1397 keV state. The angular distribution curves for the 602 keV transition have been plotted using different spin sequence ($11 \rightarrow 11$ and $13 \rightarrow 11$) (for $\delta = 0$) along with the experimental data points in Figure 5.3 (a). This indicates the 601.5 keV as $\Delta I = 2$ or $\Delta I = 0$ transition with coefficients $a_2 = +0.37(3)$ and $a_4 = +0.01(3)$. The coefficients a_2 and a_4 for the all possible values of mixing ratio δ were calculated and the contours of calculated a_4 vs a_2 values have been plotted for different spin combination ($11 \rightarrow 11$, $12 \rightarrow 11$ and $13 \rightarrow 11$) in Fig 5.3 (c). The observed values of a_2 and a_4 ($a_2 = +0.37(3)$, $a_4 = +0.01$) falls on the contour of $\Delta I = 0$ ($11 \rightarrow 11$) with mixing ratio $\delta = 0.09(0.01)$. Thus, the 601.5 keV is a $\Delta I = 0$ dipole transition. Also the simultaneous χ^2 square minimization (inset of Figure 5.3 (a)) showed the confidence limit $< 0.1\%$ for $\Delta I = 0$ of the 601.5 keV transition with $\delta = 0.09(0.01)$. The uncertainty in δ was determined from the usual procedure of finding the region of “one-standard-deviation” of χ_{min}^2 . These results are consistent with the $E1$ nature of the 1021.0 keV transition. The polarization measurement of the 601.5 keV transition was not possible because of the contaminant arising from the $\text{Ge}(n, n'\gamma)$ reaction. Accordingly the 1397 keV state was assigned as 11^- .

The 1397 keV level is populated through the $E2$ cascade of energies 811.7, 907.6, 460.6, 532.0, 820.1 and 1075.8 keV reported by the earlier work. The coincidence analysis, R_{DCO} , $R(\theta)$ and the linear polarization measurement have been found to be in good agreement of the previously assigned quadrupole nature (Table 5.1) [90]. In addition, two new transitions of energy 1281.0 and 1464.0 keV (Figure 5.2 (b) and (c)) have been added to this sequence extending it to $I^\pi = 27^{(-)}$. The $R(\theta)$ and the linear polarization values for the 1281.0 keV (see Table 5.1) transition establishes it as $E2$. Due to the lack

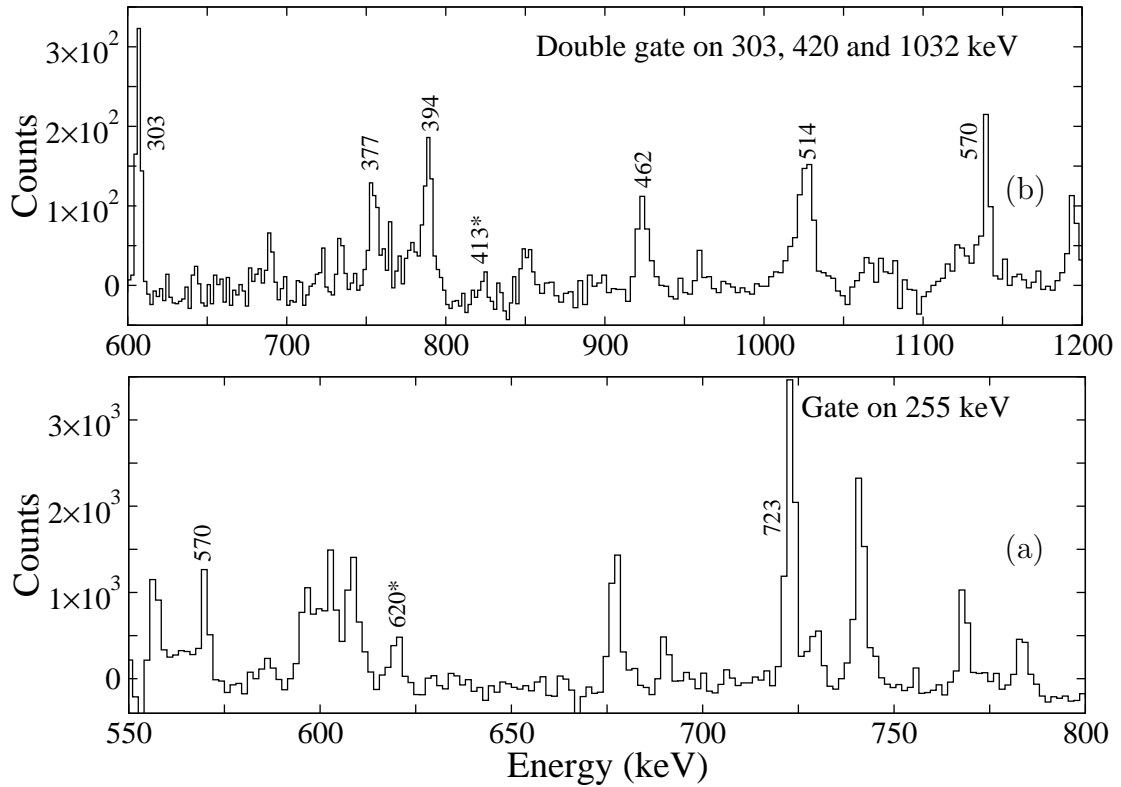


Figure 5.4: The coincidence spectra (a) and (b) show the presence of the newly found 620.3 and 413.0 keV transitions of DB I, respectively.

of statistics of the 1464.0 keV transition, only the $R(\theta)$ value 1.71(0.23) was extracted indicating it as a quadrupole transition. The γ transitions up to 15^- (3116.3 keV) state (811.7 and 907.6 keV) are similar in energy which is the signature of nuclear vibration. However, above $I^\pi = 15^-$, there exists a rotational like band structure consisting of transitions energies 532.0, 820.1, 1075.8, 1281.0 and 1464.0 keV. This structures has been labeled as QB I in Figure 5.1.

5.2.2 Dipole structures DB I and DB II

In the earlier work Piiparinen *et al.* had established [90] the positive parity energy states, which decay through $M1$ and $E2$ transitions. Based on the present analysis, the positive parity states have been rearranged to a bandlike structure which contains $M1$ with strong $E2$ cross-over transitions. This band has been labeled as DB I. In the present analysis,

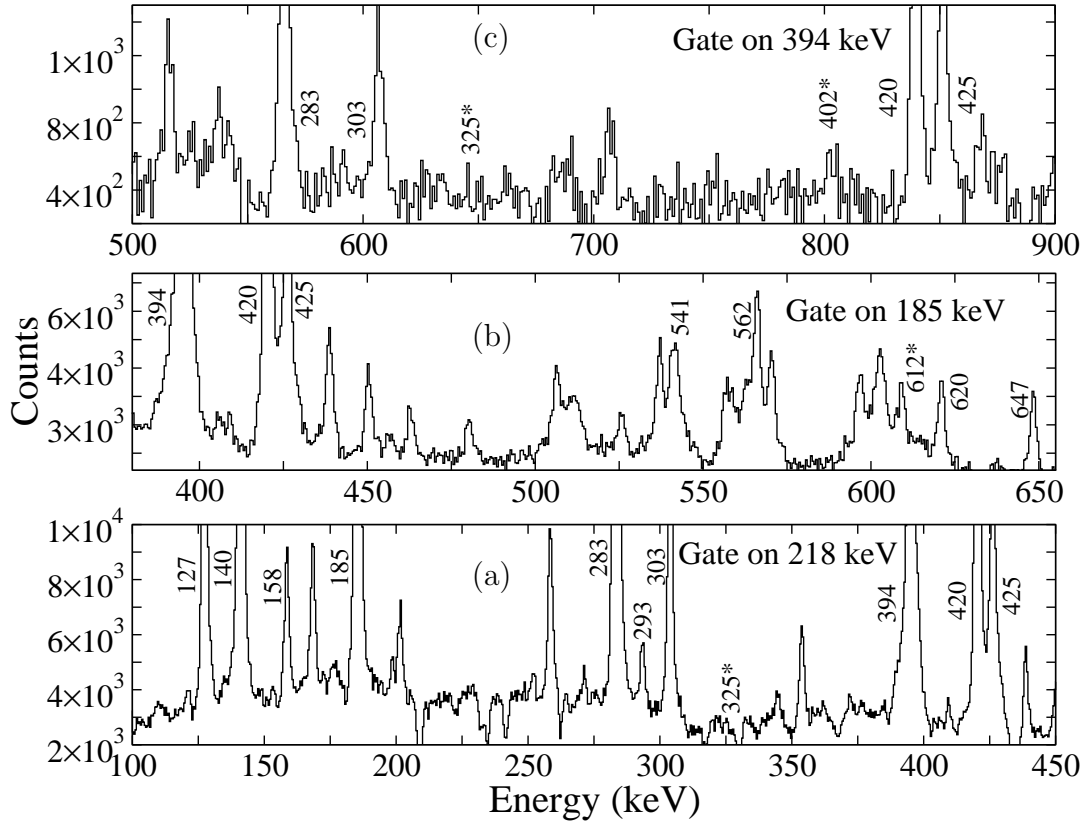


Figure 5.5: The coincidence spectra for the newly observed cross over transitions 325.0, 401.8 and 611.5 keV in DB II are shown in (a), (b) and (c), respectively.

two new γ transitions of energy 620.3 keV and 413.0 keV have been observed between $15^+ \rightarrow 13^+$ and $16^+ \rightarrow 14^+$ states (Figure 5.4 (a) and (b)), respectively. The measured $R(\theta)$ for 413.0 keV transition was found to be of 1.89(0.21) (~ 1.6 for pure quadrupole) which was in agreement with the $E2$ character.

The previous work on ^{142}Eu reported a negative parity dipole band like structure starting above the 13^- (2483 keV) state having transition energies 126.7, 140.4, 184.5, 218.4, 394.3, 425.4, 540.7 and 562.0 keV with regular energy spacing [90]. They have also reported three weak $E2$ cross over 820.2 keV ($19^- \rightarrow 17^-$), 967.0 keV ($20^- \rightarrow 18^-$) and 1103.0 keV ($21^- \rightarrow 19^-$). The absent or weak $E2$ transitions imply the weak deformation for the dipole sequence. In the present analysis, the negative parity dipole sequence has been confirmed from the coincidence analysis, R_{DCO} , $R(\theta)$ and the linear polarization measurements. This band-like structure has been assigned as DB II in the partial level structure (Figure 5.1). The present coincidence measurements confirmed three new weak

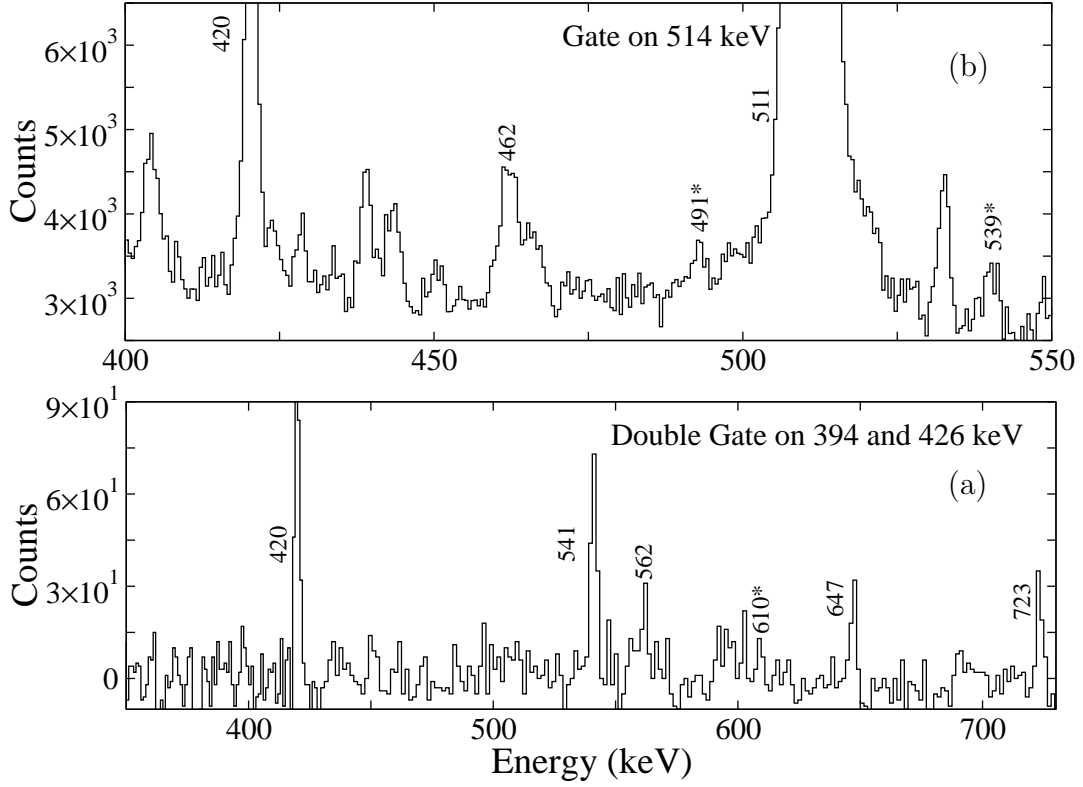


Figure 5.6: The coincidence spectra (a) and (b) show the presence of three new transitions of energies 491.0, 539.1 and 610.2 keV through which DB II decays to DB I.

cross-over transitions of 325.0, 401.8 and 611.5 keV (Figure 5.5) between the states $16^- \rightarrow 14^-$, $17^- \rightarrow 15^-$ and $18^- \rightarrow 16^-$, respectively. The $R(\theta)$ values for the 325.0 and 401.8 keV transitions were found to be of 1.30(21) and 1.43(22), respectively, which are in good agreement with the $E2$ nature of these cross-over transitions.

Piiparinen *et al.* had observed four $E1$ transitions of energy 1384.8, 941.6, 620.3, 646.6 keV through which the negative parity dipole band DB II decays into the positive parity dipole band DB I [90]. The measured R_{DCO} and R_θ values for the 1384.8, 941.6, 620.3, 646.6 keV transitions (Table 5.1) indicated their dipole nature. In the present study, three new inter-band γ transitions of energy 610.2 ($17^- \rightarrow 16^+$), 491.0 ($18^- \rightarrow 17^+$) and 539.1 ($19^- \rightarrow 18^+$) keV (shown in Figure 5.6), have been observed (Figure 5.1). The measured R_θ values of the 610.2, 491.0 and 539.1 keV transitions (Table 5.1) were in compliance with their dipole character. Out of these seven connecting transitions, the polarization measurement could be performed for four transitions (1384.8, 941.6,

620.3 and 646.6 keV). The measured positive polarization values of the 1384.8, 941.6, 620.3 and 646.6 keV transitions (see Table 5.1) indicated their electric dipole nature (polarization is positive for the electric transition). The polarization of the remaining three transitions (610.2 keV, 491.0 keV, and 539.1 keV) could not be evaluated due to the lack of statistics. Nevertheless, the $E1$ character of these transitions was confirmed through the definitive spin-parity assignments of in DB I and DB II.

Table 5.1: Energy (E_γ), Relative Intensity (I_γ), R_{DCO} , R_θ , linear polarization (P) and assignment of the gamma transitions in ^{142}Eu .

Energy (E_γ)	Intensity (I_γ)	J_i^π	J_f^π	DCO ratio ^a (R_{DCO})	Anisotropy ($R(\theta)$)	Polarization (P)	Assignment
83.6	978.8(264)	10^+	9^+	1.29(14)	1.18(5)		M1/E2
126.7	102.2(81)	14^-	13^-	0.88(13)	1.23(14)		M1/E2
140.4	166.8(69)	15^-	14^-	0.83(25)	1.08(6)		M1/E2
157.8	194.8(79)	15^+	14^+	0.76(17)	1.04(5)		M1/E2
184.5	180.8(96)	16^-	15^-	0.75(4)	0.84(0)	+0.01(15)	M1/E2
218.4	186.7(125)	17^-	16^-	0.66(4)	0.81(9)	+0.01(8)	M1/E2
254.6	145.5(39)	16^+	15^+	0.44(2)	0.83(10)	+0.02(6)	M1/E2
282.6	1000.0(125)	8^-	8^+	1.23(9)	1.73(4)		$\Delta I = 0$, (E1)
292.7	115.3(72)	9^-	8^+	0.55(4)	0.84(7)	+0.33(16)	E1
303.2	288.3(96)	12^+	11^+	0.52(4)	0.72(6)	-0.01(3)	M1/E2
325.0*	8.5(10)	16^-	14^-		1.30(21)		(E2)
377.2	49.2(77)	18^+	17^+	0.46(8)	0.54(3)	-0.02(8)	M1/E2
394.3	130.4(71)	18^-	17^-	0.52(4)	0.68(12)	+0.01(5)	M1/E2
401.8*	9.5(7)	17^-	15^-		1.43(22)		(E2)
413.0*	6.5(8)	16^+	14^+		1.89(21)		(E2)
419.6	555.4(167)	11^+	10^+	0.42(2)	0.66(4)	-0.01(3)	M1/E2
425.4	60.9(43)	19^-	18^-	0.53(6)	0.68(5)	-0.12(8)	M1/E2

Continued on next page

Table 5.1 – *Continued from previous page*

Energy (E_γ)	Intensity (I_γ)	J_i^π	J_f^π	DCO ratio ^a (R_{DCO})	Anisotropy ($R(\theta)$)	Polarization (P)	Assignment
460.6	143.2(97)	17 ⁻	15 ⁻	0.91(7)	1.38(9)	+0.41(17)	E2
461.7	59.1(45)	14 ⁺	13 ⁺		0.68(5)	-0.41(21)	M1
480.6	14.9(12)	14 ⁻	14 ⁺		1.31(16)	+0.28(24)	$\Delta I = 0$, E1
491.0*	7.2(9)	18 ⁻	17 ⁺		0.68(7)		(E1)
513.7	77.5(21)	17 ⁺	16 ⁺	0.47(5)	0.88(161)	+0.05(8)	M1/E2
532.0	116.2(65)	19 ⁻	17 ⁻	0.96(4)	1.43(21)	+0.31(14)	E2
539.1*	6.5(7)	19 ⁻	18 ⁺		0.59(0.06)		(E1)
540.7	29.1(15)	20 ⁻	19 ⁻	0.55(8)	0.97(45)	-0.01(4)	M1/E2
562.0	16.0(9)	21 ⁽⁻⁾	20 ⁻		1.08(19)		(M1/E2)
569.8	123.6(46)	13 ⁺	12 ⁺	0.69(4)	0.68(3)	-0.04(5)	M1/E2
585.0	8.7(11)	20 ⁺	19 ⁺		0.62(12)		(M1)
601.5	110.8(82)	11 ⁻	11 ⁺	0.99(7)	1.56(11)		$\Delta I = 0$, (E1)
610.2*	13.3(18)	17 ⁻	16 ⁺		0.73(5)		(E1)
611.5*	8.1(9)	18 ⁻	16 ⁻				(E2)
620.3	20.6(18)	15 ⁻	14 ⁺		0.68(6)	+0.22(15)	E1
620.3*	3.98(11)	15 ⁺	13 ⁺				(E2)
646.6	19.4(16)	16 ⁻	15 ⁺	0.87(9)	0.82(8)	+0.47(32)	E1
722.8	226.7(92)	12 ⁺	10 ⁺	1.02(9)	1.51(6)	+0.35(13)	E2
729.8	20.6(21)	21 ⁺	20 ⁺	0.50(8)	0.61(10)	-0.19(13)	M1
768.5	11.9(23)	17 ⁺	15 ⁺		1.64(17)	+0.62(48)	E2
783.3	12.9(11)	19 ⁺	18 ⁺		0.71(13)	-0.36(25)	M1
811.7	165.4(98)	13 ⁻	11 ⁻	1.14(6)	1.47(3)	+0.38(19)	E2
820.2	3.6(7)	19 ⁻	17 ⁻		2.03(22)		(E2)
820.1	68.1(61)	21 ⁻	19 ⁻	0.96(7)	1.44(13)	+0.25(16)	E2

Continued on next page

Table 5.1 – *Continued from previous page*

Energy (E_γ)	Intensity (I_γ)	J_i^π	J_f^π	DCO ratio ^a (R_{DCO})	Anisotropy ($R(\theta)$)	Polarization (P)	Assignment
873.0	9.0(11)	13 ⁺	11 ⁺		1.47(12)		(E2)
891.1	27.7(14)	18 ⁺	16 ⁺	1.03(13)	1.76(15)	+0.64(35)	E2
907.6	153.4(86)	15 ⁻	13 ⁻	0.89(7)	1.58(14)	+0.38(22)	E2
941.6	43.1(35)	14 ⁻	13 ⁺		0.51(08)	+0.34(23)	E1
967.0	2.4(6)	20 ⁻	18 ⁻		1.41(18)		(E2)
1021.1	24.6(23)	11 ⁻	10 ⁺	0.55(4)	0.53(3)	+0.68(32)	E1
1031.5	215.9(126)	14 ⁺	12 ⁺	1.07(7)	1.89(16)	+0.43(22)	E2
1075.8	36.2(28)	23 ⁻	21 ⁻	0.99(11)	1.72(15)	+0.62(41)	E2
1103.0	3.4(8)	20 ⁻	18 ⁻				(E2)
1104.5	23.9(25)	11 ⁻	9 ⁺	1.06(11)	1.77(13)		(M2)
1161.2	7.8(9)	19 ⁺	17 ⁺		1.53(21)	+0.33(21)	E2
1281.0*	19.6(21)	25 ⁻	23 ⁻		1.71(21)	+0.52(30)	E)
1314.8	4.2(8)	21 ⁺	19 ⁺		1.48(21)	+0.41(32)	E2
1368.6	21.3(16)	20 ⁺	18 ⁺	0.92(13)	1.46(10)	+0.71(47)	E2
1384.8	49.5(41)	13 ⁻	12 ⁺		0.66(4)	+0.47(21)	E1
1464.0*	4.1(12)	27 ⁽⁻⁾	25 ⁻		1.71(23)	+0.52(30)	(E2)

Uncertainty in γ ray energy is \pm (0.1-0.3) keV.

Intensities of γ rays are normalized to the 282.5 keV transition, with $I_\gamma = 1000.0$.

5.2.3 Lineshape Analysis

The level lifetimes of the ten levels (20⁺ to 11⁺) of DB I, eight levels (21⁽⁻⁾ to 14⁻) of DB II and three levels (25⁻ to 21⁻) of QB I in ^{142}Eu have been extracted in the present work using the Doppler Shift Attenuation Method (DSAM). The line shapes of the transitions at 65°, 90° and 140° have been fitted simultaneously with the help of the

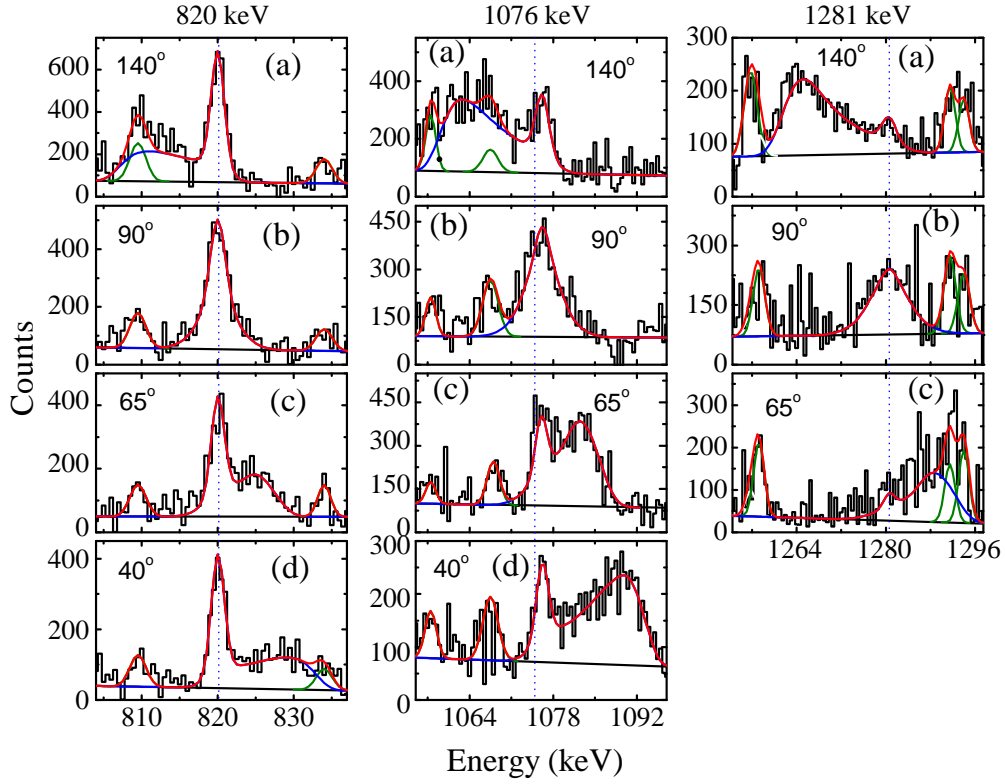


Figure 5.7: The observed spectra along with the fitted line shapes for the 820.1, 1075.6 and 1281.0 keV transitions of the quadrupole band of ^{142}Eu . The figures (a), (b), (c) and (d) are correspond to the shapes at 140° , 90° , 65° and 40° detectors. The spectrum for the 1281.0 keV transition at 40° is omitted since the peak merge with the background. The line shapes of the γ transitions, contaminant peaks and the total line shapes are represented by the blue, green and red curves, respectively. The vertical dotted line represents the stopped peak position for each transition.

LINESHAPE [95–97] package as per the procedure has been described in detail in chapter 3. The 1368.6 keV ($20^+ \rightarrow 18^+$), 562.0 keV ($21^{(-)} \rightarrow 20^-$) and 1281.0 keV ($25^- \rightarrow 23^-$) transitions are the highest transitions of the bands DB I, DB II and QBI, respectively, for which a clear Doppler shape has been observed in the experimental spectrum. The effective lifetimes of 0.81 ps, 0.46 ps and 0.45 ps have been extracted for the 20^+ , $21^{(-)}$ and 25^- states, respectively. For the measurement of the lifetime of 21^- state in QB I, the contribution of the two observed side feeding transitions of energies 443 and 800 keV (not shown in the present level scheme, Figure 5.1) were also taken into account. These side feeding transitions provide about 40% of the side feeding intensity and do not exhibit any lineshape in their experimental spectra. The 19^+ state of DB I feeds from 20^+ state, topmost level of the DB I and 21^+ state, the band-head of the dipole rotational

like band [90]. Therefore the change in structure occurs beyond 20^+ of DB I. Since, the lifetime of the 21^+ state could not be extracted, an upper limit of the life time of 19^+ state has been estimated. The effective lifetimes of 19^+ and 20^+ levels were used as the input parameters for obtaining the level lifetimes of the lower-lying states of the DB I. It is to be pointed out that in some cases the level of interest has been populated by more than one gamma transitions and the feeding states have a finite lifetime. For example, 19^- state of DB II, which decays via 425.4 keV transition, is populated by the 540.7 and 1103.0 keV transitions de-exciting the 20^- and $21^{(-)}$ levels of DB II, respectively. This information has been incorporated in the analysis by replacing the lifetime of the (top) feeding level by the intensity weighted average of the lifetimes of the two feeding states. For the 14^+ level of the DB I, several transitions have been found to feed the level. It was difficult to determine the proper branching ratios and side-feeding intensity parameters to the lineshape fitting of the transition depopulating this state. Therefore, an upper limit of the level lifetime for this state has been extracted. A similar situation arose for the 14^- and 15^- states in DB II and an upper limit of the level lifetime has been estimated for these states as well. The extracted level lifetimes and the corresponding reduced transition probabilities $B(E2)$, $B(M1)$ and $B(E1)$ values for the bands QB I, DB I and DB II are tabulated in Table 5.2, 5.3 and 5.4, respectively. The typical fits to the observed Doppler shapes for the transitions of the bands QB I, DB I and DB II in ^{142}Eu are shown in Figure 5.7, 5.8 and 5.9, respectively. The uncertainties in the lifetimes were determined from the nature of χ^2 in the vicinity of its minimum value. The systematic errors due to the uncertainty in the stopping power of the target/backing medium, which can be as large as 15%, have not been included in the quoted errors of the level lifetimes.

M. Piiparinen *et al.* had measured the lifetimes of the two levels (14^+ and 16^+) in DB I and five levels (14^- to 18^-) in DB II using the plunger technique [90]. The lifetimes were considerably larger (roughly by a factor of 2) than the present DSAM results, and the mismatch was well beyond the uncertainties of both measurements. It

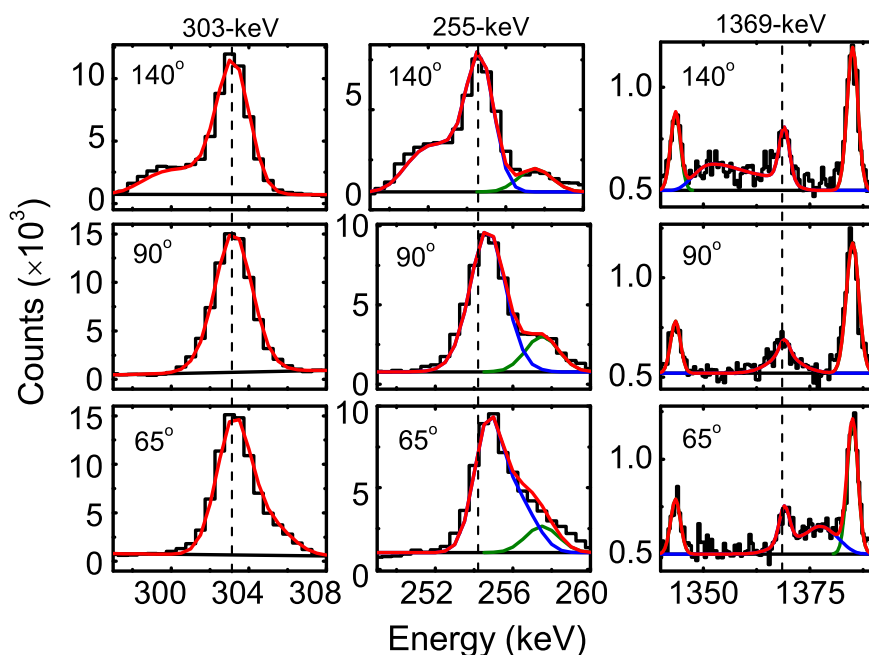


Figure 5.8: The observed line shapes and the fitted spectra for the (a) 303, (b) 255, and (c) 1369 keV γ transitions of the positive parity dipole band DB I in ^{142}Eu . The first, second and last rows correspond to the spectra at the 140° , 90° and 65° , respectively. The blue, olive and red curves represent the line shapes of the γ transition, contaminant peaks and total line shapes, respectively.

may be noted that the LINESHAPE analysis gives a lifetime limit for the highest level of the band, and uses it later as an input parameter when calculating the lower levels in the band. This implies that the uncertainty for the highest level gets carried through each lower level that is being analyzed and adds to the uncertainty of the measurement. This may lead to the discrepancy between the lifetimes obtained from the present DSAM measurements and the previous plunger techniques. In addition, the deviation may also arise due to the presence of the newly observed cross-over $E2$ transitions and the side-feeding intensities of the levels of interest. However, in both the cases, the measured lifetime and corresponding transition probabilities ($B(M1)$, $B(E1)$ and $B(E2)$ values) and their variations with spin exhibit the same characteristic trend, leading to the same interpretation of the bands and suggested octupole correlations, detailed in the next sections.

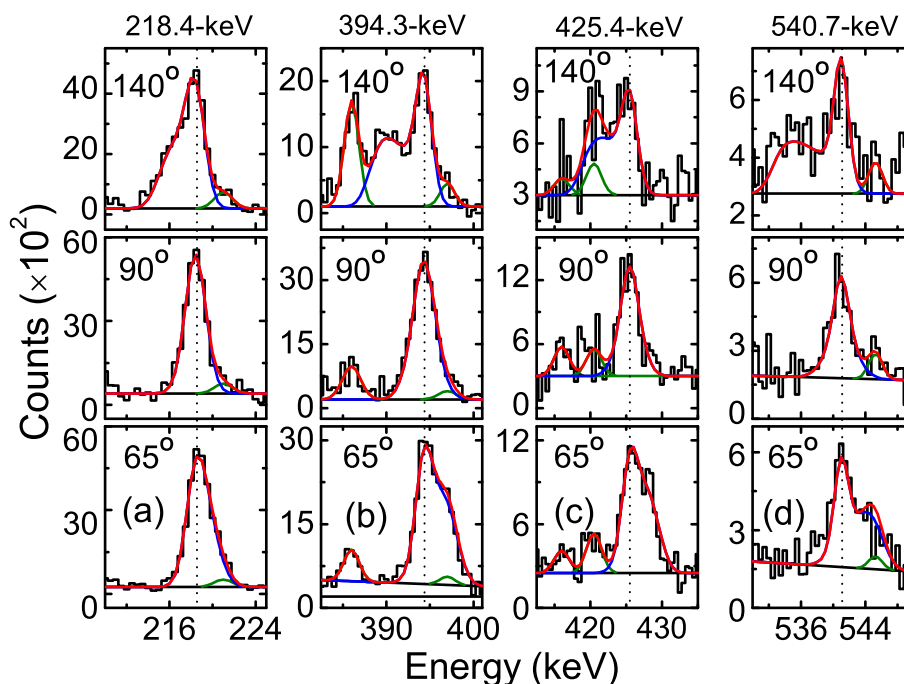


Figure 5.9: The observed line shapes and the fitted spectra for the (a) 218.4, (b) 394.3, (c) 425.4, and (d) 540.7 keV γ transitions of the negative parity dipole band DB II in ^{142}Eu . The first, second and last rows correspond to the spectra at the 140° , 90° and 65° , respectively. The blue, olive and red curves represent the line shapes of the γ transition, contaminant peaks and total line shapes, respectively.

5.3 Discussions

As far as the mass region $A \sim 140$ is concerned, the magnetic rotational bands have been observed in $^{139,142}\text{Sm}$, $^{141,143}\text{Eu}$ and ^{142}Gd [8, 32, 33, 42, 43] nuclei. The Eu, Gd isotope shows multiple MR bands in their excitation spectra. To reproduce the observed $B(M1)$ values of these bands, different model calculations have been performed and specific configuration have been assigned to these bands. Except for ^{143}Eu , it was observed that the MR bands generated with identical proton configuration and differing only in neutron number in $h_{11/2}$ orbital. However, proton aligned band has been recently observed in ^{143}Eu [43].

The odd-odd ^{142}Eu ($Z = 63$, $N = 79$) is weakly deformed with respect to the semi-magic nucleus ^{146}Gd ($Z = 64$, $N = 82$). The protons particles can be easily excited to the $h_{11/2}$ orbital across the subshell closure, leading to the observation of the MR and

Table 5.2: The measured level lifetimes, the corresponding $B(E2)$ transition rates, the dynamic moment of inertia $J^{(2)}$ and the ratio of $J^{(2)}/B(E2)$ values for the quadrupole transitions in ^{142}Eu .

J_i^π [\hbar]	E_γ [keV]	τ^a [ps]	τ^b [ps]	$B(E2)$ [e^2b^2]	$J^{(2)}$ [$\hbar^2\text{MeV}^{-1}$]	$J^{(2)}/B(E2)$ [$\hbar^2\text{MeV}^{-1}/e^2b^2$]
19^-	532.0	8.30(12)		0.23_{-3}^{+3}	15.40	66.95_{-873}^{+873}
21^-	820.1	<2	1.23_{-16}^{+21}	0.18_{-2}^{+3}	16.73	92.94_{-1033}^{+1549}
23^-	1075.8		0.46_{-7}^{+9}	0.12_{-2}^{+2}	18.98	158.17_{-2636}^{+2636}
25^-	1281.0		<0.45	>0.05	20.72	<414.7

^aThe level lifetimes from ref. [90].

^bPresent measurements.

AMR band in this mass region.

5.3.1 Evidence of AMR band in ^{142}Eu

The measured $B(E2)$ values show a monotonically decreasing behavior with the increasing angular momentum in the QB I, as seen from Table 5.2. Besides the $J^2/B(E2)$ ratio (shown in Table. 5.2) is found to be an order of magnitude larger than those for a collective rotor and increase rapidly with a spin, which eliminates the possibility of deformed band having a smooth termination (Figure 5.10 (a)). The trend of the $B(E2)$ values and the $J^2/B(E2)$ ratios have the definite experimental signatures of the AMR phenomenon [38], which identify this band as the only known AMR band in an odd-odd nucleus.

The 8^- isomeric ground state of ^{142}Eu has the configuration $\pi d_{5/2}^{-1} \otimes \nu h_{11/2}^{-1}$. In the previous works [90,124] the excited states up to $I^\pi = 11^+$ (797.0 keV) were interpreted in the shell model framework with the configuration $\pi h_{11/2}^1 \otimes \nu h_{11/2}^{-1}$. The 1397.0 keV state (11^-) is expected to have a configuration $\pi g_{7/2}^{-1} \otimes \nu h_{11/2}^{-3}$ from the alignment plot (Figure 5.11). The anti-symmetric state with three neutron holes in the $h_{11/2}$ orbital can produce a spin 15/2 which then coupled with a proton hole in the $g_{7/2}$ orbital, can generate a state of spin-parity 11^- . The configuration $\pi g_{7/2}^{-1} \otimes \nu h_{11/2}^{-3}$ can generate states up to $I^\pi =$

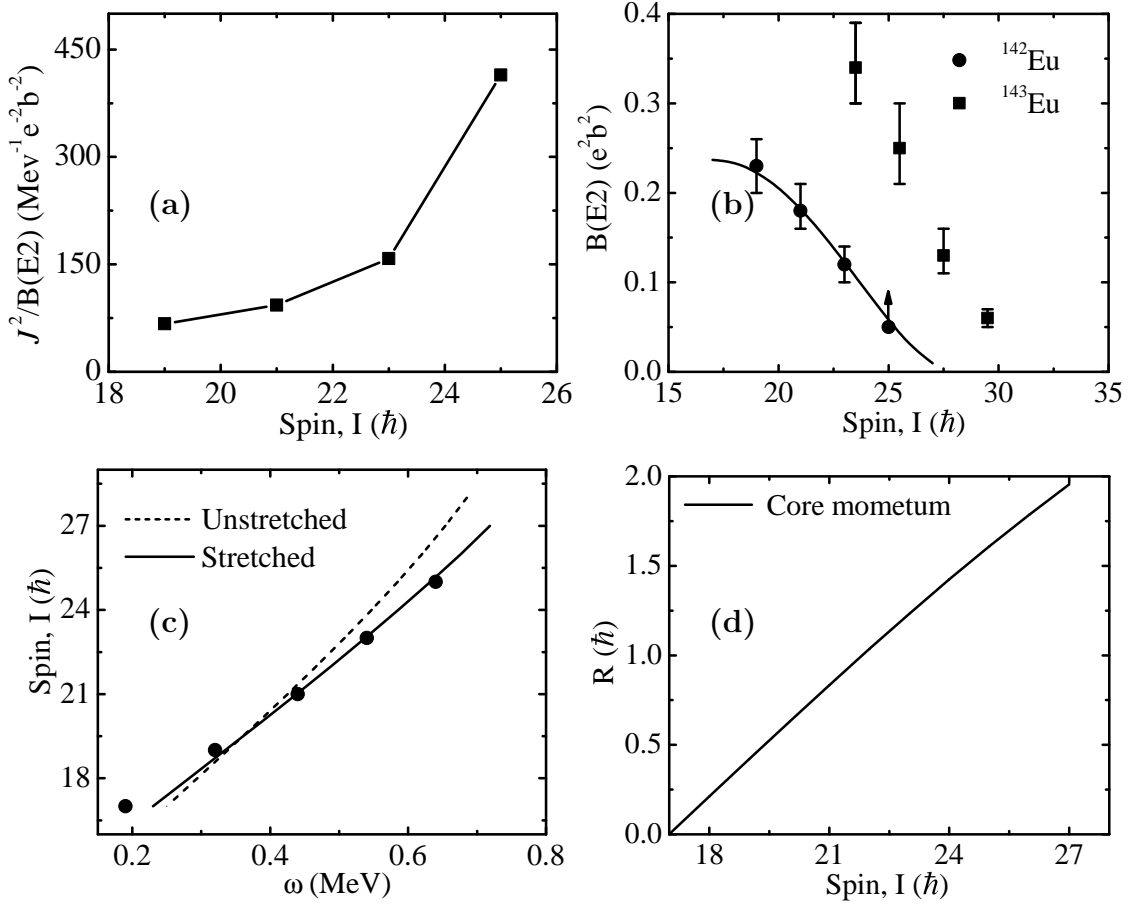


Figure 5.10: (a) $J^2/B(E2)$ vs. spin ($I(\hbar)$), (b) $B(E2)$ values with spin ($I(\hbar)$) and (c) $I(\hbar)$ against rotational frequency (ω) plots for the quadrupole band in ^{142}Eu . The solid and dashed line in (c) represents the theoretical SPRM calculation for unstretched and stretched conditions, respectively. The variation of R is shown in the panel (d). The parameters used for this calculation are $V_{\pi\pi} = 0.2$ and $V_{\pi\nu} = 1.7\text{-MeV}$ [42], $j_{\pi}^1 = j_{\pi}^2 = 4.5$ (unstretched), $j_{\nu} = 17$, $n = 8$ and $a = 3.78$ and $eQ_{eff} = 1.26$ eb (calculated as in ref. [1]). The parameters have the same meaning as in refs. [38–42]. The upward arrow in (b) represents the lower limit of the $B(E2)$ value for the 25^- state of the quadrupole structure. The $B(E2)$ values for the quadrupole band I in ^{143}Eu [42] are also shown (solid squares) (see text for details).

17^- which is the band head of the AMR band. A configuration of $\pi g_{7/2}^{-1} \nu h_{11/2}^{-3} \otimes \pi h_{11/2}^2$ is proposed for this band, which well reproduces the band head spin (17^-) with a negligible amount of angular momentum contribution from the weakly deformed core. For oblate deformation, three neutrons holes are rotationally aligned along with the one proton hole in $(d_{5/2}/g_{7/2})$ orbital. On the other hand, proton particles in the time-reversed $h_{11/2}$ orbits produce two deformation aligned angular momentum vectors which are anti-aligned to each other and perpendicular to the total angular momentum of the rotation-aligned holes. Thus, this configuration leads to a conjugate symmetric double shears

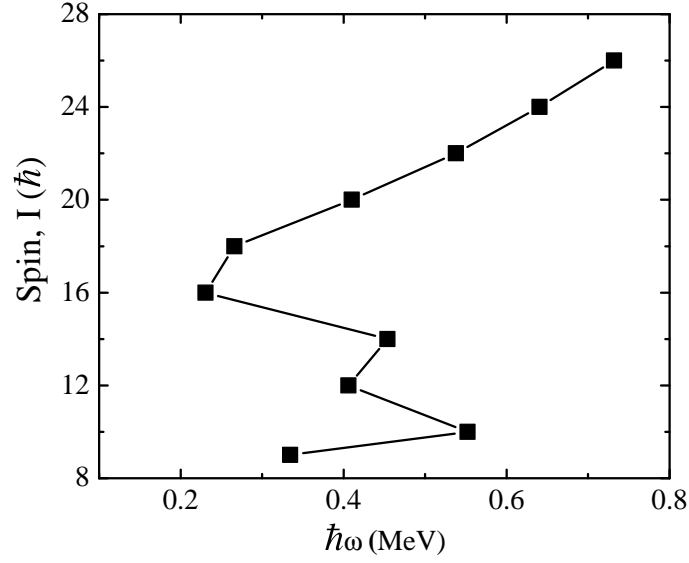


Figure 5.11: The variation of the total angular momentum (I) with rotational frequency (ω) for QB I of ^{142}Eu .

structure and generates the higher angular momentum states through the simultaneous closing of the structure of the double shear, leading to an AMR band.

To explore the underlying theoretical structure of the AMR band in ^{142}Eu with the configuration suggested above, an analysis has been carried out using the SPRM model [7, 40]. The $B(E2)$ rates were calculated using,

$$B(E2; I \rightarrow I - 2) = \frac{15}{32\pi} (eQ_{eff})^2 \sin^4 \theta \quad (5.1)$$

$$= \frac{15}{32\pi} (eQ_{eff})^2 \left[1 - \left(\frac{\mathbf{J} - \mathbf{j}_\nu}{2\mathbf{j}_\pi} \right)^2 \right]^2 \quad (5.2)$$

where \mathbf{j}_π any one of the proton angular momentum vectors which is deformation aligned and \mathbf{j}_ν is the total rotational aligned hole angular momentum, θ is the angle between \mathbf{j}_π and \mathbf{j}_ν . The value of the eQ_{eff} can be estimated from the formula given in ref. [1].

For $\pi g_{7/2}^{-1} \nu h_{11/2}^{-3} \otimes \pi h_{11/2}^2$ configuration, $j_\pi = 5.5\hbar$ assuming the stretched configuration

of the angular momentum vectors. However, for the stretched configuration with $j_\pi = 5.5\hbar$ and $j_\nu = 17\hbar$, the SPRM calculation could not reproduce self-consistently both the $I(\omega)$ and $B(E2)$ as depicted in Figure 5.10 (b) and (c). But, the unstretched configuration with $j_\pi = 4.5\hbar$ is in good agreement with the experimental values of $I(\omega)$ and $B(E2)$ with increasing angular momentum. Such unstretched configuration has been assumed in the semiclassical calculations for the other nuclei in this mass region [8, 32, 33, 42]. The maximum attainable angular momentum for the proposed configuration with unstretched angular momenta is 25^- (because of Pauli blocking). But the maximum observed state of QB I is $27^{(-)}$. The SPRM calculations show that at the band-head there is no contribution to the angular momentum from the weakly deformed core. But, as the excitation energy increases the core rotation starts contributing and reaches $\sim 2\hbar$ at the top of the band (see Figure 5.10 (d)). This increase in the core contribution results in the slow falling trend for the $B(E2)$ rates in comparison with the fully stretched configuration of ^{143}Eu as shown in Figure 5.10 (b) [42]. The interplay between the collective rotation and the shears mechanism (AMR) was first observed in the ^{110}Cd [40] and such an increase in the core contribution along the shears band is more commonly observed in the magnetic rotational band [1, 8, 43].

5.3.2 Octupole correlation between two shears bands in ^{142}Eu

The measured reduced transition rates ($B(M1)$ and $B(E2)$) decrease (Table 5.3 and 5.4) with increasing spin for both DB I and DB II. This prompted us to examine the behavior of the experimental routhian (angular momentum vs. rotational frequency) for the DB I and DB II in the framework of the tilted axis cranking covariant density functional theory (TAC-CDFT) formalism [12–17].

Table 5.3: The measured transition energies, the branching ratios (Br), the level lifetimes, the $B(M1)$ (considering conversion coefficients and mixing ratio of the transitions of interest) values of the DB I in ^{142}Eu .

J_i^π [\hbar]	E_γ [keV]	Br [%]	τ [ps]	$B(\sigma\lambda)$ [W.u.]
11 ⁺	419.6 (M1)	100(4)	0.79_{-8}^{+8}	0.55_{-6}^{+6}
12 ⁺	303.2 (M1) 722.8 (E2)	56(3) 44(3)	0.75_{-13}^{+10}	0.80_{-14}^{+11} 55.14_{-956}^{+735}
13 ⁺	569.8 (M1) 873.0 (E2)	90(11) 10(2)	0.40_{-16}^{+17}	0.38_{-15}^{+16} 9.14_{-366}^{+388}
14 ⁺	461.7 (M1) 1031.5 (E2)	16(2) 61(6)	0.90↓	0.06↑ 10.76↑
15 ⁺	157.8 (M1) 620.3 (E2)	98(10) 2(1)	3.43_{-49}^{+56}	1.50_{-21}^{+24} 1.18_{-17}^{+19}
16 ⁺	254.6 (M1) 413.0 (E2)	98(10) 1(1)	1.46_{-19}^{+22}	1.11_{-15}^{+17} 10.57_{-138}^{+159}
17 ⁺	513.7 (M1) 768.5 (E2)	89(7) 11(3)	0.46_{-5}^{+6}	0.45_{-5}^{+6} 16.54_{-180}^{+216}
18 ⁺	377.2 (M1) 891.1 (E2)	64(7) 36(5)	1.24_{-28}^{+32}	0.30_{-7}^{+8} 9.58_{-216}^{+247}
19 ⁺	783.4 (M1) 1161.2 (E2)	62(10) 38(7)	0.74↓	0.06↑ 4.51↑
20 ⁺	585.0 (M1) 1368.6 (E2)	21(6) 79(12)	0.81↓	0.04↑ 3.77↑

Table 5.4: The measured transition energies, the branching ratios (Br), the level lifetimes, the $B(M1)$ (considering conversion coefficients and mixing ratio of the transitions of interest), the $B(E1)$ and the $B(E2)$ values, the electric quadrupole and the dipole moments (Q_0 and D_0) of the DB II in ^{142}Eu .

J_i^π [\hbar]	E_γ [keV]	Br [%]	τ [ps]	$B(\sigma\lambda)$ [W.u.]	Moment
14^-	126.7 (M1)	49(6)	4.2↓	0.88↑	2.13 ^c ↑
	941.6 (E1)	21(3)		0.21×10^{-4} ↑	
15^-	140.4 (M1)	89(8)	3.1↓	1.84↑	3.28 ^c ↑
	620.3 (E1)	11(2)		0.53×10^{-4} ↑	
16^-	184.5 (M1)	89(8)	1.36^{+22}_{-24}	2.43^{+39}_{-43}	3.41^{+55b}_{-60}
	325.0 (E2)	1(1)		37.60^{+608}_{-664}	
	646.6 (E1)	10(2)		$0.98^{+16}_{-17} \times 10^{-4}$	
17^-	218.4 (M1)	91(9)	1.18^{+17}_{-18}	1.95^{+28}_{-30}	$2.92^{+42}_{-045}{}^b$
	401.8 (E2)	2(1)		30.01^{+432}_{-458}	
	610.2 (E1)	7(2)		$0.94^{+14}_{-14} \times 10^{-4}$	
18^-	394.3 (M1)	90(9)	0.89^{+15}_{-13}	0.53^{+9}_{-8}	1.82^{+31b}_{-27}
	611.5 (E2)	5(1)		12.18^{+205}_{-178}	
	491.0 (E1)	5(1)		$1.70^{+29}_{-25} \times 10^{-4}$	
19^-	425.4 (M1)	86(10)	1.17^{+25}_{-17}	0.30^{+6}_{-4}	0.81^{+17b}_{-12}
	820.2 (E2)	6(1)		2.56^{+55}_{-37}	
	539.1 (E1)	8(2)		$1.57^{+34}_{-23} \times 10^{-4}$	
20^-	540.7 (M1)	92(24)	1.10^{+17}_{-15}	0.17^{+3}_{-2}	0.62^{+10b}_{-9}
	967.0 (E2)	8(3)		1.59^{+25}_{-22}	
$21^{(-)}$	562.0 (M1)	80(11)	0.46↓	0.31↑	1.07 ^b ↑
	1103.0 (E2)	20(4)		4.94↑	

^aElectric dipole moment (D_0) in $10^{-2}efm$.

^bElectric quadrupole moment (Q_0) in eb.

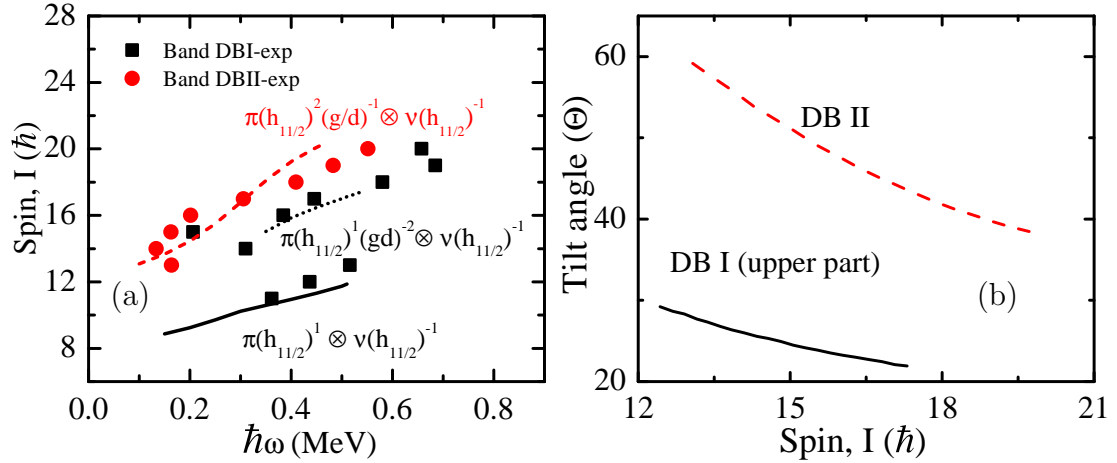


Figure 5.12: (a) Total angular momenta calculated by TAC-CDFT with and without pairing correlations and represented by solid and dashed lines, respectively, for DB I and DB II in ^{142}Eu as a function of rotational frequency (ω), in comparison with the data. In (b) variation of tilt angle with spin has been shown.

5.3.2.1 TAC-CDFT calculations

In the framework of TAC-CDFT formalism [12–17], the comparison with the data is shown in Figure 5.12 (a). For DB I, the calculated results based on $\pi h_{11/2}^1 \otimes \nu h_{11/2}^{-1}$ configuration, similar to that assigned by Piiparinen *et al.* [90], with pairing correlation before backbending and $\pi h_{11/2}^1 (g_{7/2}/d_{5/2})^{-2} \otimes \nu h_{11/2}^{-1}$ configuration without pairing after backbending are in good agreement with the data. Similarly, for DB II, the experimental results are well reproduced with $\pi h_{11/2}^2 (g_{7/2}/d_{5/2})^{-1} \otimes \nu h_{11/2}^{-1}$ configuration. These calculations show that the tilt angle for DB I and DB II are $\sim 25^\circ$ and $\sim 51^\circ$, respectively at $15\hbar$ (Figure 5.12 (b)). This indicates a substantially larger contribution of the collective rotation in DB I as compared to DB II, which in turn, might explain the origin of the energy staggering observed in DB I. The smaller $B(M1)$ rates of DB I than DB II (as tabulated in Table 5.3 and 5.4) also indicates a smaller tilt angle for DB I.

5.3.2.2 Dönau Model Calculations

To reproduce the slow falling trend in measured reduced transitions probabilities, $B(M1)$ and $B(E2)$ values for the DB I and DB II, the numerical values for the $B(M1)$ rates

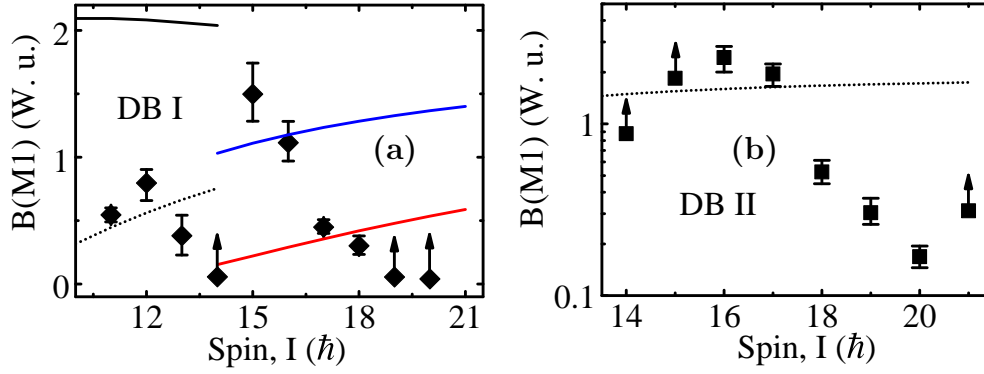


Figure 5.13: Comparison of the experimental $B(M1)$ values as a function of spin for the DB I and DB II in ^{142}Eu with the theoretical Dönau model calculation (panels (a) and (b)) [65]: (a) The solid black lines represent the calculated $B(M1)$ values before the back bending of DB I. The solid red and blue represents calculated values of $B(M1)$ after the back bending of DB I assuming the proton hole pair occupancy in the nearly degenerate $d_{5/2}$ and $g_{7/2}$ orbitals, respectively. A better fit to the $B(M1)$ values of the band DB I before back bending can be obtained where the two quasi-particles are treated as a common structure assuming the “common” two quasiparticle g factor (g^{2QP}), alignment (i^{2QP}) and projection along the symmetry axis (K^{2QP}) as $+1.35$, $4\hbar$ and $5\hbar$, respectively [67] and represented by the dotted line in (a).

were calculated through the geometric Dönau model have been compared with the experimental values for DB I and DB II in Figure 5.13 (a) and (b). The parameters used for the rotational aligned (RAL) and deformed aligned (DAL) configurations are tabulated in Table 5.5. In this geometrical model calculations rotation around the principal axis (PAR) has been assumed. These calculations clearly failed to reproduce the observed falling trend thereby indicating that both the dipole bands may originate due to the shears mechanism. Such behaviour has been observed in a number of nuclei in this mass region [8, 9, 32–34, 43].

Table 5.5: The parameters used in the calculation of $B(M1)$ transition rates using Dönau geometric model [35, 65]. DAL and RAL correspond to the deformation aligned and rotational aligned counterpart of the quasiparticles, respectively.

Band	K	DAL configuration	$i_x^1(\hbar)$	$g^{(1)}$ [66]	RAL configuration	$i_x^2(\hbar)$	$g^{(2)}$ [66]
DB I ^a	6	$\pi[h_{(11/2)}]_{\frac{11}{2}}^{-}$	$\frac{1}{2}$	+1.21	$\nu[h_{(11/2)}]_{\frac{1}{2}}^{-}$	5.5	-0.21
DB I ^b	7	$\pi[h_{(11/2)}]_{\frac{11}{2}}^{-}$	0.5	+1.21	$\nu[h_{(11/2)}]_{\frac{1}{2}}^{-} \otimes \pi[d_{(5/2)}]_{\frac{3}{2}}^{3+} \otimes \pi[d_{(5/2)}]_{\frac{1}{2}}^{1+}$	9.5	+1.062
DB I ^b	7	$\pi[h_{(11/2)}]_{\frac{11}{2}}^{-}$	0.5	+1.21	$\nu[h_{(11/2)}]_{\frac{1}{2}}^{-} \otimes \pi[g_{(7/2)}]_{\frac{3}{2}}^{3+} \otimes \pi[g_{(7/2)}]_{\frac{1}{2}}^{1+}$	11.5	+0.534
DB II	7	$\pi[h_{(11/2)}]_{\frac{11}{2}}^{-} \otimes \pi[h_{(11/2)}]_{\frac{9}{2}}^{-}$	2.0	+1.21	$\nu[h_{(11/2)}]_{\frac{1}{2}}^{-} \otimes \pi[g_{(7/2)}]_{\frac{1}{2}}^{1+}$	9.0	+0.255

^aConfiguration before band crossing.

^bConfiguration after band crossing.

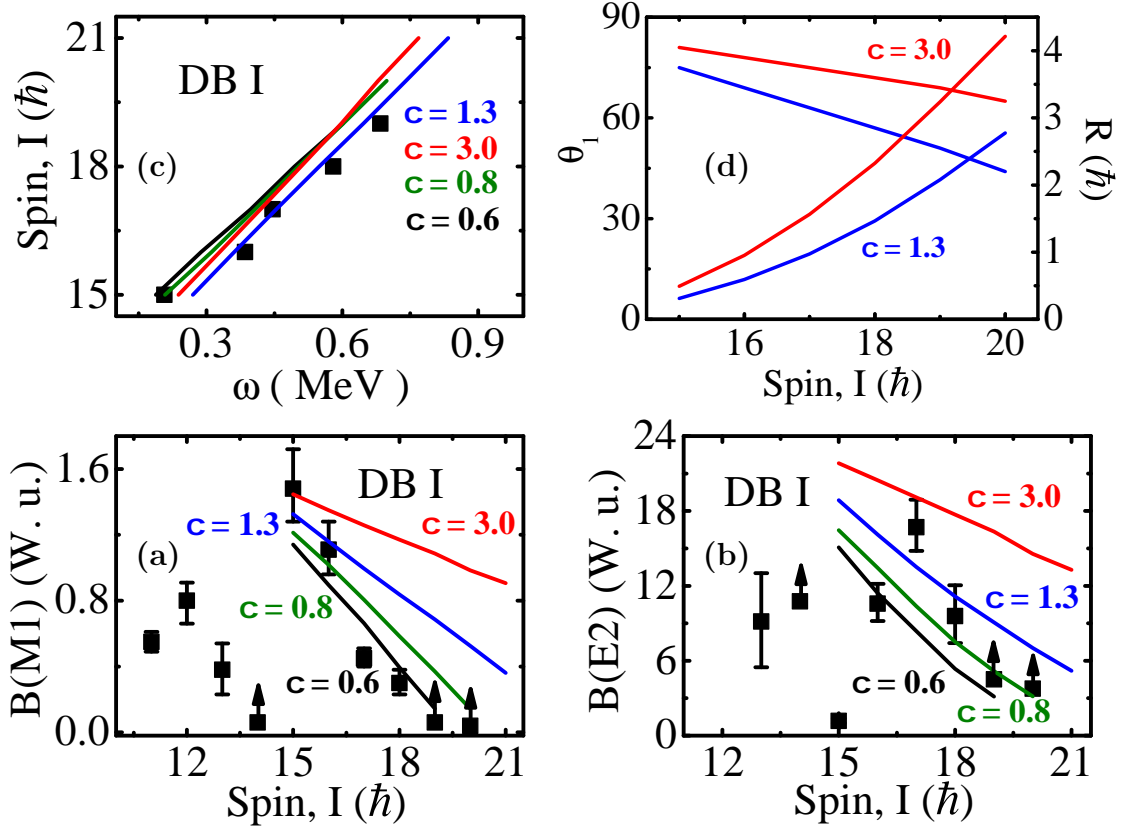


Figure 5.14: Comparison of the observed $B(M1)$, $B(E2)$, and ω values as function of spin for the DB I in ^{142}Eu with the modified SPAC model (panels (a), (b) and (c)) [125] calculations. The parameters used in the modified SPAC calculations are $j_1 = 4.5\hbar$, $j_2 = 11.5\hbar$, $g_1 = 1.21$, $g_2 = -0.01$, $Q_{eff} = 1.5$ and $Q_{col} = 0.50$ [8]. The modified SPAC model calculations are represented by the solid red ($\chi = 3.0$), blue ($\chi = 1.3$), olive ($\chi = 0.8$) and black ($\chi = 0.6$) black lines. (d) The variation of core angular momentum (R) and shears angle (θ_1) as a function of spin which indicates the slow rate of closing of the shears angle (θ_1) and rapid increase in core angular momentum (R) for $\chi \sim 3.0$ and 1.3.

5.3.2.3 SPAC Model Calculation

The quantitative measures of the contribution of core rotational angular momentum in the magnetic rotational (MR) bands have been investigated by incorporating a dimensional parameter (χ) in the shears mechanism with principal axis cranking model (SPAC) calculations [125]. The modified SPAC model calculations have been performed for the oblate deformed shape associated with the configuration $\pi h_{11/2}^1 (g_{7/2}/d_{5/2})^{-2} \otimes \nu h_{11/2}^{-1}$ assigned to the upper part of DB I. The $B(M1)$ and $B(E2)$ values could be calculated assuming the unstretched condition of angular momentum $j_1 = 4.5\hbar$ and $j_2 = 11.5\hbar$ generated from the particle and hole sectors, respectively, for different values of

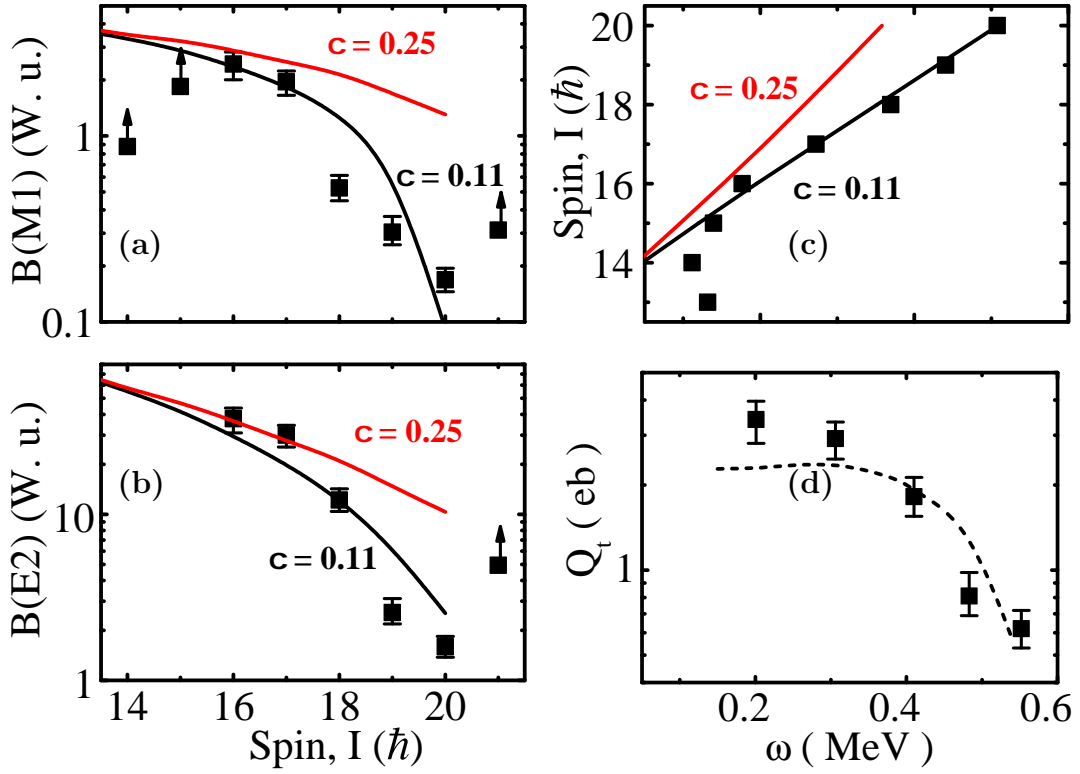


Figure 5.15: (a) and (b) show the comparison of the experimental $B(M1)$ and $B(E2)$ values for the DB II in ^{142}Eu with the SPAC (solid line) calculations, respectively. (c) The observed variation of spin (I) as a function of the rotational frequency (ω) is compared with the SPAC calculations. Experimental Q_t values of DB II are compared with the TRS calculations [25, 63] (dashed line) in panel (d). The parameters used in the SPAC calculations are $j_1 = 10\hbar$, $j_2 = 8\hbar$, $g_1 = -0.014$, $g_2 = 1.21$, $J = 3.85 \hbar^2/\text{MeV}$ and $v_2 = 0.93 \text{ MeV}$, $Q_{eff} = 7.10$ and $Q_{col} = 0.50$ [8], which corresponds to $\chi \sim 0.11$. The solid black and red lines represent the SPAC calculation with $\chi \sim 0.11$ and 0.25 , respectively.

χ as depicted in Figures 5.14 (a) and (b). These figures show that the lower spin ($I \sim 15\hbar$) states are generated for higher value of χ (~ 3.0) whereas small values of χ (~ 0.6) are responsible for the higher angular momentum states after the back bending of DB I. This indicates that the angular momentum generated after the band crossing of DB I has large core contribution ($\sim 75\%$) at lower spin ($\sim 15\hbar$) which decreases smoothly along the band ($\sim 38\%$ at $I \sim 19\hbar$). Thus, it may be inferred that the states after the back bending in DB I are generated due to the interplay of the PAR with the TAR.

The experimental routhian and the observed transition rates in DB II have also been well reproduced in the SPAC model calculation using $\pi h_{11/2}^2 (g_{7/2}/d_{5/2})^{-1} \otimes \nu h_{11/2}^{-1}$ configuration. This comparison is shown in Figure 5.15. For DB II, the observed transitions

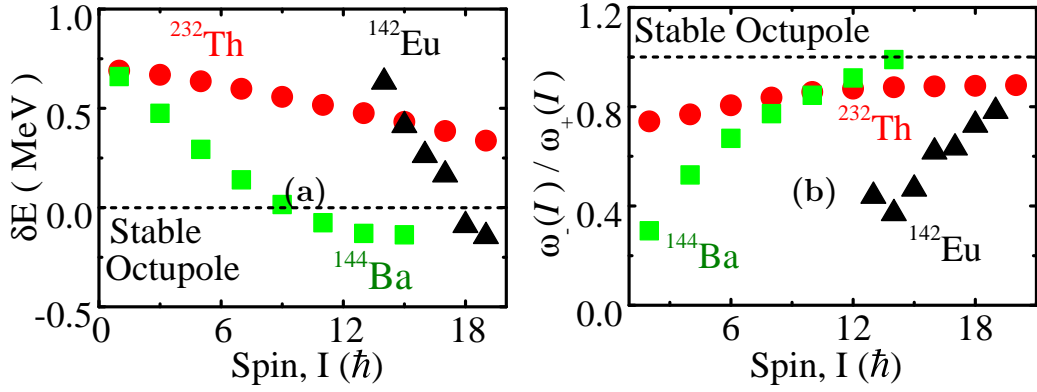


Figure 5.16: The variation of $\delta E, \omega^-(I)/\omega^+(I)$ ratio as a function of spin (I) for the bands in ^{142}Eu , ^{117}Xe , ^{232}Th and ^{144}Ba in (a) and (b).

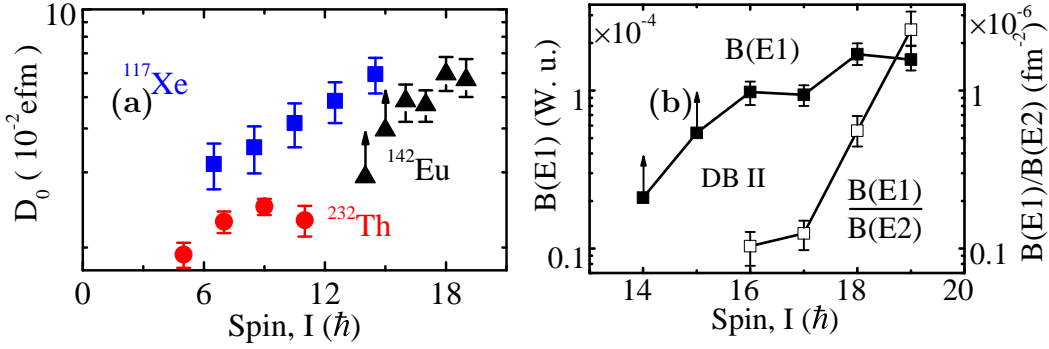


Figure 5.17: The variation of the dipole moment D_0 , the $B(E1)$ rates and $B(E1)/B(E2)$ ratio against spin (I) for the two opposite parity bands in ^{142}Eu , ^{117}Xe , ^{232}Th in (a), and (b), respectively.

rates are best reproduced with a very small collective contribution ($\sim 10\%$), which is also evident from the very weak cross-over $E2$ transitions of DB II. Thus, it may be concluded that both the four quasi-particle bands (DB I after back-bending and DB II) originate due to the interplay between tilted axis rotation (TAR) and principle axis rotation (PAR) and DB II has smaller collective contribution.

5.3.2.4 Octupole Correlation between DB I and DB II

The DB II decays to the DB I through the strong $E1$ transitions with large $B(E1)$ ($\sim 10^{-4} W. u.$) and $B(E1)/B(E2)$ transition rates (Table 5.6). Such large transition rates are comparable to the values observed in the opposite parity (octupole) bands of $^{124,125}\text{Ba}$ [126], ^{117}Xe [127] and ^{124}Cs [121]. Thus, the bands DB I and DB II dif-

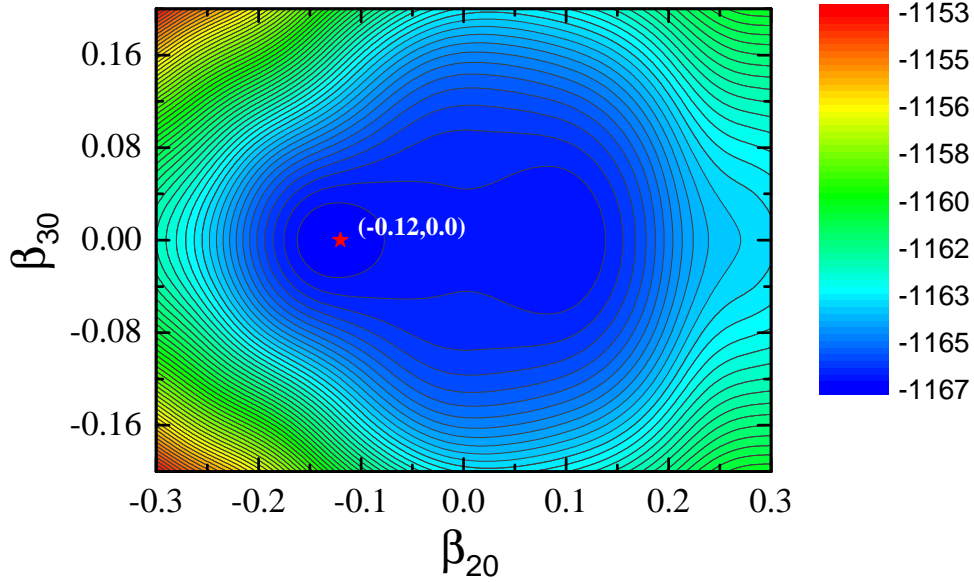
fering by $3\hbar$ at the band-head spin and connected through $E1$ transitions indicate a reflection asymmetric shape. The shape transition from reflection symmetric at low spin to reflection asymmetric at medium spin induced by rotation is plausible in ^{142}Eu . Such symmetry breaking induced by rotation has been previously observed in ^{148}Sm and ^{146}Nd [128] and supported by theoretical consideration [129].

To get a better understanding, the energy displacement $\delta E(I)$ and the rotational frequency ratio $\omega_-(I)/\omega_+(I)$ [36] have been calculated. These values steadily approach the stable octupole limit with increasing spin and overlap with the observed octupole deformed bands in ^{144}Ba [80] and vis-à-vis to the small variation of the octupole correlated bands in ^{232}Th [79] (Figure 5.16 (a) and (b)). Magnitude of the extracted intrinsic dipole moment D_0 from the measured $B(E1)$ values exhibit a slow increase from $4.30_{-0.76}^{+0.70} \times 10^{-2} \text{efm}$ at $I^\pi = 16^-$ to $5.51_{-0.80}^{+0.93} \times 10^{-2} \text{efm}$ at $I^\pi = 19^-$ in the DB II, which is similar to the octupole correlated bands in ^{117}Xe and ^{232}Th (Figure 5.17 (a)). This slow variation of D_0 is in contrast with the sharp increase of the $B(E1)/B(E2)$ rate (Figure 5.17 (b)) which arises due to the rapid falling of the Q_t values with spin due to TAR (Figure 5.15 (d)). This indicates that a dynamical octupole correlation between the $d_{5/2}$ and $h_{11/2}$ proton orbitals near the Fermi surface may exist in ^{142}Eu [36] and is the first experimental evidence of such correlation between two shears band. To further check the feasibility of the observed octupole correlations in ^{142}Eu , the potential energy surface in the $\beta_{20} - \beta_{30}$ plane has been calculated in the framework of a microscopic MDC-CDFT formalism [18–20] with the effective interaction PC-PK1 [17] (Figure 5.18). The potential energy surface is very soft with respect to the shape degree of freedom β_{30} , which further upholds the propositions of octupole correlations in ^{142}Eu . Thus, the present investigation leads to the novel observation of two opposite parity bands, originating due to the interplay of PAR and TAR and interacting through the octupole interaction potential.

Table 5.6: The $B(E1)$ rate, $B(E1)/B(E2)$ ratio and the corresponding strength of the electric dipole moment vector (D_0) of the negative parity band DB II in ^{142}Eu .

J_i^π [\hbar]	E_γ [keV]	$B(E1)^a$ [10^{-4} W. u.]	$B(E1)/B(E2)$ [$10^{-6} fm^{-2}$]	D_0 [$10^{-2} efm$]
14^-	941.6	0.21 \uparrow		2.13 \uparrow
15^-	620.3	0.53 \uparrow		3.28 \uparrow
16^-	646.6	0.98 $^{+16}_{-17}$	0.10 $^{+2}_{-3}$	4.30 $^{+70}_{-76}$
17^-	610.2	0.94 $^{+14}_{-14}$	0.13 $^{+3}_{-3}$	4.14 $^{+60}_{-63}$
18^-	491.0	1.70 $^{+29}_{-25}$	0.56 $^{+13}_{-12}$	5.51 $^{+93}_{-80}$
19^-	539.1	1.57 $^{+34}_{-23}$	2.43 $^{+74}_{-50}$	5.22 $^{+111}_{-76}$

^a1 W. u. = $1.756 e^2 fm^2$ unit in $B(E1)$ is used to calculate D_0 .

**Figure 5.18:** The potential energy surface of ^{142}Eu calculated by the MDC-CDFT approach [18–20]. The contour separation is 0.25 MeV. The star mark corresponds to the point of the minimum energy.

5.4 Summary

In summary, the two opposite parity dipole bands DB I and DB II and one positive parity quadrupole band QB I in ^{142}Eu have been investigated. The configurations $\pi h_{11/2}^1 \otimes \nu h_{11/2}^{-1}$ and $\pi h_{11/2}^1 (d_{5/2}/g_{7/2})^{-2} \otimes \nu h_{11/2}^{-1}$ have been assigned to DB I before and after band crossing, respectively, whereas the configuration for DB II is $\pi h_{11/2}^2 (d_{5/2}/g_{7/2})^{-1} \otimes \nu h_{11/2}^{-1}$. The DB I has been established to be resulting from the interplay of PAR with MR phenomena representing the TAR while DB II emerges from the shears mechanism. The measured

electric dipole moment (D_0), energy displacement $\delta E(I)$ and rotational frequency ratio $\omega_-(I)/\omega_+(I)$ associated with the DB I and DB II as well as potential energy surface calculation in the framework of MDC-CDFT, indicate an octupole correlation in ^{142}Eu presumably due to availability of valence nucleons (protons) in the $d_{5/2} - h_{11/2}$ orbitals near the Fermi surface. This is the first experimental evidence of octupole correlation between two shears band.

The rotational band QB I with a band-head spin of 17^- is proposed as an AMR band based on the falling trend of $B(E2)$ values with spin. The falling rate of the $B(E2)$ values for the AMR band in ^{142}Eu is slower compared to the neighboring nucleus exhibiting an AMR band structure [42]. The reason for the latter may be due to a gradual increase in the core contribution along the AMR band. Numerical calculations in the framework of the SPRM model using the configuration $\pi g_{7/2}^{-1} \nu h_{11/2}^{-3} \otimes \pi h_{11/2}^2$ reproduce the experimental results. These results provide the first conclusive observation of the AMR phenomenon in an odd-odd nucleus.

CHAPTER 6

Structural Evolution in ^{140}Eu

6.1 Introduction

In the $A \sim 140$ region, the planer shears bands have been observed in many nuclei [1–3,6–9,33,34,42,43,107,110,130] and the chiral twin bands, which are the manifestation of the triaxial deformed shape, are observed up to $N = 77$ for ^{132}Cs ($Z = 55$) and up to $Z = 63$ for ^{138}Eu ($N = 75$) [131, 132]. The recent investigations of the island of nuclear chirality seems to indicate that the $N = 77$ isotones form the border of the island, when the neutron number approaches $N = 82$ [22, 23]. Therefore, it is interesting to see whether this conjecture holds for different $N = 77$ odd-odd isotones in the mass $A \sim 140$ region. It has also been observed that in some shears bands, the core angular momentum increases with excitation energy and spin. This opens up the possibility of transitions from planer to aplanar mode in the same nuclei in which shears band is observed at lower spin.

This chapter of the thesis describes the attempt to study the structural evolution of the $N = 77$ isotone viz. ^{140}Eu ($Z = 63$) nucleus of mass $A \sim 140$ region.

6.2 Survey of the existing work in ^{140}Eu

The high spin states of the ^{140}Eu nucleus were previously populated by the heavy-ion fusion evaporation reaction and were studied by employing both the recoil-isomer tagging and the conventional γ -ray spectroscopy technique [21, 69]. In the recoil isomer tagging experiment, the fusion evaporation reaction $^{107}\text{Ag}(^{36}\text{Ar}, 2\text{pn})$ was used to populate ^{140}Eu at beam energy of 152 and 181 MeV. The detection system consisted of 25 Compton-suppressed germanium detectors of the JUROSPHERE II spectrometer [21]. In the conventional γ -ray spectroscopy measurement, the $^{92}\text{Mo}(^{51}\text{V}, 2\text{pn})$ reaction was used to populate the high spin states of ^{140}Eu at a beam energy of 205 MeV. Seven Compton suppressed segmented clover detectors along with 16 Compton suppressed coaxial Germanium detectors were used to detect the deexciting γ -rays [21]. Based on these measurements, a total of 69 number of γ transitions were placed in the five band-like structures. The observed doublet structure was tentatively proposed to be chiral partners but experimental transitional probabilities viz. $B(M1)$ and $B(E2)$ values were not measured. In addition, one dipole cascade was identified without any connecting transition to the established bands. Thus, a detail spectroscopic study of ^{140}Eu was undertaken.

6.3 Experimental Planning

The wide variety of heavy-ion beams from the Pelletron-LINAC facility at Inter-University Accelerator Centre (IUAC) makes it possible to study the high spin nuclear states over different regions of the periodic table. Based on the statistical model calculations using Projected Angular momentum Coupled Evaporation (PACE4), an experiment was proposed to study the ^{140}Eu nucleus through the fusion evaporation reactions $^{112}\text{Cd}(^{32}\text{S}, \text{p}3\text{n})^{140}\text{Eu}$ at a beam energy of $E_{lab} = 140 - 150$ MeV or $^{112}\text{Sn}(^{32}\text{S}, 3\text{pn})^{140}\text{Eu}$ at beam energy between 155 - 160 MeV.

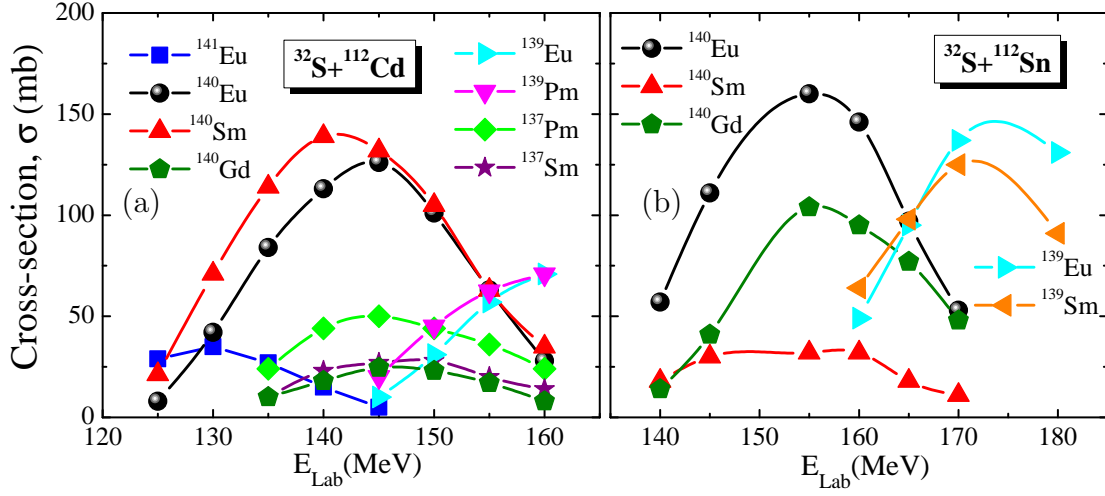


Figure 6.1: The calculated cross-section plots for the fusion of ^{32}S projectile with the (a) ^{112}Cd and (b) ^{112}Sn target to populate the ^{140}Eu residual nucleus according to PACE4. Many other channels with small cross-sections are also populated in these fusion reactions.

The choice of the target-projectile combination and the thickness of the target-backing material will be discussed in the next few sections.

6.3.1 Choice of Target-Projectile Combination: PACE4 Calculation

In a fusion evaporation experiment, the compound nucleus is expected to reach the thermodynamic equilibrium before decaying it to the daughter nuclei through particle evaporation. Thus, the statistical codes e. g. PACE4 or CASCADE, are used to obtain a reasonable prediction on the production cross sections of different daughter nuclei in a fusion evaporation reaction. According to PACE4 calculations, two fusion evaporation reactions $^{112}\text{Cd}(^{32}\text{S}, \text{p}3\text{n})$ and $^{112}\text{Cd}(^{32}\text{S}, \text{p}3\text{n})$ are found to be the most suitable to populate ^{140}Eu with a reasonable cross-section. Henceforth, the reactions $^{112}\text{Cd}(^{32}\text{S}, \text{p}3\text{n})$ and $^{112}\text{Cd}(^{32}\text{S}, \text{p}3\text{n})$ will be referred as reaction I and II, respectively. The reaction cross-sections as a function of projectile energy for the different channels of the reactions I and II were calculated using PACE4 and has been plotted in Figure 6.1 (a) and (b). The details of experimental parameters for the reactions I and II are summarized in

Table 6.1: Details of the experimental parameter calculation for the spectroscopic study of the ^{140}Eu .

Quantity	Reaction I	Reaction II
Target	^{112}Cd ($Z = 48$)	^{112}Sn ($Z = 50$)
Projectile	^{32}S ($Z = 16$)	^{32}S ($Z = 16$)
Projectile Energy	145 - 150 MeV	155 - 160 MeV
Compound Nucleus	^{144}Gd ($Z = 64$)	^{144}Dy ($Z = 66$)
Target Thickness	1.30 mg/cm ²	2.44 mg/cm ²
Backing	^{208}Pb ($Z = 82$)	^{208}Pb ($Z = 82$)
Baking Thickness	10.70 mg/cm ²	8.80 mg/cm ²
Total Cross-section	577 mb @ 145 MeV	634 mb @ 155 MeV
^{140}Eu Population %	21.8% @ 145 MeV	24.6% @ 155 MeV
Coulomb Barrier for Target	119 MeV	124 MeV
Coulomb Barrier for Backing	169 MeV	169 MeV
Maximum Angular Momentum transfer	$49\hbar$	$54\hbar$
Kinetic energy of the compound nucleus	32 MeV	34 MeV

Table 6.1.

6.3.2 Fabrication of ^{112}Cd and ^{112}Sn Target

In an in-beam γ spectroscopy experiment, choosing a suitable target-thickness has great importance. The thicknesses of the target and the backing (the nature of the backing) are dictated by the kind of spectroscopic measurements to be performed [133]. The measurements of the nuclear level lifetime can be performed using various techniques depending upon the range of the level lifetime [134]. For the measurement of the sub-picosecond lifetimes, the Doppler Shift Attenuation Method (DSAM) is widely used

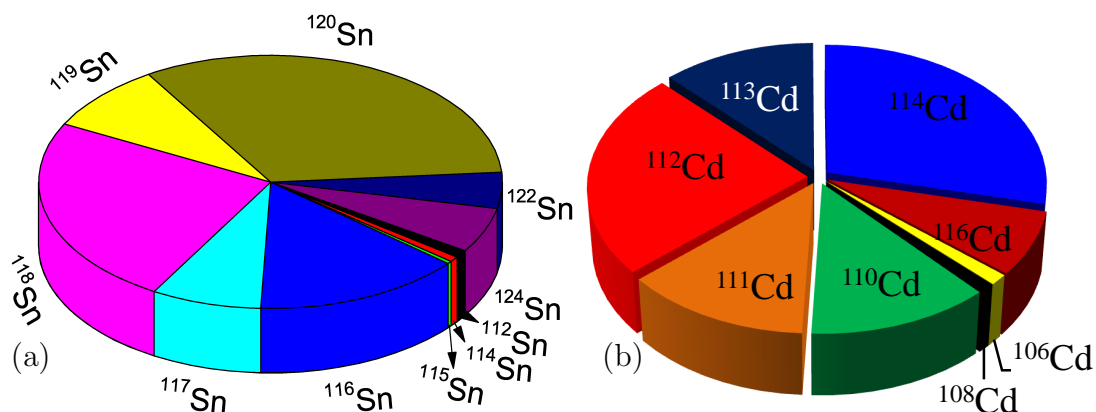


Figure 6.2: The representation of isotopic abundance of the (a) Tin, and (b) Cadmium isotope.

[135]. To perform measurement a thin target with a thick ($\sim 10 \text{ mg/cm}^2$) high-Z thick backing [136] is necessary.

The cold rolling technique was preferred for the preparation of a thin enriched target as there is minimal loss of material [137, 138]. This cold rolling technique can be used for both the malleable Cadmium and Tin materials. In the present scenario, only 5.6 mg of the ^{112}Cd material was available in the form of small pieces of foils. From this we could prepare a thin foil with a minimum dimension of $1 \text{ cm} \times 1 \text{ cm}$ as the diameter of the target holder is 1 cm. On the other hand, the ^{112}Sn material is very costly because of its poor isotopic abundance (0.97%, as shown in Figure 6.2 (a)). Therefore, it was essential to make the ^{112}Sn target with minimal loss. Hence, for the preparation of both of the targets, the vacuum-evaporation method was avoided as it leads to sizable loss of target material [139, 140]. However, before rolling, one need to prepare the blobs of ^{112}Sn and ^{112}Cd from the powder like material. The following procedures were applied for the preparation of the ingot.

6.3.2.1 Vacuum Sealing of the Target Material

The Vacuum sealing set-up at Saha Institute of Nuclear Physics (SINP), workshop contains a turbo-molecular pump to produce a high vacuum ($\sim 10^{-5}$ to 10^{-6} mbar), an LPG

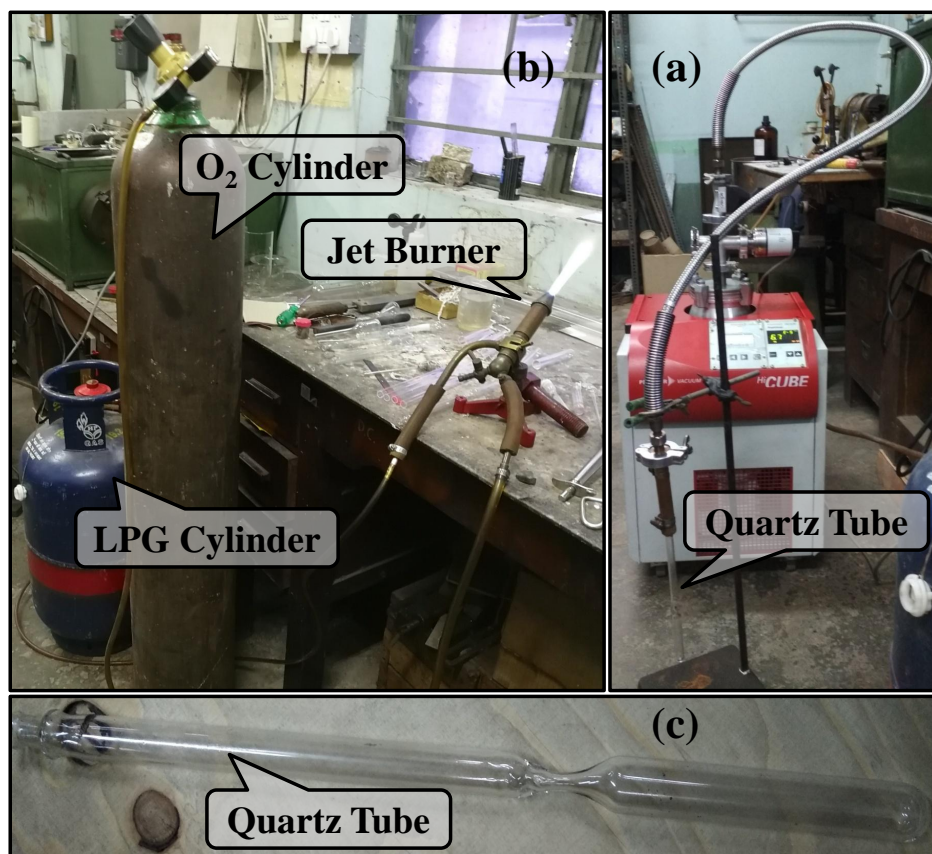


Figure 6.3: A photograph of vacuum tube sealing setup at SINP. The panel (a) shows a turbo-molecular pump, connected to a quartz-tube to be evacuated and in panel (b) the vacuum sealing set-up including gas cylinders and jet burner are shown. Panel (c) shows an enlarged view of a quartz-tube.

gas cylinder along with O_2 gas and a jet burner (Figure 6.3). At first, a long quartz-tube was connected to the turbo-molecular pump and the target material was kept in another quartz-tube. The quartz tubes were joined using LPG- O_2 flame. The tubes were disconnected by the same technique, after reaching the desired vacuum ($\sim 3 \times 10^{-5}$ mbar) inside the quartz-tube resulting the vacuum-sealed tube containing the target material.

6.3.2.2 Preparation of ^{112}Cd and ^{112}Sn Ingot

Ingots of the Cd and Sn have been prepared by keeping the vacuum-sealed quartz tube containing the target material inside the furnace. The vacuum sealing was required to avoid the oxidation of the target material.

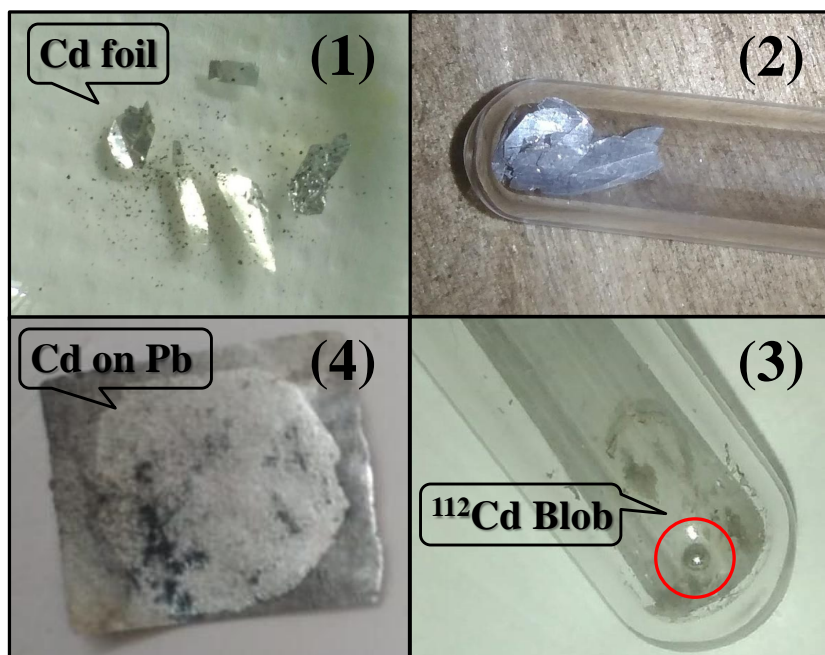


Figure 6.4: The images of the different stages of the foil preparation of the ^{112}Cd target on a Pb backing: (1) shows the small pieces of enriched ^{112}Cd material, (2) image of the vacuum-sealed quartz-tube containing the target material, (3) shows the ingot of the ^{112}Cd prepared by melting inside a furnace, (4) represents the image of the rolled ^{112}Cd target on a Pb backing.

(a) Ingot of ^{112}Cd :

Since, the amount of enriched isotope ^{112}Cd was very less (5.6 mg), the process was verified with the natural Cadmium. The melting and boiling points of the Cadmium material are $321.1\text{ }^\circ\text{C}$ and $766.8\text{ }^\circ\text{C}$, respectively. The sealed tube with few small pieces of natural cadmium was kept inside the furnace at $350\text{ }^\circ\text{C}$ for about 4 hour, but, the Cadmium material was did not melt to form a blob. Thus, the temperature of the furnace was increased by a step of $100\text{ }^\circ\text{C}$ for the same period of time, until the desired change was seen. Finally, at $600\text{ }^\circ\text{C}$, the pieces of Cadmium were melted to form a single blob.

After this exercise, the vacuum sealed quartz-tube containing the enriched ^{112}Cd material was kept in the furnace at $600\text{ }^\circ\text{C}$ for $\sim 3\text{-}4$ hours. Following the total melting of the Cadmium, a single blob of 3 mg material was prepared, from the 5.6 mg material as shown in Figure 6.4.

(a) Ingot of ^{112}Sn :

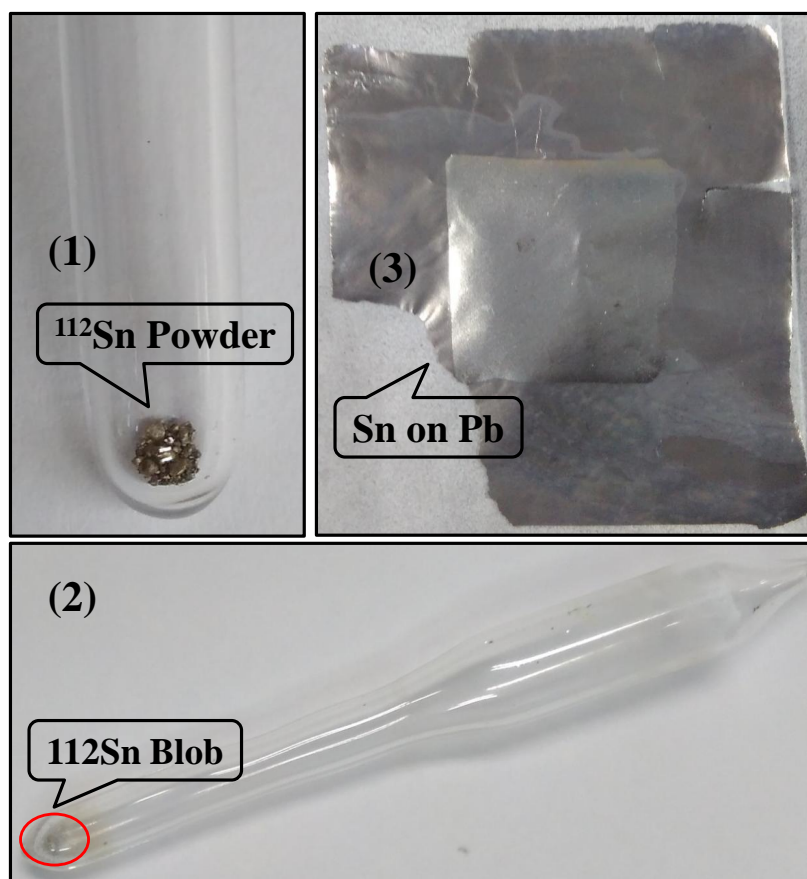


Figure 6.5: The image of the different stages of the foil preparation of the ^{112}Sn target on a Pb backing: (1) shows the powder like ^{112}Sn material inside a quartz tube, (2) the image of the vacuum-sealed quartz-tube which containing the ingot of the ^{112}Sn target material, (3) represents the image of the rolled ^{112}Sn target on a Pb backing.

Similar steps were carried out for the Sn material. The vacuum sealed quartz tube with natural Sn was kept at $300\text{ }^\circ\text{C}$ for about four hours, since the melting point of Tin is $232\text{ }^\circ\text{C}$. Still, the small pieces of Tin did not fully melt. Finally, the small pieces of Sn melted into a single blob is occurred at $900\text{ }^\circ\text{C}$.

An amount of 31.6 mg of the enriched ^{112}Sn metallic powder was taken inside a quartz tube and vacuum-sealed at $2.7 \times 10^{-5}\text{ mbar}$ and was kept inside the furnace at $900\text{ }^\circ\text{C}$ for four hours. A single piece of ^{112}Sn ingot was formed (as shown in Figure 6.5) having mass 31.0 mg . By the same technique, two more blobs of ^{112}Sn of mass 12.0 mg and 5.0 mg were prepared.

6.3.2.3 Rolling of the ^{112}Sn and ^{112}Cd Ingot

Using the method of cold rolling with the help of rolling machine at Saha Institute of Nuclear Physics (SINP) (Figure 6.6) and Tata Institute of Fundamental Research (TIFR), foils of different thicknesses can be made. The mechanical rolling machine contains two electrically controlled rollers. Both the plates can rotate in both clockwise and anti-clockwise directions, simultaneously. In the rolling process, the target material to be rolled is placed between two mirror polished stainless steel plates (SS), which in turn is placed inside the two rotating rollers. Inner surfaces of the SS plates is made dust free by cleaning with alcohol and acetone prior to inserting the target material between the plates.

(a) Rolling of ^{112}Sn Ingot:

The Teflon foils were used during the time of rolling to avoid the sticking of Sn with SS plates. The desired thickness 10.26 mg/cm^2 of the ^{112}Sn was reached after a number of rolling. The foil was cleaned to make it dust free using acetone and alcohol. In a similar way, a ^{208}Pb foil of thickness 22.5 mg/cm^2 was rolled to the desired thickness of 15.6 mg/cm^2 . The 10.26 mg/cm^2 ^{112}Sn foil and 15.6 mg/cm^2 ^{208}Pb foil were rolled together to make a sandwich. In this technique, two ^{112}Sn target with ^{208}Pb backing were prepared at SINP. One more ^{208}Pb backed ^{112}Sn target was prepared with the help of TIFR rolling machine having target and backing thicknesses of 2.44 mg/cm^2 and 8.8 mg/cm^2 , respectively (Figure 6.5). Using the same rolling process, two more self-supporting ^{112}Sn targets of 2.26 mg/cm^2 thickness were also prepared.

(a) Rolling of ^{112}Cd Ingot:

The ^{112}Cd piece of 3 mg, was rolled at TIFR to make a foil of dimension $1.5 \text{ cm} \times 1.4 \text{ cm}$ with a thickness of 1.3 mg/cm^2 . A Pb foil of thickness 10.7 mg/cm^2 was prepared using the SINP rolling machine. The foils were then sandwiched to prepare a Pb backed ^{112}Cd target by cold rolling (Figure 6.4).

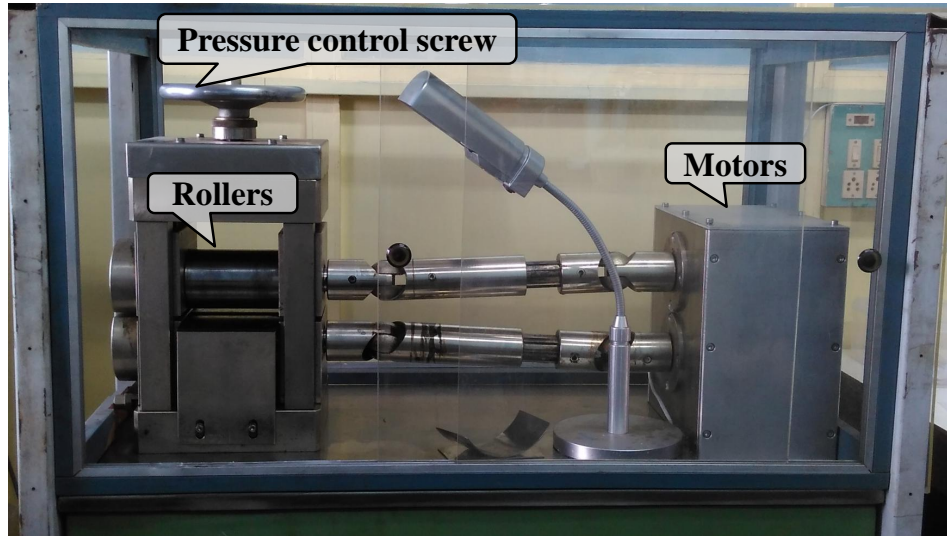


Figure 6.6: A photograph of the rolling machine at Saha Institute of Nuclear Physics.

6.4 Experimental Details

Two possible reactions $^{112}\text{Cd}(^{32}\text{S}, \text{p}3\text{n})$ and $^{112}\text{Sn}(^{32}\text{S}, 5\text{n})$ at beam energies 145 - 150 and 155 - 160 MeV, respectively, were proposed to populate the high spin states in ^{140}Eu .

At the time of experiment, the Pelletron facility of IUAC was found to attain a maximum charge state of 10^+ for ^{32}S ions with the terminal voltage up to 13.2 MV. Therefore, the maximum energy of the projectile ^{32}S could be achieved was $E_{lab} = (q + 1)V = 145.2$ MeV. Hence, the first reaction $^{112}\text{Cd}(^{32}\text{S}, \text{p}3\text{n})$ was chosen to populate the ^{140}Eu . The detection system used was the Indian National Gamma Array (INGA) which consisted of sixteen Compton suppressed clover detectors, positioned at five different angles: (i) four at 148° , (ii) two at 123° , (iii) six at 90° , (iv) one at 57° , and (v) three at 32° . The de-exciting γ -ray events were only recorded when at least two detectors had fired within a time window of 800 ns.

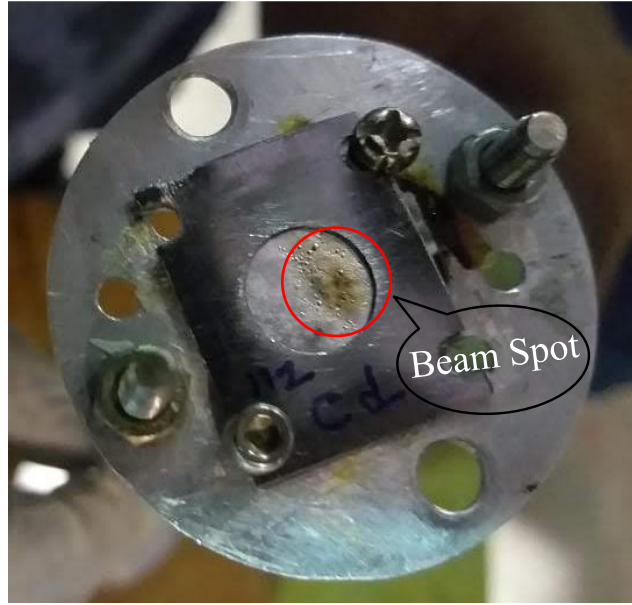


Figure 6.7: The photographed of the ^{112}Cd target after the experiment, which shows the beam spot (encircled).

6.5 Data Analysis Techniques

The γ - γ coincidence events were sorted to make the E_γ - E_γ matrices and E_γ - E_γ - E_γ cube and were analyzed to extract the desired information using the INGASORT and RADWARE software packages [82–84].

The different types of matrices that have been analyzed are:

(i) A symmetric $4k \times 4k$ E_γ - E_γ matrix containing the events of from all detectors to determine the coincidence relationships.

(ii) An angle-dependent $4k \times 4k$ asymmetric matrix is also formed to determine the DCO ratio (R_{DCO}) for the observed γ -rays (see Chapter 3 for details).

The detectors at $\theta_1 = 148^\circ$ and $\theta_2 = 90^\circ$ with respect to the beam direction were used to evaluate R_{DCO} . For the present geometry, the experimental value of $R_{DCO} \approx 0.5$ (2.0) is expected for a pure dipole (quadrupole) transition by gating on a stretch quadrupole (dipole) one. On the other hand, if the gated transition and observed transition have

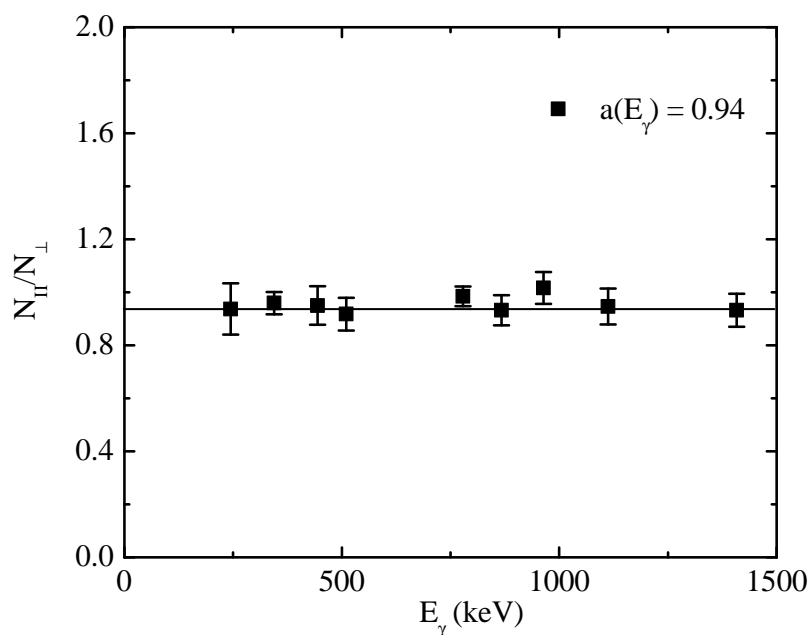


Figure 6.8: The geometrical asymmetry correction factor $a(E_\gamma)$ using the unpolarized radioactive source, ^{152}Eu and ^{133}Ba .

same multipolarity then $R_{DCO} \approx 1$, as predicted by the ANGCOR code [89].

(iii) Specific angle-dependent γ - γ asymmetric $4k \times 4k$ matrices were created for the evaluation of the ADO ratio ($R(\theta)$) (Details in Chapter 3).

For the present geometry, ($\theta_1 = 148^\circ$ and $\theta_2 = 90^\circ$), the value of $R(\theta)$ for pure dipole (pure quadrupole) transitions is $\approx 0.6(1.7)$ and the transitions which deviate from these values have mixed multipolarity. Also for the level lifetime measurements by the DSAM technique, these angle dependent matrices were used.

(iv) Two asymmetric E_γ - E_γ matrices were created with either horizontally (N_{\parallel}) or vertically (N_{\perp}) scattered γ -rays (at 90° detectors) on one axis and the coincident γ -rays from all the detectors on the other axis. The geometrical asymmetry ($a(E_\gamma) = N_{\parallel}/N_{\perp}$) corrected PDCO (Δ) was defined in Chapter 3 which determines the electromagnetic nature of the γ transitions. A near-zero value of the Δ is indicative of a mixed transition, while the negative value corresponds to the magnetic transition and the positive value corresponds to the electric nature of the transitions. The geometrical asymmetry correction factor ($a(E_\gamma)$) [8, 91] for the present data has been plotted in Figure 6.8.

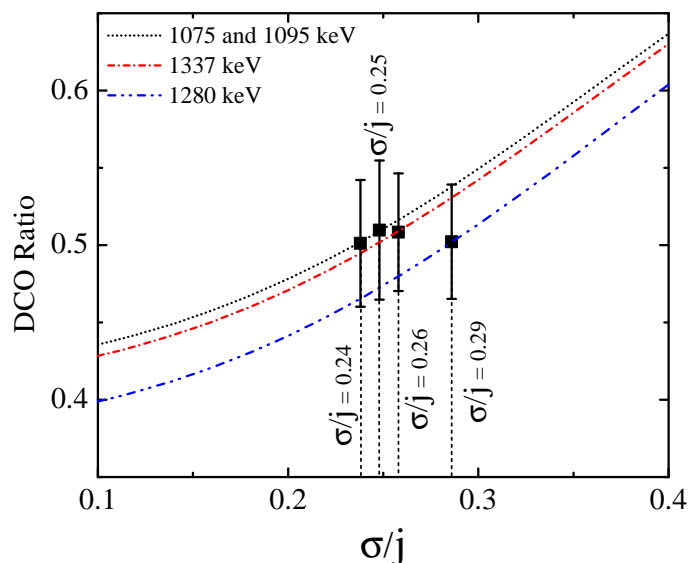


Figure 6.9: Theoretical R_{DCO} values for the different σ/j ratios (represented by black, red, and blue lines) calculated using the ANGCOR program [89]. The calculated curves match with the experimental R_{DCO} values (represented by solid square) for the 1074.6 keV ($15^- \rightarrow 14^+$), 1095.2 keV ($15^- \rightarrow 14^+$) and 1337.1 keV ($13^- \rightarrow 12^+$) $E1$ transition of ^{140}Sm and 1280.2 keV ($17/2^+ \rightarrow 15/2^-$) $E1$ transitions of ^{141}Eu , assuming $\sigma/j = 0.24(6)$, $0.25(7)$ and $0.26(5)$, and $0.29(5)$, respectively.

The following sections report the results obtained from the aforementioned analysis and the interpretations of the results.

6.6 Experimental Results

6.6.1 Width of the Substate Population

The determination of the width of the sub-state population (σ/j) for the present reaction is very important in order to determine the electromagnetic nature of the γ transitions. It was estimated using the pure dipole ($E1$) transitions of energy 1074.6 keV ($15^- \rightarrow 14^+$), 1095.2 keV ($15^- \rightarrow 14^+$) and 1337.1 keV ($13^- \rightarrow 12^+$) in ^{140}Sm and 1280.2 keV ($17/2^+ \rightarrow 15/2^-$) in ^{141}Eu . The R_{DCO} -value was extracted by gating on the stretched $E2$ transition. The observed values of the R_{DCO} were reproduced using the ANGCOR code by varying σ/j ratio as shown in Figure 6.9. The experimental R_{DCO} values for the

1074.6, 1095.2, 1337.1, and 1280.2 keV transitions were reproduced with the σ/j ratio as 0.24(6), 0.25(7), 0.26(5), and 0.29(5), respectively. The weighted average of the $\sigma/j = 0.26(6)$ has been adopted for further analysis of the data.

6.6.2 Construction of the Level Scheme

All the previously reported transitions of the ^{140}Eu by the D. M. Cullen *et al.*, Hecht *et al.* and Tantawy *et al.* [21, 69, 141] were observed and confirmed in the present experiment. Hecht *et al.* [21] had reported the level scheme of ^{140}Eu in which positive and negative parity parts were not connected. The lower spin part (up to 8^+) was analyzed from decay studies by Tantawy *et al.* [141] and the 302 ns isomer state was assigned $I^\pi = 8^+$ instead of 9^+ reported by Hecht *et al.* [21]. In the present level scheme the $I^\pi = 8^+$ assignment has been adopted. In the current experimental analysis level scheme has been constructed above the 5^- (125 ms) isomer [141]. The excited level scheme of ^{140}Eu was constructed from the present data (Figure 6.10) using the doubles and triples coincidences between the γ events with the help of Radware and Ingasort software packages [82–84].

The measured γ transition energies and total intensities, together with the extracted R_{DCO} , $R(\theta)$, and PDCO (Δ) for transitions in ^{140}Eu are listed in Table 6.2. The intensities were determined with respect to the intensity of the 640.4 keV transition, which was assumed as 100. The multipolarities of the observed transitions were determined by the angular correlation (R_{DCO} , $R(\theta)$) and PDCO (Δ) measurements of the γ -ray transitions. For the R_{DCO} measurements the stretched $E2$ transitions were used as gating transitions.

Table 6.2: The transition energy (E_γ), the relative intensity (I_γ), the R_{DCO} , the $R(\theta)$, the PDCO (Δ) and the assignment of the gamma transitions in ^{142}Eu . The newly observed transitions are marked by asterisk.

Energy ^a (E_γ)	Intensity ^b (I_γ)	J_i^π	J_f^π	DCO ratio ^c (R_{DCO})	ADO ratio ($R(\theta)$)	PDCO (Δ)	Assignment
94.5	81.4(64)	8 ⁺	7 ⁺	1.29(18)	1.86(15)		(M1/E2)
97.6	75.9(28)	8 ⁺	7 ⁻	2.43(23)	2.62(13)		(E1)
104.1	21.3(15)	7 ⁻	6 ⁻		2.64(14)		(M1/E2)
137.5	27.1(11)	7 ⁻	6 ⁻	0.61(17)	2.16(7)		(M1/E2)
152.6	7.4(10)	12 ⁻	11 ⁻		1.29(26)		(M1/E2)
156.5*	3.7(4)	11 ⁺	10 ⁺	0.56(10)	0.69(8)		(M1/E2)
169.8	23.6(24)	14 ⁻	13 ⁻	0.80(5)	1.10(10)		(M1/E2)
170.4	102.6(21)	6 ⁻	5 ⁻	0.91(3)	1.32(3)		(M1/E2)
190.9	59.8(13)	7 ⁻	6 ⁻	0.56(2)	0.91(3)		(M1/E2)
209.8	4.2(4)	13 ⁻	12 ⁻	2.83(41)	1.29(3)		(M1/E2)
230.4	21.4(12)	13 ⁻	12 ⁻	0.55(5)	1.01(6)	+0.02(1)	(M1/E2)
243.9*	6.96(5)	9 ⁻	8 ⁻	0.52(7)	0.56(4)	+0.01(1)	M1/E2
252.3	74.8(24)	7 ⁻	6 ⁻	0.72(7)	1.20(9)	+0.04(1)	M1/E2
257.9	10.0(7)	13 ⁻	12 ²	0.49(9)	0.86(8)		(M1/E2)
274.5	18.1(23)	11 ⁺	10 ⁺	0.83(18)	1.29(18)	+0.04(1)	M1/E2
275.5	2.2(3)	14 ⁻	13 ⁻		0.58(6)		(M1/E2)
285.1	49.1(24)	6 ⁻	5 ⁻	0.62(5)	0.89(7)	+0.03(1)	(M1/E2)
292.8	8.2(9)	8 ⁻	7 ⁻	0.43(8)	0.76(7)	+0.08(3)	M1/E2
317.0*	1.6(4)	13 ⁺	12 ⁺		0.92(21)		(M1/E2)
317.6*	4.7(6)	11 ⁽⁺⁾	10 ⁺	0.67(15)	0.98(17)		M1/E2
327.9*	11.2(10)	12 ⁺	11 ⁽⁺⁾	0.62(8)	0.77(8)		(M1/E2)
345.3	2.7(4)	14 ⁻	13 ⁻	0.58(6)	0.40(4)		(M1/E2)
346.5*	2.5(4)	13 ⁺	12 ⁺	0.44(11)	0.89(21)		(M1/E2)

Continued on next page

Table 6.2 – *Continued from previous page*

Energy ^a (E_γ)	Intensity ^b (I_γ)	J_i^π	J_f^π	DCO ratio ^c (R_{DCO})	ADO ratio ($R(\theta)$)	PDCO (Δ)	Assignment
361.4	19.5(19)	13 ⁺	12 ⁺	0.64(6)	1.61(5)	−0.14(2)	M1/E2
361.6	39.4(33)	7 [−]	5 [−]	0.99(5)	0.68(6)	+0.15(1)	E2
365.9	39.9(27)	10 ⁺	9 ⁺	0.50(6)	0.67(5)	+0.19(3)	M1/E2
372.7	11.8(8)	15 [−]	14 [−]	0.56(6)	0.62(3)	−0.06(1)	M1/E2
379.2	1.3(2)	18 ^(−)	17 ^(−)		0.70(26)		(M1/E2)
385.6	36.6(42)	10 ⁺	8 ⁺	0.96(10)	1.52(10)	+0.06(1)	E2
390.4	25.0(27)	7 [−]	5 [−]	0.46(8)	0.48(10)		(E2)
396.5	2.4(6)	15 ^(−)	14 [−]		0.72(6)		(M1/E2)
397.2	1.6(4)	18 ^(−)	17 ^(−)		1.06(17)	+0.01(1)	(M1/E2)
401.5	8.4(11)	8 [−]	7 [−]	0.48(4)	1.33(18)	−0.02(1)	M1/E2
406.3	40.4(42)	10 ⁺	8 ⁺	1.23(4)	1.81(4)	+0.41(3)	E2
418.1*	2.6(7)	15 ⁽⁺⁾	14 ⁺	0.65(13)	0.66(14)		(M1/E2)
422.9	77.4(44)	7 [−]	5 [−]	1.13(11)	1.64(13)	+0.19(4)	E2
445.9	61.6(37)	12 ⁺	11 ⁺	0.35(7)	0.62(4)	−0.05(1)	(M1/E2)
454.1	4.5(5)	16 [−]	15 [−]	0.38(14)	0.88(9)	−0.01(1)	(M1/E2)
460.0	2.7(4)	17 ^(−)	16 [−]	0.63(14)	1.0(12)		(M1/E2)
466.1*	2.5(4)	10 [−]	9 [−]	0.57(7)	0.95(7)		(M1/E2)
469.7	23.4(23)	14 ⁺	13 ⁺	0.26(3)	0.45(3)	−0.05(1)	M1/E2
471.5	11.4(12)	16 ^(−)	15 ^(−)		0.66(5)	−0.04(1)	M1/E2
477.5*	1.6(5)	10 [−]	9 [−]				(M1/E2)
477.9	13.9(12)	8 [−]	6 [−]	0.95(31)	1.88(25)	+0.15(1)	E2
483.6	5.9(7)	10 ⁺	9 ⁺	0.44(7)	0.89(6)		(M1/E2)
483.7*	4.0(5)	13 [−]	12 [−]	1.07(11)	1.67(13)		(M1/E2)
484.3	34.6(27)	8 [−]	6 [−]	1.08(9)	1.88(5)	−0.07(1)	E2

Continued on next page

Table 6.2 – *Continued from previous page*

Energy ^a (E_γ)	Intensity ^b (I_γ)	J_i^π	J_f^π	DCO ratio ^c (R_{DCO})	ADO ratio ($R(\theta)$)	PDCO (Δ)	Assignment
489.7	16.4(9)	12 ⁺	11 ⁺	0.36(7)	0.50(3)	−0.09(1)	M1/E2
501.8	19.3(18)	14 ⁺	13 ⁺	0.26(3)	0.66(4)	−0.01(1)	M1/E2
510.9	62.4(34)	16 ⁺	14 ⁺	0.89(3)	1.46(3)	+0.17(1)	E2
537.4	36.7(22)	7 [−]	5 [−]	0.92(4)	1.81(7)	+0.26(3)	E2
554.6*	3.5(8)	10 ⁺	8 ⁺	1.06(18)	1.79(35)		(E2)
590.2*	8.1(8)	12 ⁽⁺⁾	10 ⁺	1.19(8)	1.63(7)		(E2)
597.5*	3.7(5)	12 ⁽⁺⁾	10 ⁺				(E2)
601.2	21.2(15)	10 [−]	8 [−]	1.09(8)	1.13(6)	+0.20(3)	E2
611.4	14.7(16)	14 ⁽⁺⁾	12 ⁺	0.90(4)	1.43(17)		(E2)
612.8	2.9(5)	17 ^(−)	15 [−]	0.95(19)	1.60(19)		(E2)
615.1	16.1(23)	16 ⁺	14 ⁺	0.97(13)	1.83(26)		(E2)
618.9	30.2(35)	12 ⁺	10 ⁺	1.14(5)	1.34(9)	+0.18(3)	E2
632.4*	2.5(5)	12 [−]	11 ^(−)		0.52(8)		(M1/E2)
637.4*	8.8(12)	16 ⁽⁺⁾	14 ⁽⁺⁾	1.15(10)	1.66(19)		(E2)
640.2	100.0(56)	11 ⁺	9 ⁺	1.12(5)	1.89(6)	+0.16(2)	E2
646.9	42.6(24)	12 ⁺	10 ⁺	1.01(5)	1.41(6)	+0.12(2)	E2
647.0	62.4(37)	18 ⁺	16 ⁺	0.89(4)	1.74(6)	+0.19(1)	E2
649.3*	2.2(4)	13 ^(−)	12 ^(−)		0.91(9)		(M1/E2)
709.5	21.8(14)	10 [−]	8 [−]	0.95(6)	1.94(9)	+0.09(1)	E2
715.1	26.0(26)	11 [−]	9 [−]	0.93(4)	1.45(6)	+0.09(1)	E2
720.2	27.9(15)	12 ⁺	10 ⁺	1.06(13)	1.51(16)	+0.12(2)	E2
721.1	13.1(8)	10 [−]	8 [−]	0.75(5)	1.61(6)	+0.16(1)	E2
748.3*	11.9(14)	13 ⁽⁺⁾	11 ⁺	1.04(18)	1.25(17)		(E2)
753.7	38.5(24)	20 ⁺	18 ⁺	1.15(10)	1.46(5)	+0.12(2)	E2

Continued on next page

Table 6.2 – *Continued from previous page*

Energy ^a (E_γ)	Intensity ^b (I_γ)	J_i^π	J_f^π	DCO ratio ^c (R_{DCO})	ADO ratio ($R(\theta)$)	PDCO (Δ)	Assignment
764.5*	4.1(5)	12 ⁺	10 ⁺		1.54(39)		(E2)
785.8*	1.9(0.3)	12 ⁽⁻⁾	11 ⁻		0.82(8)		(M1/E2)
786.7	36.8(21)	14 ⁺	12 ⁺	0.89(4)	1.54(4)	+0.18(2)	E2
804.5	18.5(15)	12 ⁻	10 ⁻	1.02(9)	1.63(9)	+0.09(1)	E2
806.7	52.5(49)	13 ⁺	11 ⁺	0.88(4)	1.73(11)	+0.11(1)	E2
812.5*	11.6(9)	15 ⁽⁺⁾	13 ⁺	1.07(14)	1.44(21)		(E2)
813.8*	2.5(4)	13 ⁻	11 ⁻	1.06(30)	1.45(11)		(E2)
818.7	16.8(12)	13 ⁺	11 ⁺	0.90(9)	1.46(17)		(E2)
819.9	7.0(7)	12 ⁻	10 ⁻	1.09(14)	1.63(9)	+0.04(1)	E2
827.3	2.1(3)	16 ⁻	14 ⁻	1.06(37)	1.64(17)		(E2)
829.5	15.6(14)	13 ⁻	11 ⁻	0.89(8)	1.60(6)	+0.06(1)	E2
830.9	41.4(32)	15 ⁺	13 ⁺	1.11(8)	1.46(17)	+0.12(1)	E2
832.3	22.4(19)	12 ⁻	10 ⁻	1.03(12)	1.49(4)	+0.17(2)	E2
863.1*	8.8(7)	14 ⁺	12 ⁺		1.82(14)		(E2)
870.4*	1.9(4)	11 ⁽⁻⁾	10 ⁻				(M1/E2)
906.9	11.1(16)	22 ⁺	20 ⁺	0.87(5)	1.38(16)	+0.07(1)	E2
910.4*	3.9(5)	13 ⁽⁺⁾	11 ⁺		1.64(52)		(E2)
914.4	3.3(4)	17 ⁽⁻⁾	15 ⁻		1.70(24)		(E2)
919.5	23.4(13)	15 ⁺	13 ⁺	0.88(9)	1.66(18)	+0.09(1)	E2
924.9	8.4(8)	12 ⁻	10 ⁻	1.18(12)	1.71(9)	+0.08(1)	E2
985.8	4.7(7)	24 ⁺	22 ⁺				(E2)
993.6	7.1(9)	22 ⁺	20 ⁺	1.09(25)	2.03(23)	+0.12(3)	E2
1003.9	9.8(11)	22 ⁺	20 ⁺	0.95(17)	1.45(10)	+0.11(2)	E2

^aUncertainty in γ ray energy is \pm (0.1-0.3) keV.*Continued on next page*

Table 6.2 – *Continued from previous page*

Energy ^a (E_γ)	Intensity ^b (I_γ)	J_i^π	J_f^π	DCO ratio ^c (R_{DCO})	ADO ratio ($R(\theta)$)	PDCO (Δ)	Assignment
---------------------------------------	--	-----------	-----------	---	------------------------------	-------------------	------------

^bIntensities of γ rays are normalized to the 640. keV transition, with $I_\gamma = 100.0$.

^cCalculated by gating on stretched $E2$ transitions.

In the earlier measurement [21], a cascade of $M1$ transitions having energies 152.6, 209.8, 275.5, 396.5, and 471.5 keV was reported, which was not connected with the established level scheme. In the present coincidence measurements, five new transitions 649.3, 785.8, 632.4 and 870.4 keV (shown in Figure 6.11) were found which connects this cascade to the level scheme (Figure 6.10). Because of the weak nature of these transitions, only the $R(\theta)$ measurements were possible (Table 6.2). Thus, the parity of the suspended $M1/E2$ cascade has been assigned tentatively. The 537.4 keV (QB 1) and 484.3 (QB 2) keV gates showed the presence of four new connecting transitions of 466.1, 477.5, 483.7 and 813.8 keV between the bands QB 1, QB 2 and QB 3. In the positive parity levels, many new connecting transitions were also observed and placed between QB 5, QB 6, QB 7 and QB 8 (Figure 6.10). In addition, a new quadrupole band QB 9, was established using the 406.3 and 646.9 keV gates (Figure 6.12). The placements of the γ transitions in the quadrupole band QB 10 was rearranged and a new transition of energy 637.4 keV was placed at top of the band. The spin-parity of this band has been assigned from the R_{DCO} , $R(\theta)$ and PDCO measurements. In this present analysis, ten quadrupole bands (QB 1 to QB 10) and two dipole bands (DB 1 and DB 2) could be established (Figure 6.10).

6.6.3 Level Lifetime Measurements

The level lifetime of the six levels of the positive parity side in ^{140}Eu were extracted in the present thesis work using the DSAM technique. The Doppler broadened lineshapes

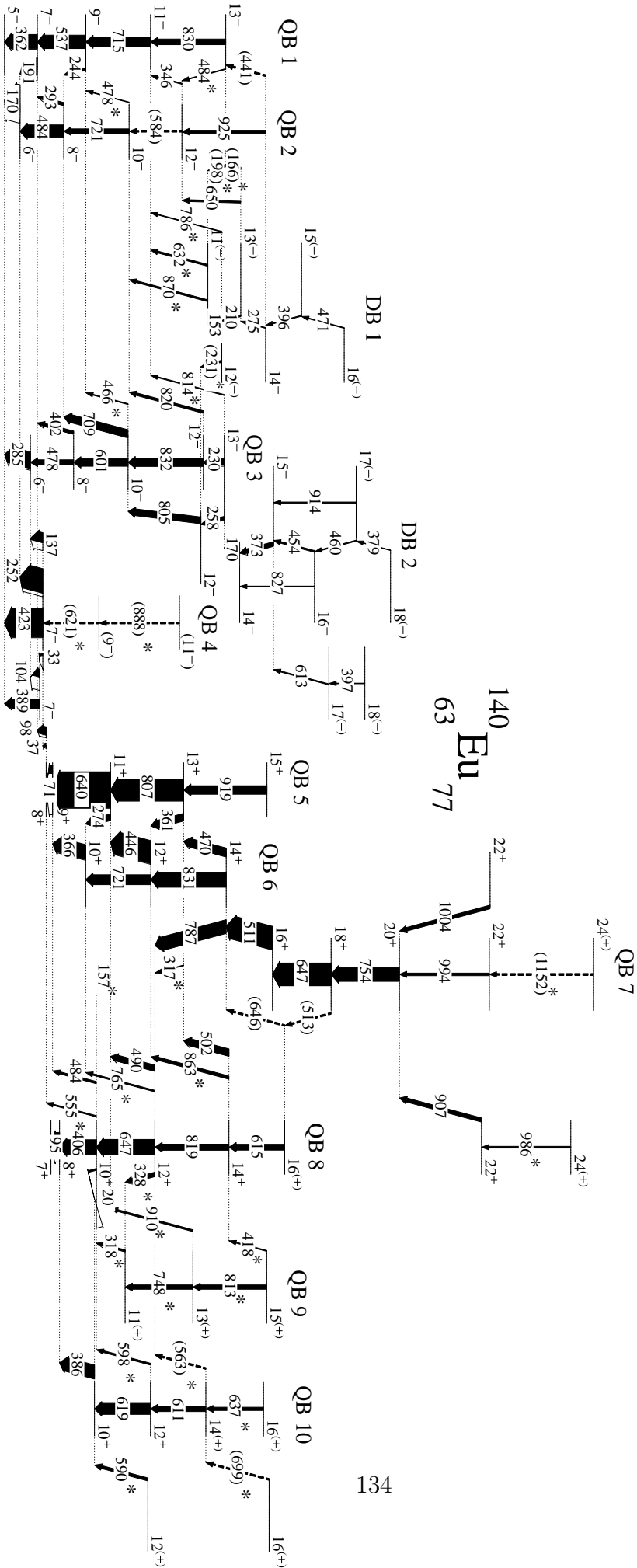


Figure 6.10: The partial proposed level scheme of ^{140}Eu deduced from the present analysis. The newly observed transitions are marked by asterisk. The width of the γ -rays represent the relative intensities. Intensity of the γ transitions having energies less than 80 keV were not measured due to experimental limitation.

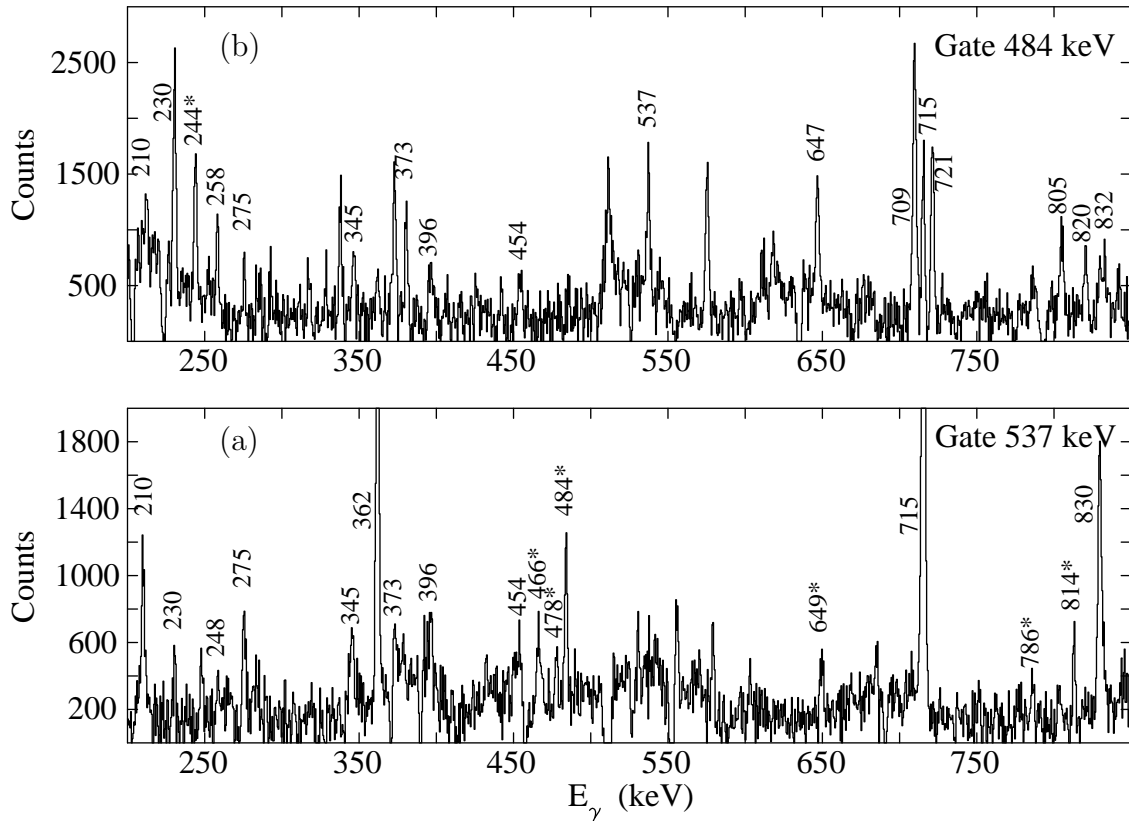


Figure 6.11: The gated spectra of (a) 537.4 keV and (b) 484.3 keV transitions in the negative parity structure of ^{140}Eu . The newly observed transitions are marked by asterisk.

at 32° , 90° and 148° were fitted simultaneously by the LINESHAPE packages [97].

The coincidence spectra exhibited lineshapes for the transitions 919.5, 806.7, 640.2 keV of QB 5, 445.9 keV of QB 6 and 993.6, 753.7 keV of QB 7. The lineshape for the 919.5 keV ($15^+ \rightarrow 13^+$) transition was fitted to extract the effective lifetime of 1.03 ps for the 15^+ state. This effective lifetime was then used as the input parameter for measuring the lower lying levels of the QB 5. To measure the level lifetime of the 12^+ state of QB 6, the Doppler broadened lineshape of the depopulating transition 445.9 keV was fitted. The 13^+ level of the QB 5 also decays to QB 6 by the 361.4 keV (13^+ of QB 5 $\rightarrow 12^+$ of QB 6) transition. The level lifetime contribution from the 13^+ level of the QB 5 was included by the intensity weighted average lifetimes in the simultaneous fitting of the lineshape of 445.6 keV.

The 20^+ level of the QB 7 is populated through three transitions 906.9, 993.6, and

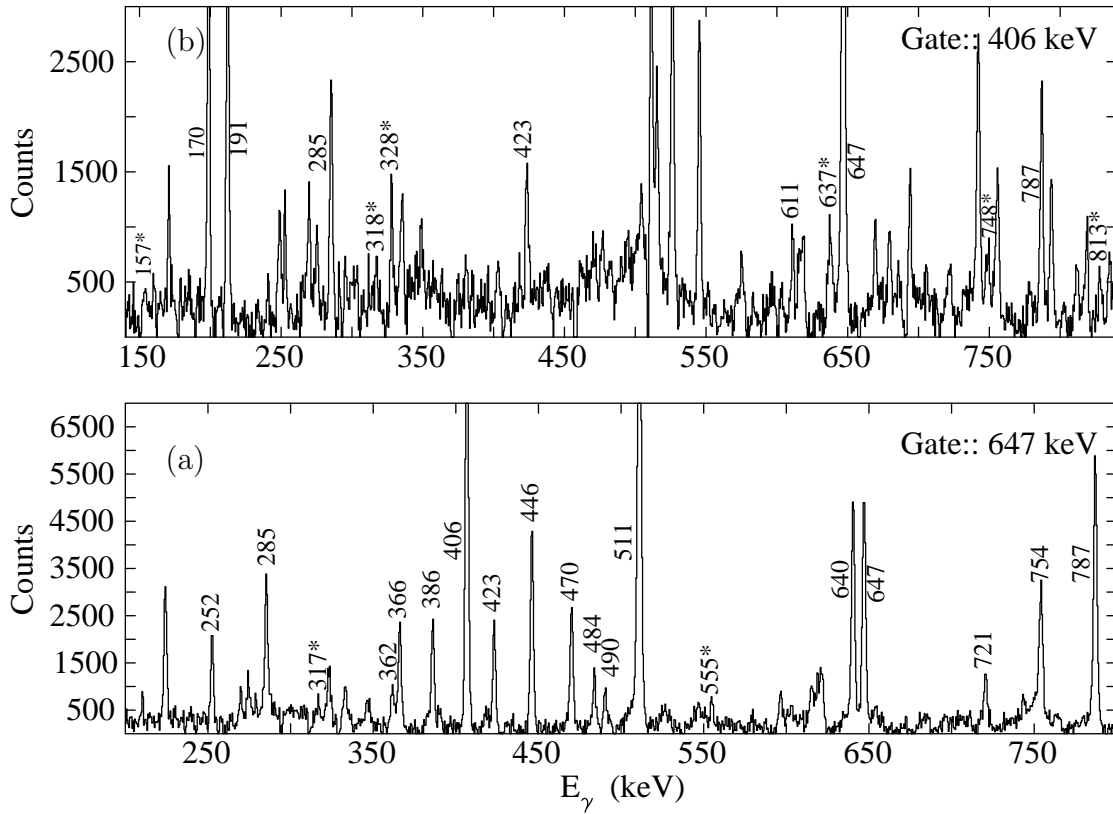


Figure 6.12: The gated spectra of (a) 646.9 keV and (b) 406.3 keV transitions in the positive parity structure of ^{140}Eu . The newly observed transitions are marked by asterisk.

1003.9 keV and all the transitions exhibit lineshapes. The lineshape of the 906.9 keV was fitted to measure the effective lifetime of 1.10 ps of the 22^+ . But the lineshapes for 993.6 and 1003.9 keV transitions overlap and the extraction of the effective lifetimes of the other two 22^+ levels were not possible by the gating from the bottom of the transitions. On the other hand, the weaker intensities of the transitions above 20^+ did not allow the extraction of lineshapes using the gates from the top. The 20^+ state of QB 7 was found to decay through the 753.7 keV transition which showed clear lineshape. Since, the effective lifetimes for the other two 22^+ levels could not be estimated, only the effective lifetime for the $I^\pi = 20^+$ level was determined. Some of the typical fitted lineshape spectra are shown in Figure 6.13 and the extracted level lifetimes and the transition probabilities are tabulated in the Table 6.3.

Table 6.3: The measured level lifetimes and the estimated $B(M1)$ and $B(E2)$ values for the QB 5, QB 6 and QB 7 in ^{140}Eu .

Band	J^π	$E_\gamma(\text{keV})$	$\sigma\lambda$	BR (%)	$\tau(\text{ps})$	$B(M1)\mu_N^2$	$B(E2)e^2b^2$
QB 5	11 ⁺	640.2	E2	0.82(11)	1.79_{-54}^{+51}	0.20_{-6}^{+6}	0.35_{-10}^{+10}
		274.5	M1/E2	0.15(2)			
	13 ⁺	806.7	E2	0.71(9)	1.74_{-45}^{+49}	0.18_{-5}^{+5}	0.10_{-3}^{+3}
		361.4	M1/E2	0.26(3)			
	15 ⁺	919.5	E2	1.00(6)	$< 1.03^a$		$> 0.13^b$
QB 6	12 ⁺	720.2	E2	0.30(3)	1.61_{-44}^{+43}	0.27_{-8}^{+7}	0.08_{-2}^{+2}
		445.9	M1/E2	0.70(6)			
QB 7	20 ⁺	753.7	E2	1.00(6)	$< 1.32^a$		$> 0.25^b$
	22 ⁺	906.9	E2	1.00(14)	$< 1.10^a$		$> 0.12^b$

^aEffective lifetime is obtained assuming 100% side-feeding intensity.

^bLower limit of the $B(E2)$ value.

6.6.4 Discussion

From the present data a detail level scheme could be established only up to $I \sim 20\hbar$. This was surprising as ^{140}Eu was populated using ^{32}S beam. The reason may be attributed to two different observations:

(a) the current data volume is insufficient to populate the ten bands with substantial intensity. It is interesting to note that the levels of same spin of all the bands have very similar energy. Thus, the population got evenly spread over the ten band structures.

(b) The backed target data had substantial lineshapes for all the transitions depopulating the high spin ($I > 20\hbar$) levels. This made the identification of these transitions difficult in the different gated spectra.

Thus, to extend the level scheme to the 4-qp bands, it is necessary to carry out a thin target experiment in future. Once γ transitions are identified, the present data may be used to extract the level lifetimes.

The partial level structure established from the present work, does not indicate the

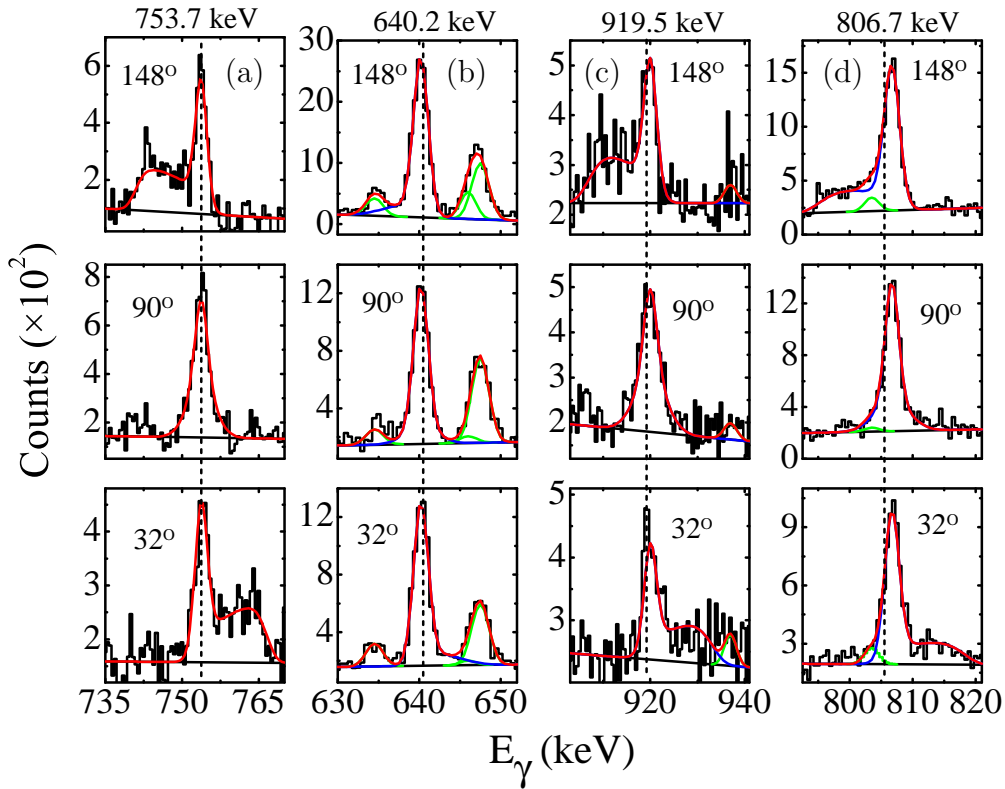


Figure 6.13: The observed line shapes and the fitted spectra for the (a) 753.7, (b) 640.2, (c) 919.5, and (d) 806.7 keV γ transitions of the positive parity quadrupole bands in ^{140}Eu . The first, second and last row corresponds to the spectra at the 148° , 90° and 32° , respectively. The blue, green, and red curves represent the line shapes of the γ transitions, contaminant peaks and total line shapes, respectively.

presence of any chiral doublet structure in the low spin domain ($I < 20\hbar$) of ^{140}Eu .

6.6.5 Summary

In summary, an experiment has been proposed and performed at INGA facility to study the high spin behavior in ^{140}Eu . To perform this experiment, the foils ^{112}Cd and ^{112}Sn target material with Pb backing are prepared. The data taken during the experiment was analyzed to construct the partial levelscheme of ^{140}Eu (Figure 6.10). Two dipole bands and ten quadrupole bands have been established and a large number of new transitions were identified and placed. The level lifetime of the six positive parity levels were extracted using DSAM technique. No signature of a chiral doublet structure could be identified in the present level scheme.

CHAPTER 7

Future Outlook

In the present thesis, the various mechanisms for the generation of angular momentum in the weakly deformed nuclei, ^{141}Sm , ^{142}Eu and ^{140}Eu , in mass $A \sim 140$ region are comprehensively investigated.

The observed partner bands in ^{141}Sm (above $I^\pi = 35/^-$) seems to be a perfect candidate for the five quasiparticle chiral doublet. This structure has not been observed yet. A future experiment with a thin target may help in extending the bands to higher spins and estimate the intensities of the γ transitions accurately. In addition, the present experiment needs to be repeated in future for collection of more statistics which is necessary to estimate the transition rates beyond $I^\pi = 39/2^-$.

In ^{142}Eu , AMR band is observed which is a novel observation in an odd - odd nuclei. Furthermore, octupole correlation between two MR bands was established in the same nucleus. This is the first observation of this phenomena.

The diversity of excitation mechanisms in the weakly deformed nuclei occur because of the coexistence of the shears mechanism and the collective rotation. In mass $A \sim 140$ region, the length of the shears blades is intermediate compared to the larger shears blades in $A \sim 200$ region and smaller shears blades in $A \sim 100$ region. The shears bands in the $A \sim 200$ region are entirely generated from the quasiparticles contribution while

the shears bands in $A \sim 100$ region have $\sim 30\%$ contribution from core rotation. Hence, the extension of the study to the lower mass $A \sim 80, 60$ regions will explore the situation where the lengths of the shears blades (low j orbitals presents in the low mass nuclei) are smaller and the collective rotation may start to dominate. Very recently, multiple chiral doublet bands ($M\chi D$) in ^{78}Br have been reported [123].

It may be worthwhile to carry out nuclear structure studies through lighter beams (like α particles) or through Coulomb excitation but employing a powerful clover array with more than 30 detectors. Such a INGA array is possible by mobilizing the existing resources from the various Indian laboratories. These studies might lead to discovery of new structure phenomena in extreme non-yrast configurations, which will be populated very weakly. The nucleus is an unique system and will continue to fascinate us by exhibiting new structural properties.

Bibliography

- [1] R. M. Clark, A. O. Macchiavelli, *Annu. Rev. Nucl. Part. Sci.* **2000**, 50, 1.
- [2] H. Hübel, *Progress in Particle and Nuclear Physics* **2005**, 54, 1–69.
- [3] Stefan Frauendorf, *Rev. Mod. Phys.* **2001**, 73, 463.
- [4] S. Frauendorf and J. Meng, *Nuclear Physics A* **1997**, 617, 131.
- [5] P.A. Butler, W. Nazarewicz, *Rev. Mod. Phys.* **1996**, 68, 349.
- [6] A. O. Macchiavelli *et al.*, *Physics Letters B* **1999**, 450 1–6.
- [7] M. Sugawara *et al.*, *Phys. Rev.C* **2009**, 79, 064321.
- [8] S. Rajbanshi *et al.*, *Phys. Rev. C* **2014**, 89, 014315.
- [9] A. A. Pasternak *et al.*, *Eur. Phys. J. A* **2008**, 37, 279–286.
- [10] M. J. A. de Voigt, J. Dudek, and Z Szymański, *Rev. Mod. Phys.* **1983**, 55, 949.
- [11] S. Frauendorf, *Nuclear Physics A* **1993**, 557, 259c–276c.
- [12] P. W. Zhao, J. Peng, H. Z. Liang, P. Ring, and J. Meng, *Phys. Rev. Lett.* **2011**, 107, 122501.
- [13] J. Meng, J. Peng, S. Q. Zhang, and P. W. Zhao, *Front. Phys.* **2013**, 8, 55.
- [14] P. W. Zhao, N. Itagaki, and J. Meng, *Phys. Rev. Lett.* **2015**, 115, 022501.
- [15] P. W. Zhao *et al.*, *Phys. Lett. B* **2011**, 699, 181.
- [16] P. W. Zhao *et al.*, *Phys. Rev. C* **2015**, 92, 034319.
- [17] P. W. Zhao *et al.*, *Phys. Rev. C* **2010**, 82, 054319.
- [18] B. N. Lu, E. G. Zhao, and S.-G. Zhou, *Phys. Rev. C* **2012**, 85, 011301R.

- [19] J. Zhao, B. N. Lu, E. G. Zhao, and S.-G. Zhou, Phys. Rev. C **2012**, 86, 057304.
- [20] B. N. Lu, J. Zhao, E. G. Zhao, and S.-G. Zhou, Phys. Rev. C **2014**, 89, 014323.
- [21] A. A. Hecht *et al.*, Phys. Rev. C **2003**, 68, 054310.
- [22] G. Rainovski *et al.*, J. Phys. G: Nucl. Part. Phys. **2003**, 29, 2763.
- [23] H. Pai *et al.*, Phys. Rev. C **2011**, 84, 041301R.
- [24] V. A. Dzuba and V. V. Flambaum *et al.*, Phys. Rev. A **2016**, 93, 052517.
- [25] W. Nazarewicz, J. Dudek, R. Bengtsson, T. Bengtsson, and I. Ragnarsson, Nucl. Phys. A **1985**, 435, 397.
- [26] D.G. Jenkins *et al.*, Physics Letters B **1998**, 428, 23–30.
- [27] D.G. Jenkins *et al.*, Phys. Rev. Lett. **1999**, 83, 500.
- [28] R.M. Clark, *et al.*, Phys. Rev. Lett. **1999**, 82, 3220.
- [29] H. Schnare *et al.*, Phys. Rev. Lett. **1999**, 82, 4408.
- [30] R. Schwengner *et al.*, Phys. Rev. C **2002**, 66024 310.
- [31] Sham S. Malik, Priyanka Agarwal, and Ashok K. Jain, Nuclear Physics A **2004**, 732, 13–23.
- [32] A. A. Pasternak *et al.*, Eur. Phys. J. A **2005**, 23 191–196.
- [33] E.O. Podsvirova *et al.*, Eur. Phys. J. A **2004**, 21, 1–6.
- [34] R.M. Lieder *et al.*, Eur. Phys. J. A **2002**, 13, 297–305.
- [35] P. Datta *et al.*, Phys. Rev. C **2003**, 67, 014325.
- [36] A. V. Afanasjev, S. Mizutori, Z. Phys. A **1995**, 353, 267–271.
- [37] Amita, A. K. Jain, and B. Singh, At. Data Nucl. Data Tables **2000**, 74, 283.
- [38] A. J. Simons *et al.*, Phys. Rev. Lett. **2003**, 91, 162501.
- [39] A. J. Simons *et al.*, Phys. Rev. C **2005**, 72, 024318.
- [40] Santosh Roy *et al.*, Phys. Lett. B **2011**, 694, 322–326.
- [41] Santosh Roy and S. Chattopadhyay, Phys. Rev. C **2011**, 83, 024305.

- [42] S. Rajbanshi *et al.*, Phys. Lett. B **2015**, 74, 387–391.
- [43] S. Rajbanshi *et al.*, Phys. Rev. C **2014**, 90, 024318.
- [44] J. R. Jongman *et al.*, Phys. Rev. C **1994**, 50, 3159.
- [45] Raymond K. Sheline and Prakash C. Sood, Progress of Theoretical Physics **1989**, 81, 5.
- [46] A. Bohr and B. R. Mottelson, Nuclear Structure Benjamin, New York, **1975**, Vol. II.
- [47] Peter Ring and Peter Schuck, The Nuclear Many-Body Problem Springer, New York, **1981**.
- [48] R. F. Casten, Nuclear Structure from a Simple Perspective Oxford Studies in Nuclear Physics.
- [49] A. Bohr, B.R. Mottelson, Phys. Rev. **1953**, 90, 717.
- [50] D. R. Inglis, Phys. Rev. **1954**, 96, 1059.
- [51] D. R. Inglis, Phys. Rev. **1955**, 97, 701.
- [52] P. Möller, J. R. Nix, W. D. Myers, and W. J. Swiatecki, At. Data Nucl. Data Tables **1995**, 59, 185.
- [53] A. V. Afanasjev *et al.*, Phys. Rep. **1999**, 322, 1.
- [54] A. V. Afanasjev and I. Ragnarsson, Nucl. Phys. A **1996**, 608, 176.
- [55] C. M. Petrache *et al.*, Phys. Rev. C **2005**, 72, 064318.
- [56] C. M. Petrache *et al.*, Phys. Rev. C **2012**, 86, 044321
- [57] S. W. Ødegard *et al.*, Phys. Rev. Lett. **2001**, 86 5866.
- [58] T. D. Johnson *et al.*, Phys. Rev. C **1990**, 42, 2418.
- [59] G. N. Sylvan *et al.*, Phys. Rev. C **1997**, 56, 772.
- [60] Otto Haxel, J. Hans D. Jensen, and Hans E. Suess, Phys. Rev. **1949**, 75, 1766.
- [61] MG Mayer, Phys. Rev. **1949**, 75, 1969.
- [62] F. S. Stephens, Reviews of Modern Physics, **1975**, 47, 43.

- [63] W. Nazarewicz, M. A. Riley, and J. D. Garrett, Nucl. Phys. A **1990**, 512, 61.
- [64] V. M. Strutinsky, Yad. Fiz. **1966**, 3, 614 [Sov. J. Nucl. Phys. **1966**, 3, 449]; Ark Fys. **1966**, 36, 629; Nucl. Phys. A **1967**, 95, 420; *ibid.* A **1968**, 122, 1.
- [65] F. Donau, Nuclear Physics A **1987**, 471, 469–488.
- [66] T. Lonnröth *et al.*, Z. Phys. A **1984**, 317, 215.
- [67] P. Petkov *et al.*, Nucl. Phys. A **1998**, 640, 293–321.
- [68] R. Bengtsson and S. Frauendorf, Nuclear Physics A **1979**, 327, 139–171.
- [69] D.M. Cullen, *et al.*, Phys. Rev. C **2002**, 66, 034308.
- [70] E. R. Marshalek, Nucl. Phys. A **1979**, 331, 429.
- [71] Stefan Frauendorf, Z. Phys. A **1997**, 358, 163–167.
- [72] G. Baldsiefen *et al.*, Nucl. Phys. A **1994**, 574, 521–558.
- [73] W. Korten *et al.*, Physica Scripta **1995**, T56, 44–46.
- [74] C. J. Chiara *et al.*, Phys. Rev. C **2000**, 61, 034318.
- [75] S. Zhu *et al.*, Phys. Rev. C **2001**, 64, 041302.
- [76] K. Starosta *et al.*, Nuclear Physics A **2001**, 682, 375c–386c.
- [77] P.A. Butler and W. Nazarewicz, Nuclear Physics A **1991**, 533, 249–268.
- [78] W. Nazarewicz and P. Olanders, Nuclear Physics A **1985**, 441, 420–444.
- [79] B. Ackermann *et al.*, Nucl. Phys. A **1993**, 559, 61–82.
- [80] J. H. Hamilton *et al.*, Act. Phys. Pol. B **2001**, 32, 957.
- [81] G.F. Knoll, *Radiation detection and measurements*, John Wiley and Sons, Inc., New York 2000.
- [82] D. C. Radford, Nucl. Instrum. Methods, Phys. Res., Sect A **1995**, 361, 297.
- [83] D. C. Radford, Nucl. Instrum. Methods, Phys. Res., Sect A **1995**, 361, 306.
- [84] R. K. Bhowmik, INGASORT manual private communication.
- [85] T. Yamazaki, Nucl. Data, Sect. A **1967**, 3, 1.

- [86] E. Der Mateosian and A. W. Sunyar, Atomic data and Nuclear Data tables **1974**, 13, 407–462.
- [87] D. M. Van Patter, E. J. Hoffman, T. Becker and P. A. Assimakopoulos Nuclear Physics A **1972**, 178 355–364.
- [88] K. S. Krane, R. M. Steepen and R. M. Wheeler, Nuclear Data Tables, **1973**, 11, 351–406.
- [89] E. S. Macias, W. D. Ruhter, D.C. Camp and R.G. Lanier, Computer Physics Communications **1976**, 11, 75–93.
- [90] M. Piiparinen *et al.*, Nucl. Phys. A **1996**, 605, 191–268.
- [91] J. H. Lee *et al.*, J. of the Korean Phys. Society, **2002**, 40, 5, 793–801.
- [92] J. S. Kim *et al.*, Phys. Rev. C **1975**, 12, 499.
- [93] P. J. Nolan and J. F. Sharpey-Schafer, Rep. Prog. Phys., Vol. **1979**, 42 1.
- [94] W. M. Currie, Nuclear Instruments and Methods **1969**, 73, 173–185.
- [95] L. C. Northcliffe and R.F. Schilling, Nuclear Data Tables A **1970**, 7, 233.
- [96] N.R. Johnson *et al.*, Phys. Rev. C **1997**, 55, 652.
- [97] J.C. Wells, N.R. Johnson, LINESHAPE: A Computer Program for Doppler Broadened Lineshape Analysis, Report No. ORNL–6689, **1991**, 44.
- [98] F. James and M. Roos, Computer Physics Communications **1975**, 10, 343–367.
- [99] M. A. Cardona *et al.*, Z. Phys. A **1991**, 340, 345.
- [100] M. Lach *et al.*, Z. Phys. A **1993**, 345, 427.
- [101] A. Krämer-Flecken *et al.*, Nucl. Phys. A **1993**, 563, 301.
- [102] M. K. Kabadiyski *et al.*, Nucl. Phys. A **1996**, 605, 191.
- [103] L. W. Fagg and S. S. Hanna, Rev. Mod. Phys. **1959**, 31, 711.
- [104] T. Kibédi, T.W. Burrows, M.B. Trzhaskovskaya, P.M. Davidson, C.W. Nestor, Jr., Nucl. Instr. and Meth. A **2008**, 589, 202–229.
- [105] S. Kumar *et al.*, Phys. Rev.C **2007**, 76, 014306.
- [106] S. Bhowal *et al.*, Phys. Rev.C **2011**, 84, 024313.

- [107] M. Sugawara *et al.*, Eur. Phys. J. A **1998**, 1, 123.
- [108] E. S. Paul *et al.*, Phys. Rev. C **1987**, 36, 153.
- [109] E. S. Paul *et al.*, Phys. Rev. C **1989**, 39, 153.
- [110] A. A. Pasternak, E. O. Lieder, and R. M. Lieder, Acta Phys. Pol. B **2009**, 40, 647.
- [111] S.Y. Wang *et al.*, Phys. Lett. B **2011**, 703, 40.
- [112] D. Tonev *et al.*, Phys. Rev. Lett. **2014**, 112, 052501.
- [113] E. Grodner *et al.*, Phys. Lett. B **2011**, 703, 46.
- [114] E. Grodner *et al.*, Phys. Rev. Lett. **2006**, 97, 172501.
- [115] D. Tonev *et al.*, Phys. Rev. Lett. **2006**, 96, 052501.
- [116] S. Mukhopadhyay *et al.*, Phys. Rev. Lett. **2007**, 99, 172501.
- [117] P.L. Masiteng *et al.*, Phys. Lett. B **2013**, 719, 83.
- [118] E. A. Lawrie *et al.*, Phys. Rev. C **2008**, 78, 021305R.
- [119] Priyanka Agarwal *et al.*, Phys. Rev. C **2007**, 76, 024321.
- [120] Stefan Frauendorf and Jie Meng, Z. Phys. A **1996**, 356, 263-279.
- [121] K. Selvakumar *et al.*, Phys. Rev. C **2015**, 92, 064307.
- [122] J. Meng, J. Peng, S. Q. Zhang, and S.-G. Zhou, Phys. Rev. C **2006**, 73, 037303.
- [123] C. Liu *et al.*, Phys. Rev. Lett. **2016**, 116, 112501.
- [124] A. M. Bizzeti-Sona *et al.*, Z. Phys. A - Atomic Nuclei **1990**, 337, 235–236.
- [125] S. Rajbanshi *et al.*, Phys. Rev. C **2018**, 98, 061304R.
- [126] P. Mason *et al.*, Phys. Rev. C **2005**, 72, 064315.
- [127] Z. Liu *et al.*, Eur. Phys. J. A **1998**, 1, 125.
- [128] W. Urban *et al.*, Phys. Lett. B **1991**, 258, 293.
- [129] W. Nazarewicz and S. L. Tabor, Phys. Rev. C **1992**, 45, 2226.
- [130] R M Clark, J. Phys. G: Nucl. Part. Phys. **1999**, 25, 695.

- [131] T. Koike *et al.*, Phys. Rev. C **2003**, 67, 44319.
- [132] C.W. Beausang *et al.*, Nucl. Phys. A **2001**, 682, 394c.
- [133] S.R. Abhilash, *et al.*, J. Radioanal. Nucl. Chem. **2015**, 305, 749.
- [134] P.J. Nolan, J.F. Sharpey-Schafer, Rep. Prog. Phys. **1979**, 42, 1.
- [135] T.K. Alexander, J.S. Forster, Lifetime Measurements of Excited Nuclear Levels by Doppler-Shift Methods, Springer US, Boston, MA, **1978**, p. 197.
- [136] K.R. Devi, *et al.*, Nucl. Instrum. Methods Phys. Res. A **2018**, 893, 35.
- [137] S. Chakraborty, *et al.*, Phys. Scripta **2018**, 93, 115302.
- [138] F.J. Karasek, Nucl. Instrum. Methods **1972**, 102, 457.
- [139] P. Sharma, *et al.*, Proc. DAE-BRNS Symp. on Nucl. Phys. **2014**, 59, 912–913.
- [140] P. K. Giri, *et al.*, Proc. DAE-BRNS Symp. on Nucl. Phys. **2015**, 60, 984–985.
- [141] M. N. Tantawy *et al.*, Phys. Rev. C **2006**, 73, 024316.

Thesis Highlight

Name of the Student: Sajad Ali

Name of the CI/OCC: Saha Institute of Nuclear Physics **Enrolment No.:** PHYS05201504010

Thesis Title: Structural evolution of weakly deformed nuclei in mass ~ 140 region with increasing angular momentum

Discipline: Physical Science **Sub-Area of Discipline:** Nuclear structure study by gamma spectroscopy

Date of viva voce: 21.08.2020

The main objective of the present thesis work is to investigate the various mechanisms of the generation of angular momentum, which result in the evolution of nuclear structure in the weakly deformed nuclei of mass $A \sim 140$ region. In this thesis work, the high-spin level structure of ^{141}Sm ($Z = 62$, $N = 79$), ^{142}Eu ($Z = 63$, $N = 79$) and ^{140}Eu ($Z = 63$, $N = 77$) have been experimentally investigated using the gamma-ray spectroscopic technique.

The availability of particles and holes in the high- j $h_{11/2}$ orbital in mass ~ 140 region leads to the different exotic excitation. The high angular momentum states can be coupled to form magnetic (MR) and anti-magnetic rotational bands (AMR). The opposite shape driving effects of the $h_{11/2}$ orbital may lead to triaxially deformed nuclei. It may also be possible to observe transitions from magnetic (planar tilt) to Chiral doublet band (aplanar tilt) with increase of excitation energy. In addition, the occupancy of the $d_{5/2}$ and the $h_{11/2}$ orbitals by the protons may lead to the observation of octupole correlation in this mass region.

The high spin states of ^{141}Sm were populated by the reaction $^{116}\text{Cd}(^{31}\text{P}, p5n)$ with $E_{\text{Lab}} = 148$ MeV, at TIFR, Mumbai. The deexciting gamma rays were detected by the Indian National Gamma Array (INGA). This study has established three dipole sequence (I, II, III), where the observed magnetic dipole transition rates ($B(M1)$) have been found to decrease with increasing spin. The Shears Mechanism with Principal Axis (SPAC) calculations reproduced the $B(M1)$ values. The routhian plot showed a rapid increase in frequency with angular momentum which has been also observed in ^{139}Sm . This has been interpreted as the onset of collectivity along the MR band. The partner bands II and III show excellent similarities in the measured quasiparticle alignment, the quasiparticle routhians, the energy staggering and the kinetic moment of inertia. The existence of the degenerate $\Delta I = 1$ doublet bands II and III suggest that the ^{141}Sm can have triaxial deformed nuclear shape at the higher spins. Thus, it may be concluded that a smooth transition of the nuclear shape, from planar (MR) to aplanar (chiral) may exist in ^{141}Sm .

In the same reaction the excited states of the ^{142}Eu nucleus were also populated. A quadrupole band (QB I) and two opposite parity dipole bands (DB I and DB II) were observed. The $B(E2)$ values of the QB I showed a monotonically decreasing nature with increasing spin. The observed behavior could be well reproduced in the framework of Shears Mechanism with Principal axis Rotation Model (SPRM) calculations. This leads to the novel observation of an AMR band in an odd-odd nuclei.

The corresponding reduced transition probabilities $B(M1)$, $B(E1)$ and $B(E2)$ values for the bands DB I and DB II were estimated from the measured level lifetimes. The $B(M1)$ and $B(E2)$ values for both the bands showed a falling trend. The SPAC model calculations indicated that the DB II originate due to the shears mechanism while the DB I is generated due to the interplay of the shears mechanism and collective rotation. The band DB II was found to decay to DB I by enhanced $E1$ transitions. Such large electric dipole transition strengths are the finger prints of the octupole correlation which is supported by the Multi-Dimensional Co-variant Density Functional Theory (MDC-CDFT) calculation. This is the first experimental evidence of octupole correlation between two shears bands.

The high spin state of ^{140}Eu has been populated at IUAC, New Delhi by the reaction $^{112}\text{Cd}(^{32}\text{S}, p3n)$ at $E_{\text{lab}}=145$ MeV and the level scheme has been extended substantially in the present measurement. From the present data, ten quadrupole bands and two dipole bands have been established.